Raman Research Institute

Astronomy & Astrophysics Group

Ph.D. Dissertation

The Origin And Propagation Of Ultra-High Energy Cosmic Ray Particles

Saikat Das

Research Fellow, A&A – RRI
Supervisor: Nayantara Gupta
Bengaluru 560080, India

July 2020

Thesis Submitted
for the degree of

Doctor of Philosophy

Jawaharlal Nehru University
New Delhi 110067, India

Declaration

I, ***Saikat Das*** (Enrolment No.: RRI/2016/018), declare that the work reported in this thesis titled '***The Origin And Propagation of Ultra-High Energy Cosmic Ray Particles***', is entirely original. This thesis is composed independently by me at ***Raman Research Institute (RRI)*** under the supervision of ***Dr. Nayantara Gupta*** and is the result of my own work unless otherwise stated. I further declare that the subject matter presented in this thesis has not previously formed the basis for the award of any degree, diploma, membership, associateship, fellowship or any other similar title of any university or institution. I also declare, this thesis has been checked through the plagiarism software TURNITIN.

- The material in Chapter 2 has been published in *Physical Review D* (Saikat Das, Soebur Razzaque, and Nayantara Gupta; Phys. Rev. D 99, 083015 (2019))
- The material in Chapter 3 has been published in *The Astrophysical Journal* (Saikat Das, Nayantara Gupta, and Soebur Razzaque; Astrophys. J. 889, 149 (2020))
- The material in Chapter 4 has been published in *The European Physical Journal C* (Saikat Das, Soebur Razzaque, and Nayantara Gupta; Eur. Phys. J. C 81, 59 (2021))

Signature of Supervisor	Signature of Candidate
Dr. Nayantara Gupta	**Saikat Das**
Associate Professor, RRI	Research Fellow, RRI

Astronomy & Astrophysics Group
Raman Research Institute (RRI)
Bengaluru 560080, Karnataka IN

Date:

Place:

Certificate

This is to certify that the work contained in the thesis titled '***The Origin And Propagation of Ultra-High Energy Cosmic Ray Particles***', submitted by ***Saikat Das*** (Enrolment No.: RRI/2016/018) to the Jawaharlal Nehru University for the award of the degree of ***Doctor of Philosophy (Ph.D.)*** in Physical Sciences, is the bonafide record of orginal research work carried out by the candidate from August 2016 — July 2020, under my guidance and supervision at Raman Research Institute (RRI), Bengaluru, India. The results embodied in the thesis have not been submitted to any other University or Institute for the award of any degree or diploma.

Signature of Director	Signature of Supervisor
Prof. S. Sridhar	**Dr. Nayantara Gupta**
Director (i/c) & Professor, RRI	Associate Professor, RRI

Astronomy & Astrophysics Group
Raman Research Institute (RRI)
Bengaluru 560080, Karnataka IN

Date:

Place:

Acknowledgements

I express sincere gratitude to my thesis supervisor Dr. Nayantara Gupta (Associate Professor, Raman Research Institute, Bengaluru, India), for her consistent support and cooperation. Her perspectives and ingenuity towards research have helped me to evolve over time as an individualistic research fellow.

The thesis work was carried out in collaboration with Dr. Soebur Razzaque (Professor, University of Johannesburg, Auckland Park, South Africa), who has always conveyed great enthusiasm and provided assistance in tackling the problems. His critical approach has contributed to improving the quality of work.

A very special thanks to Dr. Nirupam Roy (Assistant Professor, Indian Institute of Science, Bengaluru, India) for his support in computational techniques and discussions on statistical methods. Also, his urge for multicuisine food has served my appetite too.

I have always received a great deal of help in academic and non-academic needs from my friends at RRI and IISc. The vivid discussions and all the activities we did together during the last four years, up until the onset of the COVID-19 pandemic recently, will always be memorable.

I acknowledge the support received from the *Computer Section, RRI* for providing facilities related to computation and networking. I have benefited from the vast volume of the digital repository, online resources, and a massive collection of print version books, maintained by the *Library Section, RRI*.

I am indebted to the *Secretary, A&A,* (Mrs. Harini) and the *Administration Block, RRI* for timely processing of official documents and other essential tasks. I am obliged for the fellowship grant, travel allowance, accommodation facility, etc., provided by RRI.

Saikat Das

20 July 2020

Contents

Synopsis

Introduction

Cosmic-ray physics has evolved over the last hundred years as a multi-disciplinary subject entailing high-energy particle physics, relativistic astrophysics, and plasma physics. Cosmic rays are comprised of a wide variety of charged particles, ranging from leptons to hadrons (baryons and mesons), including atoms and nuclei that hit the Earth's atmosphere after propagating through Galactic or extragalactic distances. The spectrum of these particles spans from a few MeV ($\equiv 10^6$ eV) to $\sim$ 1 ZeV ($\equiv 10^{21}$ eV) energy range with a varying flux and mass composition. Of particular interest are the particles with energies $E \geqslant 1$ EeV ($\equiv 10^{18}$ eV) and extending up to a few times 100 EeV. These are the highest energy particles observed in the Universe, called the *ultrahigh-energy cosmic-ray* (UHECR) particles. The astrophysical conditions that accelerate particles to such high energies have been probed since their first detection was made at *Volcano Ranch Experiment*, New Mexico, in 1962. The sources are believed to be extragalactic owing to the inability of Galactic sources to accelerate particles up to such high energies. The *Pierre Auger Observatory* (PAO) in Argentina and the *Telescope Array* (TA) in the United States are state-of-the-art experiments measuring UHECR spectrum, composition, and arrival directions by reconstructing the giant hadronic cascades they induce in the Earth's atmosphere.

Various steady and transient astrophysical objects like *gamma-ray bursts* (GRBs), *active galactic nuclei* (AGNs), *starburst galaxies* (SGs), etc., are considered to be potential candidates for UHECR acceleration. Nevertheless, the correlation of a UHECR event with any specific source is yet to be made. The *Galactic magnetic field* (GMF), as well as the *extragalactic magnetic field* (EGMF), deflects the UHECRs during their propagation. As a result, it creates a shadowing effect on the true location of sources and also limits the maximum distance from which particles can reach the detector. Thus, the origin of UHECRs has remained an intriguing mystery of astroparticle physics. In this thesis, we do a semi-analytical study of UHECR propagation, employing a *Monte Carlo* simulation framework, to predict the flux of secondary neutrinos and photons expected at Earth. We explore multi-messenger astrophysical phenomena to identify UHECR sources through high-energy electromagnetic counterparts. Our study also tests various mass composition models to constrain the source population requirements and sheds light on the accelerator environment. By and large, our knowledge of photohadronic interactions dominating at different energies is reinforced, thus explaining various spectral features, viz., the origin of ankle and cutoff in the cosmic-ray spectrum.

UHECR Composition & Cosmogenic Neutrinos

UHECRs propagate over cosmological distances, rendering them susceptible to pho-

tohadronic interactions with the *cosmic microwave background* (CMB) and the *extragalactic background light* (EBL). The produced neutral and charged pions decay to yield cosmogenic photons and neutrinos, which are ideal messengers of UHECR acceleration. But the neutrino spectrum depends heavily on the source properties and composition at injection. We scan the UHECR parameter space to constrain the abundance fraction of light nuclei composition (H+He), by fitting the observed energy spectrum from 10^{18} eV up to the highest energies. We consider a general source population having a power-law evolution in redshift and include all relevant energy loss processes of UHECRs to simulate the propagation. For our most optimistic scenario, upcoming detectors will either detect cosmogenic neutrinos within a few years of observation or restrict the parameter ranges. The cosmogenic photon fluxes for representative cases are also found to be consistent with the currently known upper bound. For an initial flavor ratio of $\nu_e : \nu_\mu : \nu_\tau = 1 : 2 : 0$ at production, the expected flux of individual flavors at Earth is in the ratio $1 : 1 : 1$, by virtue of neutrino oscillations. However, the contribution of neutron beta decay to cosmogenic neutrinos can shift the ratio of the fluxes of individual flavors from their constant values. Thus, the measurement of fluxes of individual flavors can act as a discriminator between different mass composition models. We have also analyzed the spectrum with a mixed composition (H+He+N+Si) at injection, fitting the region above the ankle ($E \gtrsim 10^{18.7}$ eV). But, the resulting neutrino flux in the latter case is far below the sensitivity of proposed detectors, unlikely to be detected in the near future. Also, the best-fit corresponds to a negative source evolution index, and the injection spectral index is found to be too hard compared to typical Fermi acceleration values. Future detection of cosmogenic neutrinos will be a robust test of these plausible scenarios.

VHE Gamma-Rays from UHECR Interactions

AGNs are a class of compact astrophysical objects found at the center of "active galaxies" that can radiate across the entire electromagnetic spectrum. The emission from these black holes is powered by accretion, causing a collimated beam of outflow, whereby particles are accelerated to relativistic energies. This makes them ideal UHECR accelerator candidates. Blazars, a class of radio-loud AGN, have their jets oriented along the observer's line-of-sight direction. *BL Lacertae* (BL Lac) objects are those blazars that have no characteristic spectral lines and exhibit a non-thermal continuum emission from radio to gamma-ray wavelengths with two prominent peaks. In some of them, called *high-frequency peaked BL Lac objects* (HBLs), the low-energy peak owing to synchrotron emission can extend up to X-ray energies. The high-energy peak in the case of HBLs, particularly the *very high-energy* (VHE; $E \gtrsim 30$ GeV) spectrum, is difficult to be explained solely using *inverse-Compton* (IC) scattering of synchrotron photons inside the jet. We invoke a lepto-hadronic process in play to fit the multiwavelength spectrum, up to the highest energies. For the values of jet parameters obtained, consistent with the modeling of leptonic emission, we find the acceleration of UHECR protons is plausible in HBLs up

to $\approx 10^{19}$ eV. These protons are expected to traverse cosmological distances interacting relatively close to Earth, producing e^+e^- pairs and $\pi^0 \rightarrow \gamma\gamma$ photons. A substantial fraction of the observed gamma-ray signal is found to originate from the electromagnetic cascade of these $e^{\pm}$ and γ-rays. The kinetic power of the jet complies with the Eddington luminosity of the corresponding supermassive black hole. We have considered a random turbulent EGMF with a Kolmogorov power spectrum to account for the UHECR survival rate along the observer's line-of-sight direction. However, the prospects of detecting neutrino or UHECR events are currently unfavorable. Multi-messenger observation of blazars can genuinely put this proposition on firmer grounds.

Two-Population Model of UHECR Sources

The *extensive air shower* (EAS) induced by a UHECR event on incidence at Earth's atmosphere is recorded using the *surface detector* (SD), as well as, the *fluorescence detector* (FD). Even with the hybrid detection technique and high statistics observed by PAO, the mass composition of UHECRs is not well constrained due to the lack of precise measurement of interaction cross-sections at the highest energies. The uncertainties in various hadronic interaction models at ultrahigh energies lead to inconsistencies in the modeling of maximum shower depth distribution $X_{\rm max}$. However, all of the current LHC-tuned models predict a decrease in proton fraction for $E > 10^{18.3}$ eV, with heavier nuclei such as Nitrogen dominating at the highest-energy bin. A combined fit of energy spectrum and mass composition data to that generated from a single extragalactic source population yields zero ^{1}H abundance fraction, for a mixed composition at injection. The slope of the $\langle X_{\rm max}\rangle$ fit for $E > 10^{18.7}$ eV suggests a significant scope of improvement. For a well-suited hadronic model (SYBILL2.3C), we add the contribution from a second extragalactic source population injecting ^{1}H only, such that the resultant spectrum extends up to the highest-energy bin. High-luminosity GRBs are such sources, where the relativistic outflows are mainly proton dominated. Another population injects light-to-heavy nuclei with distinct values of maximum rigidity and injection spectral index. A one-to-one comparison shows a notable improvement in the combined fit, with a statistical significance much higher than 3σ, while going from the one-population to two-population model. We present the maximum allowed proton fraction in the highest-energy bin at $> 3\sigma$ confidence level. The maximum rigidity of the proton population, being closer to GZK cutoff energy, results in a large number of secondary neutrinos dominating the cumulative neutrino spectrum in the two-population model. Detection of these neutrinos by future experiments will be a confirmation of the existence of protons at the highest energy.

Summary & Outlook

Although a dramatic change has been in progress towards our understanding of UHECRs, we are yet to witness the identification of the first astrophysical UHECR source. The anisotropy in UHECR arrival directions above 8 EeV observed by PAO, at 5.2σ statistical

significance, cannot be possible due to deflections of an initially isotropic flux. In a recent analysis, PAO has studied the correlation of observed intermediate-scale anisotropy in UHECR arrival directions with extragalactic gamma-ray source catalogs. The results indicate that starburst galaxies better explain the data, at 4σ statistical significance, compared to isotropy. Thus, an excess emission from strong nearby sources seems to be feasible with current statistics. However, the number of such events recorded with terrestrial detectors is inadequate. In the future, improved sensitivity and higher exposure will provide better constraints on the source models, narrowing down the viable parameter ranges.

While new data-based methods are already being implemented by PAO to improve energy calibration, the proposed AugerPrime upgrade will enhance the quality of mass composition reconstruction. Coincident observations of neutrinos and gamma-rays along with UHECR events, will also be crucial to precisely locate the highest-energy cosmic accelerators. At the highest energies, a time correlation of UHECRs with electromagnetic counterparts is expected to be maintained. This can provide directional information and also the proof of dominant interactions at various energies. For heavier nuclei to dominate at the highest energy bin ($10^{20.1}$ – $10^{20.2}$ eV), these UHECRs must originate at distances $z \lesssim 0.5$. In such a scenario, the cutoff occurs due to the maximum acceleration energy at the sources. However, several alternatives also do exist. We have tried to focus on such phenomenological aspects and multi-messenger observations in the thesis.

Like every analysis, our one has its own shortcomings. We have taken care to mention the approximations concerning numerical and computational methods, wherever applicable. We illustrate our results as coherently as possible to the best of our knowledge.

Signature of Supervisor
Dr. Nayantara Gupta
Associate Professor, RRI

Signature of Candidate
Saikat Das
Research Fellow, RRI

Astronomy & Astrophysics Group
Raman Research Institute (RRI)
Bengaluru 560080, Karnataka IN

List of Publications

1. **Saikat Das**, Soebur Razzaque, and Nayantara Gupta
   Ultrahigh energy cosmic rays and neutrinos from light nuclei composition
   Physical Review D **99**, 083015 (2019)
   arXiv.org identifier: arXiv:1809.05321 [astro-ph.HE]

2. **Saikat Das**, Nayantara Gupta, and Soebur Razzaque
   Ultrahigh-energy Cosmic-Ray Interactions as the Origin of Very High-energy γ-Rays from BL Lacertae Objects
   The Astrophysical Journal **889**, 149 (2020)
   arXiv.org identifier: arXiv:1911.06011 [astro-ph.HE]

3. **Saikat Das**, Soebur Razzaque, and Nayantara Gupta
   Modeling the spectrum and composition of ultrahigh-energy cosmic rays with two populations of extragalactic sources
   The European Physical Journal C **81**, 59 (2021)
   arXiv.org identifier: arXiv:2004.07621 [astro-ph.HE]

4. **Saikat Das**, Nayantara Gupta, and Soebur Razzaque
   PeV-EeV neutrinos from gamma-ray blazars due to ultrahigh-energy cosmic-ray propagation
   The Astrophysical Journal (ACCEPTED FOR PUBLICATION)
   arXiv.org identifier: arXiv:2012.13877 [astro-ph.HE]

List of Figures

List of Tables

1

Introduction

Continuous efforts unrolling for more than a century have made it possible to perceive the astrophysical information carried to Earth by messengers other than photons. The data collected in various wavebands have been appended to the optical database starting from the 1930s, with the first astronomical discovery of a radio source. Within a few decades, supernova remnants (SNRs) and active galactic nuclei (AGNs) were identified in the radio sky. Sooner in the 1960s, the advancement of X-ray observation due to space-based experiments (sounding rocket flights) added more clarity and opened a new window to the non-thermal universe. The EGRET instrument of the Compton Gamma-Ray Observatory (CGRO), launched in 1991, provided the first rigorous map of the gamma-ray sky at energies above $\epsilon_\gamma \gtrsim 100$ MeV. The observation of an overwhelming number of objects across the entire electromagnetic spectrum, through these evolutionary stages, has provoked scientists towards the search for the most extreme and violent cosmic phenomena. Since then, the domain of gamma-ray astronomy has evolved in its own right as a distinct field in astronomy and astrophysics, advancing to the recent measurement of photons from point sources up to energies $\epsilon_\gamma \sim 100$ TeV.

Several sources in our Galaxy have been identified so far, capable of producing high-energy (HE; 30 MeV < ϵ_γ < 30 GeV) and very high-energy (VHE; 30 GeV < ϵ_γ < 30 TeV) gamma rays, viz., pulsars, SNRs and the Galactic center. The interaction of Galactic cosmic rays with matter and radiation fields contribute to the diffuse Galactic emission (DGE). The Large Area Telescope on board NASA's Fermi Gamma-Ray Space Telescope (*Fermi*-LAT), launched in 2008, has been successful in probing the isotropic diffuse gamma-ray background (IGRB) in the range between 100 MeV – 820 GeV energies, originating from extragalactic unresolved or faint sources. The extragalactic gamma-ray background (EGB) includes both individual and diffuse sources from the edge of the Milky Way to the edge of the observable universe. Contribution from the ultra-relativistic jets of AGNs, star-forming galaxies, gamma-ray bursts (GRBs), and beamed emission from blazars dominates the EGB. The *Fermi*-LAT fourth source catalog (4FGL) lists 5064 sources above 4σ significance between 50 MeV – 1 TeV energy range, based on 8-yrs of data.

However, at $\epsilon_\gamma \gtrsim 1$ PeV energies, the universe is impenetrable to electromagnetic radiation. The universal photon background, viz., the cosmic microwave background (CMB) and the extragalactic background light (EBL) scatters the high-energy photons producing secondary electrons and positrons. The EBL covers all wavelengths apart from the microwave band and peaks at optical – infrared – ultraviolet energy range [1–4]. The

condition that gives the threshold energy of interaction is

$$\gamma + \gamma_{\rm bg} \rightarrow {\rm e}^+ + {\rm e}^- \qquad\qquad \epsilon_\gamma \epsilon_{\rm bg} \geqslant \frac{2m_e^2 c^4}{1-\cos\psi} \tag{1.1}$$

where ϵ_γ and $\epsilon_{\rm bg}$ are the energies of the high-energy photon and the background photon, respectively. The scattering angle is denoted by ψ, and m_e is the electron mass. Hence, for sources situated at a distance more than the pair-production length of γ-rays produced in it, high-energy photons are not efficient messengers of intrinsic physical processes.

Leptons can produce γ-rays in a magnetic field through various processes, such as synchrotron emission, synchrotron self-Compton (SSC) processes, and inverse-Compton (IC) scattering of external photons inside highly luminous astrophysical objects [5–7]. Fortunately, more often than not, VHE γ-rays are suspected to be produced in association with cosmic rays (CR). The latter are charged particles accelerated inside astrophysical sources, primarily comprised of protons and other nuclei. The CR spectrum spans over several decades of energy from a few MeV to $\sim$ 1 ZeV energy range. Cosmic rays, with energies higher than the required threshold, can undergo interactions with ambient matter and light to produce γ-rays. Observation of γ-rays produced through this hadronic channel distinctly, can provide direct proof of CR acceleration in relativistic outflows, such as magnetized plasma winds or jets of AGN. The observed CR spectrum is denoted by $dN/dE \sim E^{-\beta}$, where β is the spectral index. The flux and the observed composition varies widely with sharp changes in β at specific energies, indicating an alteration in acceleration mechanism or transition between source populations.

The most energetic cosmic rays extend up to the sub-ZeV energy regime. These are called the ultrahigh-energy cosmic rays (UHECRs; $E \gtrsim 0.1$ EeV), the highest-energy particles observed in the universe. Now, for particles to be accelerated up to ultrahigh energies, the confinement radius must be larger than the Larmor radius (r_L) of the charged particle. r_L of a charged particle in a magnetic field can be written as

$$r_L = \frac{E}{ZeB} \sim 110 \text{ kpc } Z^{-1}\left(\frac{\mu G}{B}\right)\left(\frac{E}{100 \text{ EeV}}\right) \tag{1.2}$$

The value of r_L in Galactic magnetic fields ($\sim$ μG) is much higher than the Galactic disk's thickness, leading to the search for extragalactic sources. A simple criterion can be deduced by placing sources in the $B - R$ phase-space, called the "*Hillas diagram*" and grouping them according to the maximum acceleration energy $E_{\rm max}$ [8]. The timescales of acceleration and diffusion are also essential and must be taken into account. The high-energy emission from accreting black holes produces UHECRs by virtue of diffusive shock acceleration of particles inside the jets, known as the Fermi acceleration mechanism [9]. The particles gain energy through repeated reflection from magnetic mirrors. Another prevalent method is the formation of unipolar inductors in rapidly rotating neutron stars or other relativistic magnetic rotators. For example, neutron stars (NS) can accelerate particles in the relativistic outflows because of the strong magnetic field [10].

Numerous extragalactic candidate source classes have been proposed, capable of accelerating UHECRs. A vast majority of these are transient sources related to the birth of compact objects or explosions resulting from their gravitational interactions [11, 12], eg., tidal disruption events (TDE) of neutron stars or white dwarfs [13–16], gamma-ray bursts (GRBs) [17–21], hypernovae [22], binary black hole merger events [23, 24], etc. γ-rays can be produced by the interaction of cosmic rays near the source or during the propagation in extragalactic space. Sources such as starburst galaxies, powerful extended jets/lobes of FR-I and FR-II radio galaxies [25, 26], AGNs powered by the accretion onto a supermassive black hole (SMBH), TeV blazars [27–29], etc., are also potential UHECR accelerators. A comparison of photon arrival times is critical to understand whether strong γ-ray emitters are also UHECR emitters.

The Pierre Auger Observatory (PAO) in Malargüe, Argentina, and the Telescope Array (TA) experiment in the United States have been observing UHECRs for more than a decade now. However, a correlation of known astrophysical sources with a UHECR event is yet to be made. The observed large-scale anisotropy (averaged in angular windows of 45° radius) above 8×10^{18} eV in their arrival directions suggest that UHECRs cannot possibly originate from an initially isotropic flux by deflections in a magnetic field. Nevertheless, the Galactic and extragalactic magnetic field (GMF and EGMF) pose additional challenges in UHECR source identification. Once injected into the cosmos from their sources, UHECRs undergo several photohadronic interactions with the all-pervasive universal photon backgrounds. CMB is the most abundant of these, with a number density $n_\gamma \sim 410$ cm^{-3} having energy $\epsilon_{\rm bg}^{\rm CMB} \sim 0.1$ meV. The observed spectrum above 10^{18} eV exhibits several interesting features, a reminiscence of the UHECR interactions and energy loss processes.

The earliest multi-messenger observation dates back to the 1960s when a team led by Raymond Davis detected electron neutrinos produced from nuclear reactions inside the Sun [30, 31]. The observation of neutrinos before electromagnetic radiation from Supernova-1987A emphasized the usefulness of neutrinos beside photons to probe the emission processes inside astrophysical objects [32, 33]. The complementary information obtained from the detection of neutrinos, gravitational waves, cosmic rays has ever since proved to be particularly commendable in concretizing the field of multi-messenger astronomy. Since γ-rays are produced by the interaction of charged particles viz., leptons and hadrons, the observed diffuse neutrino flux may as well stem from photohadronic interactions of cosmic rays. The IceCube Neutrino Observatory has made significant progress towards the detection of neutrinos of cosmic origin. It is now possible to differentiate between the diffuse astrophysical neutrino flux produced inside the sources and the atmospheric neutrino flux resulting from CR interactions in the Earth's atmosphere. Strong evidence of cosmic neutrino signal was observed by IceCube in 2013, setting the benchmark for self-consistent modeling of CR sources.

The following sections of this chapter connect the multiple facets of UHECR physics. In

Sec. 1.1, we provide a brief overview of the UHECR acceleration processes and the energy-loss interactions during propagation through cosmological distances. In Sec. 1.2, we account for the ongoing experiments and the detection techniques employed in UHECR detection. Sec. 1.3 explains the interdependency of cosmic rays, γ-rays, and neutrinos to study the high-energy astrophysical universe. The current state of research on spectrum, composition, and anisotropy of UHECRs is briefed in Sec. 1.4. The motivation of the research in this thesis is driven by current unknowns and stimulated by the rapid evolution of the subject, illustrated in Sec. 1.5.

1.1 Acceleration & Propagation

At the beginning of the twentieth century, the current flowing in ionization chambers without any artificial sources of ionization was termed as "dark current". Some explanations ascertained the radiation emitted from the decay of radioactive impurities near the Earth's surface as the cause. But the ionization current only dropped at low altitudes and went on rising as the ionization chamber was taken vertically upwards in a balloon flight, away from the Earth's surface. Victor Hess inferred a cosmic origin of the dark current in his famous balloon flight experiment in 1912 [34]. First considered to be a highly penetrating form of γ-rays, it was later understood that these are charged particles due to their deflections in Earth's magnetic field. The observed flux was found to depend on the geomagnetic latitude of Earth. In 1938, French physicist Pierre Victor Auger was able to detect the secondary particles with ground detectors [35], resulting from the interaction of primary CR of PeV energies (1 PeV $\equiv 10^{15}$ eV) with the Earth's atmosphere.

From the 1930s to the mid-1950s, the study of elementary particles was one of the main aims of CR physics. Several particles, such as e^+, $\mu^\pm$, $\pi^\pm$, K-mesons, and some hyperons, were discovered in cosmic rays. With the advent of powerful particle accelerators, such studies in the energy range of up to $\sim$ 1 TeV have become more organized. The center of interest in CR physics has now shifted in unveiling its astrophysical aspects. The highest-energy particle detected to date extends up to sub-ZeV (1 ZeV $\equiv 10^{21}$ eV) energy regime and is thus an intriguing problem of astroparticle physics [36–38]. One can hardly overestimate the importance of high-energy cosmic rays in understanding the production and interaction of particles at these extreme energies. UHECRs are the highest energy particles observed in the universe with energy $E \gtrsim 0.1$ EeV. UHECR air shower created by a primary particle of energy 10^{20} eV was first detected in the Volcano Ranch experiment (New Mexico) in 1962, by a team led by John Linsley and Livio Scarsi [39].

1.1.1 Acceleration of UHECRs

Although, the sources of UHECRs are still unidentified [36, 37, 40], the power-law nature of the observed spectrum indicates a non-thermal physical process as their origin. The Hillas plot in Fig. 1.1 shows the astrophysical objects in $B - R$ phase space diagram [8]. The dotted red lines indicate the BR product beyond which the confinement of

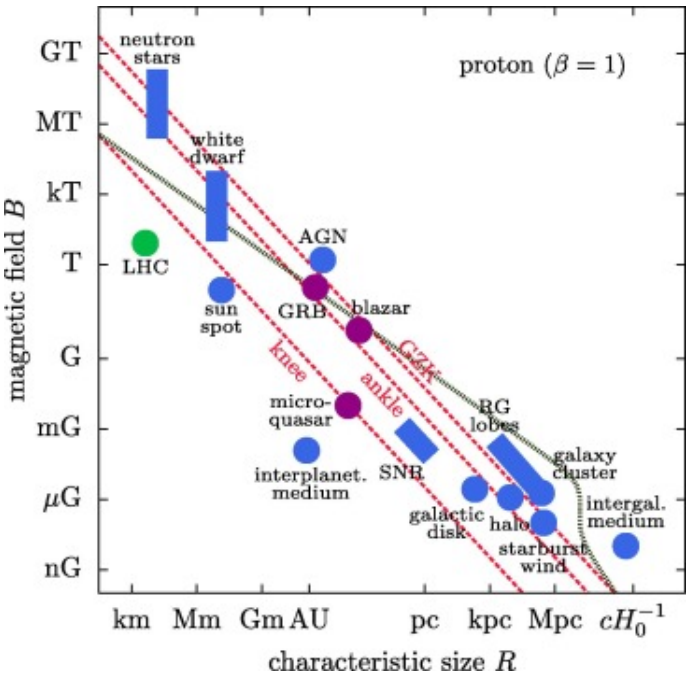

Figure 1.1: The diagram shows the astrophysical sources in $B - R$ phase space. The red dotted lines indicate the BR product beyond which confinement of protons at the knee, ankle, and cutoff of the CR spectrum is possible. The grey dotted lines are the second upper limit taking into account the synchrotron losses of UHECRs inside the sources and interaction with cosmic background photons. The image is taken from Ref. [42].

protons with energy 1 PeV, 5 EeV, 60 EeV are possible for outflows with velocity $\beta = 1$. Larmor radius (cf. Eqn. 1.2) of the particle must be smaller than the size of the accelerator ($r_L(E) < R$), thus constraining the magnetic field of the acceleration region. Enrico Fermi, in 1949 proposed the acceleration mechanism of high-energy cosmic rays through the stochastic collisions in irregularities of the EGMF [9]. The intergalactic medium contains ionized gas, which is highly conductive and contains no net electric field. The average energy gain is given by $\langle \Delta E/E \rangle \sim 4\beta^2/3$, where β is the non-relativistic velocity of the magnetic irregularity. The number of particles with energies between E and $E+dE$ is given by $N(E)dE$. The spectrum of accelerated particles is found to be a power-law $dN/dE \sim E^{-\alpha}$. This is known as the "*second-order Fermi acceleration process*" [41].

However, the random velocity of magnetic clouds in the Galaxy is $\beta \lesssim 10^{-4}$, and the mean free path of CR scattering is ~ 1 pc. The number of collisions per year is few, resulting in a very slow energy gain of the particles to reach the UHE regime. Monoenergetic particles will encounter random collisions, and thus the energy distribution will become broadened. The more general Fokker-Planck equation treats the statistical nature of the problem and energy spectrum broadening, for the diffusion of particles in momentum space [43]. The first-order Fermi process considers a shock wave where particles can gain energy as they bounce back and forth, leading to $\langle \Delta E/E \rangle \propto \beta$ [44, 45]. Galactic cosmic rays are predicted to be accelerated in SNR shocks by this process.

Relativistic shocks ($\Gamma > 10$) can accelerate particles up to the highest energies depending on the magnetic turbulence [46, 47]. In one cycle of upstream-downstream-upstream motion of the particle through the shock, the energy gain can be as much as $\simeq 4\Gamma^2$. After the first cycle, the distribution becomes highly anisotropic within an angle of $1/\Gamma$ due to relativistic beaming. As a result, the energy gain in subsequent cycles is greatly reduced to $\Delta E/E \simeq 2$. For GRBs, $\Gamma \sim 300$ and the upstream magnetic field is $10-100\ \mu$G, as derived from X-ray afterglow emissions [48, 49]. In such a scenario, particles can gain energies up to $\sim 10^{15}$ eV. One-shot acceleration in AGN jets can provide an energy boost by a factor of Γ^2, whereby CRs of energy 10^{17} eV or below can penetrate the jet sideways and get accelerated to ultra-high energies, independent of the magnetic turbulence [50]. The upstream-downstream-upstream motion of the energetic particles can also create plasma instabilities, thus increasing the magnetic turbulence level that accelerates the particles. The amplification of the magnetic field by streaming instabilities was originally proposed for non-relativistic shocks in SNRs [44, 51] and was later extended to obtain more detailed results [52–56]. Diffusive acceleration in collisionless shock waves is still one of the most favorable acceleration mechanism of cosmic rays at all energies [57].

Magnetized and fast-spinning stellar objects can induce electric fields, in which particles can be accelerated up to ultrahigh energies. This method is known as "*unipolar induction*". Black hole magnetospheres and fast-spinning magnetized neutron stars are such relativistic magnetic rotators that lose rotational energy in jets. The neutron stars (NS) have a population density of $\dot{n}_s = 3 \times 10^{-3}$ Mpc^{-3}yr^{-1} and a rotational energy

$$E_{\rm rot} \simeq 2 \times 10^{52} \left(\frac{I}{10^{45}\ {\rm gm\ cm^2}}\right)\left(\frac{\Omega}{10^{-3}\ {\rm s}}\right)^{-2} {\rm erg} \tag{1.3}$$

where I is the moment of inertia, and Ω is the period of rotation [58]. The flux from UHECR sources can be written as

$$J(E) = \frac{c}{4\pi} Q(E) \tau_{\rm loss}(E) \tag{1.4}$$

where $Q(E)$ is the injection rate per unit volume, and $\tau_{\rm loss}$ is the timescale of energy losses. The required source emissivity is found by comparing the above expression with the observed flux at a fixed energy. It turns out to be $\approx 3 \times 10^{45}$ erg Mpc^{-3} yr^{-1} at 10^{19} eV [59]. Hence, NS can meet the energy requirement if they emit a fraction $\sim 10^{-4}$ of their luminosity in UHECRs [10, 60, 61]. An electric field is generated at the NS surface owing to the rotational energy and strong magnetic field. Thus, a potential drop in the outflowing plasma winds is created, whereby particles can be accelerated.

$$\Phi = \frac{2\pi^2 B R_s^3}{\Omega^2 c^2} \simeq 7 \times 10^{19} \left(\frac{B}{10^{13}\ {\rm G}}\right)\left(\frac{R_s}{10^6\ {\rm cm}}\right)^3 \left(\frac{\Omega}{10^{-3}\ {\rm s}}\right)^{-2} {\rm V} \tag{1.5}$$

This corresponds to a maximum particle Lorentz factor $\gamma_\Phi = Ze\Phi/(Am_p c^2)$, which is equivalent to an energy of 10^{20} eV for ^{56}Fe nuclei. It has been shown that young neutron stars with millisecond rotation periods and very high-surface magnetic fields $B_\star$ (called "*magnetars*") can accelerate particles upto ultrahigh energies [10].

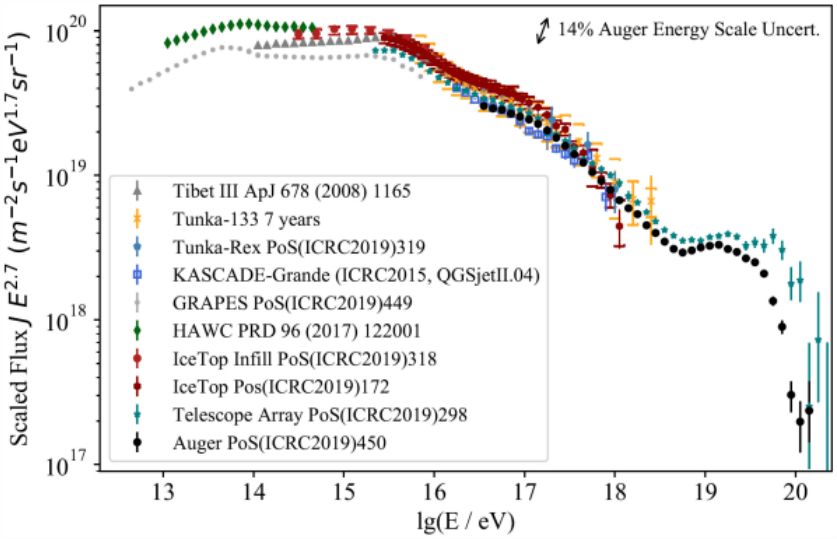

Figure 1.2: The high-energy CR spectrum from ~TeV energies up to 100 EeV combining the measurement from various experiments, that use various detection techniques. The image is taken from Ref. [68].

1.1.2 Extragalactic propagation

The observed CR spectrum from 10 TeV to over 100 EeV is shown in Fig. 1.2, with data taken from recent measurements by KASCADE-Grande [62], IceTop array [63], HAWC [64], Telescope Array [65], Pierre Auger Observatory [66], and other experiments. The spectrum can be explained using a broken power-law with the spectral indices changing sharply at various points. The sudden steepening of the spectrum near $\approx$ 1 PeV is called the "*knee*", which may have an astrophysical origin. The hardening of the spectrum near to $\approx$ 5 EeV is known as the "*ankle*". The steep decline in the observed flux beyond $\approx$ 60 EeV is called the "*cutoff*" in the CR spectrum. There exists a debate on the transition energy from Galactic to extragalactic cosmic rays, which occurs somewhere between the knee and ankle [67]. But, little uncertainty exists in attributing the spectral features seen beyond the ankle to the extragalactic propagation of UHECRs.

The interaction of UHECRs with CMB and EBL results in pair production, photo-pion production, and in case of heavier nuclei, photo-disintegration. The rate of interactions encountered by UHECRs during its passage is given by

$$\frac{1}{\tau} = \frac{c}{2\Gamma^2} \int_{\epsilon'_{\rm th}}^{\infty} \epsilon' \sigma(\epsilon') \int_{\epsilon'/2\Gamma}^{\infty} \frac{n_\gamma(\epsilon)}{\epsilon^2}\, d\epsilon\, d\epsilon' \tag{1.6}$$

where $\sigma(\epsilon')$ is the interaction cross-section, and ϵ' is the background photon energy in the particle rest frame. $\epsilon'_{\rm th}$ is the threshold of interaction and $n_\gamma(\epsilon)$ is the number of background photons per unit volume and energy interval, in the laboratory frame. The center of momentum frame energy squared, $s = m_p^2 c^4 + \epsilon E(1 - \beta \cos\theta)$ yields the value of $\epsilon_{\rm th}$ required for various interactions. The photopion production of ultrahigh-energy

protons occur through the Δ-resonance channel

$$p + \gamma_{bg} \rightarrow \Delta^{+} \rightarrow \begin{cases} p + \pi^0 \rightarrow p + \gamma\gamma \\ n + \pi^{+} \rightarrow n + \mu^{+} + \nu_{\mu} \rightarrow n + e^{+} + \nu_e + \overline{\nu}_{\mu} + \nu_{\mu} \end{cases} \tag{1.7}$$

The inelasticity η is $0.2 - 0.5$, and $E_{\rm CMB} \sim 1$ meV. The threshold of interaction is

$$E_{\rm th}^{N,\pi} = \frac{m_{\pi}c^4(m_N + m_{\pi}/2)}{2\epsilon} \approx 6.8 \times 10^{19} \left(\frac{\epsilon}{\rm meV}\right)^{-1} \text{ eV} \tag{1.8}$$

In addition to above, there may exist multipion production channels with much lower cross-section [17, 69]. A nuclei undergoing Bethe-Heitler interaction loses energy via $e^{+}e^{-}$ pair production as ${}^{A}_{Z}X + \gamma_{bg} \rightarrow {}^{A}_{Z}X + e^{+}e^{-}$. The threshold energy for this process is two orders of magnitude smaller than that for photopion production and is given by

$$E_{\rm th}^{e^{\pm}} = \frac{m_e c^4(m_X + m_e)}{\epsilon} \approx 4.8 \times 10^{17} A \left(\frac{\epsilon}{\rm meV}\right)^{-1} \text{ eV} \tag{1.9}$$

Beta decay of neutrons, produced in the decay of charged pions, can also contribute to the electron neutrino flux via the process $n \rightarrow p + e^{-} + \overline{\nu}_e$. Heavier nuclei ($Z > 1$) can undergo photodisintegration due to irradiation by photons of energy between $8 - 30$ MeV,

$${}^{A}_{Z}X + \gamma \rightarrow {}^{A-n}_{Z-n'}X + nN \tag{1.10}$$

producing $n(n')$ stripped nucleons (protons) [70, 71]. The cross-section shows a giant dipole resonance near the threshold $\approx$ 8 MeV, corresponding to the extraction of one nucleon. Beyond 30 MeV, the quasi-deuteron process dominates and more than one nucleon is extracted from the nuclei. Photodisintegration is the dominant energy loss process of UHECR nuclei [72, 73], simulated using various cross section models [70, 74]. UHECRs also lose energy during their propagation because of the adiabatic expansion of the universe, given by the following expression for protons:

$$\frac{dE}{dt} = -\frac{\dot{a}}{a}E = -H_0 \left[\Omega_m(1+z)^3 + \Omega_{\Lambda}\right]^{1/2} E \tag{1.11}$$

where a is the scale factor and we consider ΛCDM cosmology in our calculations with $H_0 = 67.3$ km s^{-1} Mpc^{-1}, $\Omega_m = 0.315$, $\Omega_{\Lambda} = 1 - \Omega_m$ [75]. Neutrinos, being weakly interacting, propagate unhindered through the cosmos and experience only adiabatic energy loss due to the cosmic expansion. The photons interact with the cosmic background radiation and the universal radio background (URB) to produce electromagnetic cascades through various processes such as Breit-Wheeler pair production, double pair production, resulting in $e^{+}e^{-}$ pairs [76]. The relativistic cascade electrons lose energy by triplet pair production, synchrotron radiation on deflections in the magnetic field, and up-scattering background photons by inverse-Compton scattering. An elucidating but straightforward model of electromagnetic showers was proposed by Walter Heitler [77], which is used

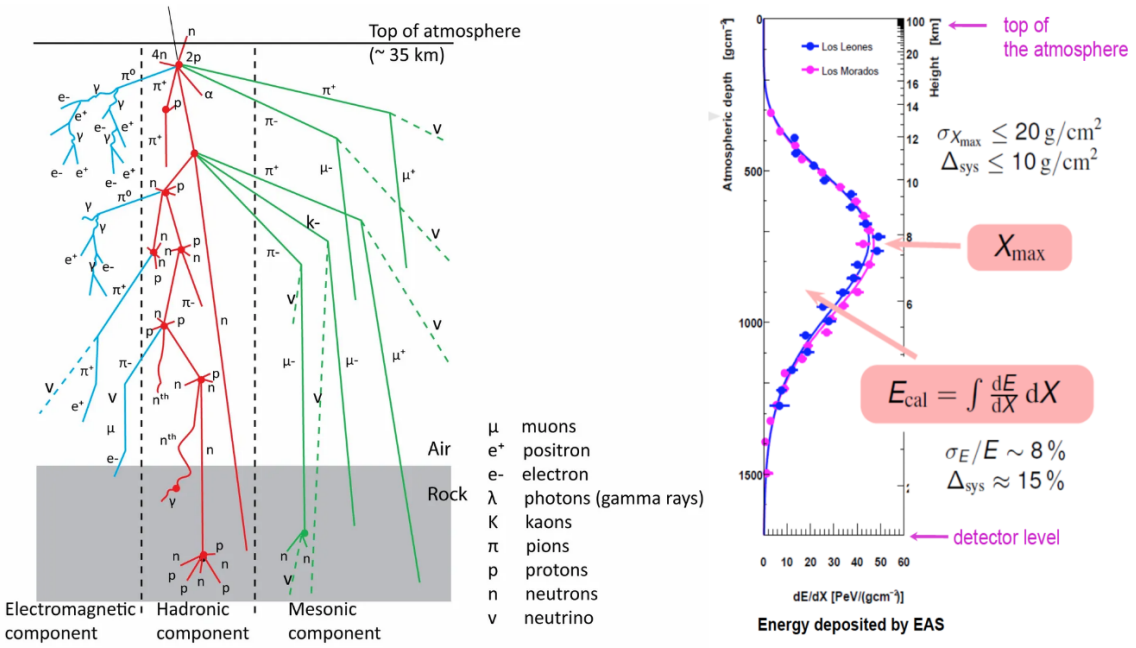

Figure 1.3: *Left:* Schematic diagram showing the electromagnetic component, hadronic component, and mesonic component of the extensive air shower initiated by a primary UHECR particle at the top of the atmosphere. The image is taken from Ref. [84]. *Right:* The longitudinal shower profile indicating the atmospheric depth $X_{\max}$, where the number of secondary particles is maximum. The image is taken from Ref. [85].

widely for the calculation of secondary EM fluxes resulting from the EM cascade of $e^{\pm}$, γ-photons [78–80].

The ankle feature in the propagated spectrum was earlier considered as the reminiscence of e^+e^- pair-production dip caused by UHECR interactions on the CMB [81–83]. However, current measurements disfavor proton dominance beyond the ankle (more detailed discussion in Chapter 2). A more validated formulation considers the transition between two or more different populations of sources as the cause of the ankle phenomenon. Recent observations reveal that UHECRs must originate from redshifts $z \lesssim 0.5$ for them to arrive at Earth with energies greater than the ankle, and also to survive the possibility of photodisintegration. The cutoff at the highest energies can be interpreted as due to increased photopion production on the CMB ($\Delta-$resonance), called the GZK phenomenon, or due to maximum acceleration energy at the sources. However, a UHECR event is not correlated with any astrophysical source, so far. Beyond 4×10^{19} eV, the statistics are low. Hence, the spectral features are still open to speculations.

1.2 UHECR Detection

UHECRs hit the Earth's atmosphere at a rate of one particle per 100 km^2 per century. Hence, to detect UHECR events, an extensive collection area must be employed. In 1939, Pierre Auger discovered the correlated arrival of particles at widely separated points. At

the time, Geiger-Müller (GM) counters were used and Auger concluded that some of the cascades were initiated by PeV cosmic rays. Larger and larger arrays of GM counters were used to detect events up to 10^{17} eV. But little was known about their arrival direction. Soon scintillation counters were used to measure the arrival time of signals about tens of meters apart, and the direction of incidence was reconstructed. In the early 1960s, before the discovery of 2.7 K background radiation, now known as the cosmic microwave background (CMB), it was suspected that the CR spectrum might extend up to 10^{21} eV. The first giant air shower array ($\sim$ 8.1 km^2) at Volcano Ranch in New Mexico was built in 1961, where the first UHECR event of energy 10^{20} eV was detected. Subsequently, a vast array of water Cherenkov detectors spread over an area of 12 km^2 was operated for a year in 1967 at Haverah Park, UK. Gradually the Yakutsk array in Siberia (1970), Fly's Eye detector (1981), and subsequently HiRes instrument in USA (1998), the Akeno Giant Air-Shower Array (AGASA) in Japan (1990) made significant contribution in the development of UHECR detection techniques.

1.2.1 Hadronic cascade

Primary cosmic rays collide with atoms and nuclei on top of the atmosphere and initiate hadronic cascades to produce energetic secondary particles, which interacts further. This chain of interaction continues until the primary particle energy goes below a certain threshold, and only ionization losses dominate. This is commonly known as extensive air shower (EAS) [86], whereby a single primary UHECR particle of energy 10 EeV produces $\sim 10^{10}$ particles spread over 20 km^2 (cf. Fig. 1.3). The number of secondary particles produced as a function of the atmospheric depth (gm cm^{-2}) traversed by the cascade is called the longitudinal profile. The depth at which the number of particles reaches its maximum is called the maximum shower depth $X_{\rm max}$ and is a useful component to deduce the energy and composition of the primary particle. The average shower maximum,

$$\langle X_{\rm max} \rangle = D_e \ln \left(\frac{E}{E_0} \right) \tag{1.12}$$

scales approximately as $\ln(E/A)$ where E is the energy and A is the atomic mass. The dependence on A propagates in the characteristic energy E_0, depending on the primary composition. D_e is the elongation rate of the cascade, i.e., the rate of change of $X_{\rm max}$ with energy. Determining $X_{\rm max}$ is more complex for hadronic showers than in the case of electromagnetic showers, because of the larger cross-section and higher multiplicity at each step, thus reducing the value of $X_{\rm max}$. As a general extension to Heitler's model of pure electromagnetic showers to hadronic cascades, the elongation rate is defined as, $D_{10} = dX_{\rm max}/d\log_{10} E_0$. The fast rate of energy transfer in hadronic showers indicates that the elongation rate of EM showers (D_{10}^{γ}) is an upper limit to the elongation rate of hadronic showers. This postulate is known as the elongation rate theorem [87]. The shower maximum for protons occur deeper in the atmosphere than for an equivalent

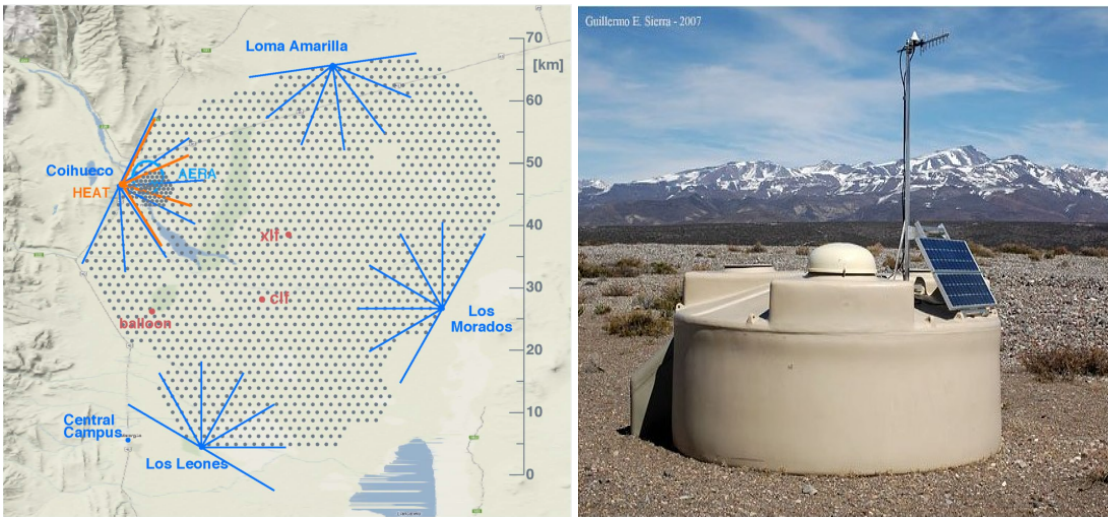

Figure 1.4: *Left:* The map of the Pierre Auger observatory, showing the surface detector stations in black dots. The blue lines indicae the field of view of the fluorescence telescopes at the four sites. *Right:* A single water-Cherenkov tank of diameter 3.6 m, water depth 1.2 m, and contains three photomultiplier tubes at the top surface. There is also a communication antenna attached to each station. Image courtesy: Pierre Auger Observatory.

energy iron nucleus, i.e., $\langle X^{p}_{\rm max}\rangle > \langle X^{Fe}_{\rm max}\rangle$. The changes in the primary composition are derived from the observed breaks in the elongation rate.

The number of secondary particles in the cascade grows with subsequent generation of interactions. At each generation vertex, $\sim$ 30% of energy is carried by the EM cascade stemming from the spontaneous decay of the neutral pions (π^0). Cumulatively, $\sim$ 90% of the total primary particle energy is dissipated via EM cascade. Only the remaining energy is carried by muons ($\mu^{\pm}$) and neutrinos ($\nu_{\rm e}$, ν_{μ}) from charged pion ($\pi^{\pm}$) decay. Unlike the electromagnetic component of the hadronic cascade, the number of muons is not linearly proportional to the primary particle energy. This is because the pions ($\pi^{\pm}$) need to cool sufficiently so that they will decay before interacting any further. Thus, with increasing primary energy, more energy is lost in electromagnetic cascades due to higher interaction generations. Heavier nuclei produce more number of muons compared to protons, $N^{A}_{\mu} \propto A(E/A)^{0.85}$.

1.2.2 Pierre Auger Observatory

The Pierre Auger Observatory (PAO), located near the city of Malargüe in Mendoza province, Argentina, is the world's largest detector for the observation of UHECR particles that hit the Earth's atmosphere with energy above 10^{17} eV [88, 89]. It has measured the energy spectrum, mass composition, and also the arrival direction of primary UHECRs, since 2004. It is situated at an altitude of 1400 m above sea level. Located at a latitude and longitude of 35°.2 S and 69°.2 W, respectively, PAO detects UHECRs incident mostly from the Southern Hemisphere. PAO uses its hybrid detection technique to detect these EAS initiated by extremely energetic particles and reconstructs the primary particle's energy

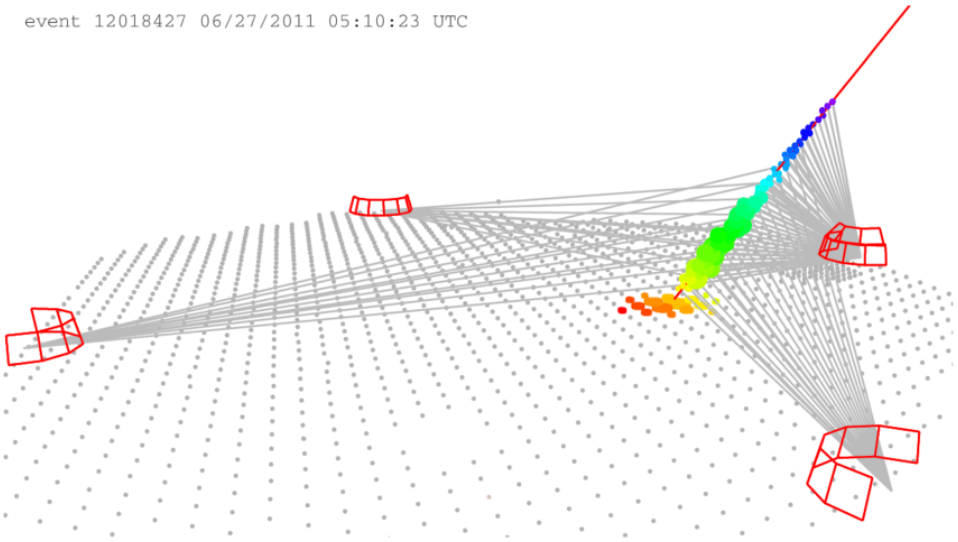

Figure 1.5: Detection of a UHECR event using the hybrid detection technique. Colors indicate the time profile of the shower development until it reaches the ground. Twenty-seven fluorescence telescopes at four sites, including the HEAT telescopes, detect the ultraviolet radiation from the EAS. The image is taken from [91].

along with composition and arrival direction.

PAO combines the data collected by the surface detector (SD) at the ground level resulting from the hadronic cascade with the observation of air shower developments in the atmosphere and by fluorescence detector (FD). The SD array is comprised of 1600 water-Cherenkov detectors, arranged in a triangular grid with 1.5 km spacing (SD-1500 array), spread over an area of ~3000 km^2. There are additional 61 detectors covering an area of 23.5 km^2 with a grid spacing of 750 m (SD-750, 'infill' array), as shown in the left panel of Fig. 1.4. When charged particles enter a station, it induces Cherenkov radiation, which is reflected at the walls by a diffusive Tyvek liner. Three photomultiplier tubes on the top of each water-Cherenkov tanks sample the shower signal using the electromagnetic and muonic components. Each SD tank contains 12 metric tons of ultrapure water. The detectors' responses are recorded in a common calibration unit, called the vertical equivalent muon (VEM) [90]. It is the signal produced by a muon traversing the water vertically at the center of the station. Air showers are detected when a triangle of neighboring stations is triggered simultaneously. The angular resolution is $0^\circ.8$ at $E > 3$ EeV for 1500 m array and 1° for 750 m array. The SD array has almost 100% duty cycle.

The FD is comprised of 27 fluorescence telescopes grouped at four buildings along the boundary of the surface array, that observes the longitudinal development of the air shower by detecting the fluorescence light emitted isotropically by hadronic interactions in the atmosphere. The charged particles produced in an air shower traverses through the universe colliding with atmospheric nitrogen. This produces ultraviolet light by "fluorescence". The fluorescence intensity is observed as a function of atmospheric depth

traveled, to probe the EAS development. Each building contains six telescopes with a $30^\circ \times 30^\circ$ field of view, and each telescope uses Schmidt optics consisting of a wide-angle, segmented spherical mirror of ~ 13 m^2. The light reflected from the mirror is focussed onto a camera consisting of 440 photomultipliers (PMT), capable of detecting showers up to 15 km away. The longitudinal profile of the shower is measured as an image of active PMT pixels along the shower axis [92]. It can operate only during clear moonless nights and has a duty cycle of ~15%. The 750 m array is overlooked by three fluorescence telescopes (HEAT), that can cover elevations from 30° to 60°, aiding the observation of low-energy showers ($E < 10^{17.8}$ eV). The two complementary methods (SD & FD) make up the hybrid detection technique employed to detect UHECRs. FD can better estimate the total shower energy, which is approximately equal to the primary CR energy. Fig. 1.5 illustrates the hybrid detection method of an UHECR event. All 27 telescopes can detect ultraviolet light and Cherenkov radiation.

1.2.3 Telescope Array experiment

In addition to the PAO in Southern Hemisphere, another experiment called the Telescope Array (TA) in Utah, United States (39°.3 N, 112°.9 W, 1400 m above sea level) is also capable of detecting UHECR events, using the same hybrid detection technique [93, 94]. It detects UHECRs above 10^{18} eV using the surface array spread over 780 km^2 and employing more than 500 scintillation detectors located on a 1.2 km square grid. Three fluorescence stations are arranged over a 30 km triangle, each hosting 12-14 telescopes. The fluorescence telescopes detect the scintillation light produced as the shower propagates through the gas in the atmosphere. The surface array measures the density of secondary particles in an EAS, and the scintillation molecules within the detector are excited by their incidence. Eighty-seven events were recorded above 57 EeV, with a zenith angle of arrival direction less than 55°, during the period from May 2008 to May 2014. The statistics of events observed are lower than those recorded by PAO at the highest energies, owing to the smaller effective exposure area.

1.3 Neutrinos & Gamma-rays

The diffuse γ-rays detected by *Fermi*-LAT space instrument in the energy range between MeV and ~ TeV suggests some connection between the production of cosmic rays and γ-rays. The latter, if produced in photohadronic interactions, also hint towards a diffuse astrophysical neutrino flux. Indeed, IceCube Neutrino Observatory at the Antarctic ice sheet in South pole has discovered a diffuse high-energy neutrino background of astrophysical origin, at multi-TeV to PeV energies [95]. All these messengers are complementary to each other, carrying the information of the same inherent astrophysical phenomenon. Cosmic rays and neutrinos are the messengers of strong and weak nuclear forces. Multi-messenger astronomy thus uses messengers of other fundamental forces of nature, in addition to that of electromagnetic forces, the photons.

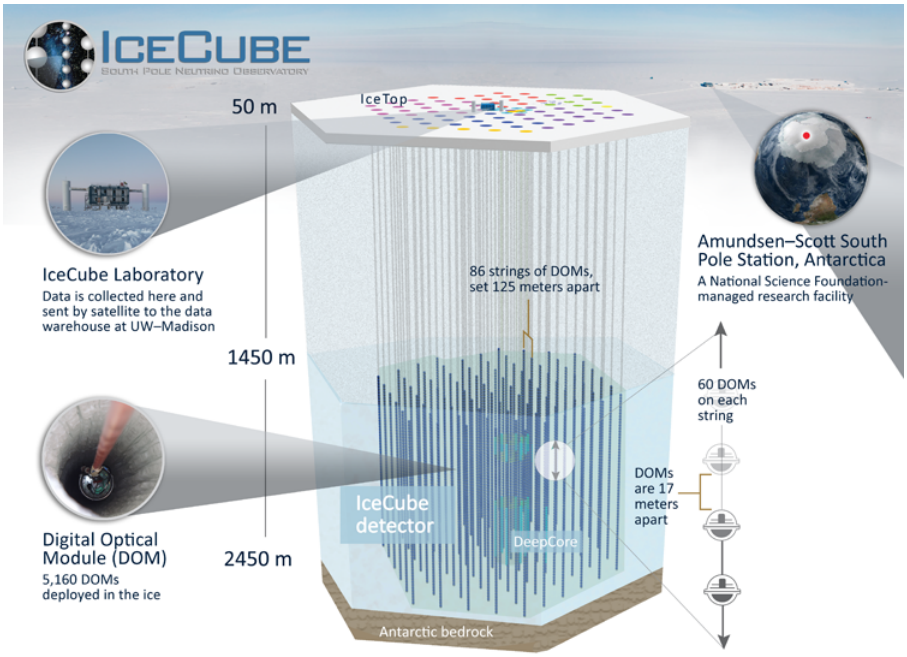

Figure 1.6: Schematic diagram showing the components of IceCube Observatory at South Pole ice, viz., the surface array IceTop, the IceCube array, and the low-energy sub-array DeepCore. Image courtesy: IceCube Neutrino Observatory.

1.3.1 Neutrino astrophysics

The IceCube Neutrino Observatory at the South Pole has been operating in its full configuration since 2011. It instruments approximately a cubic kilometer of the Antarctic ice sheet at a depth between 1450 m and 2450 m, consisting of 5160 digital optical modules (DOMs) attached to 86 strings in a 3D hexagonal array. These DOMs detect the Cherenkov photons emitted by charged particles traveling at a speed greater than that of light in ice. The DOMs have a vertical separation of 17 m, and the strings are placed 125 m apart [42]. This configuration allows IceCube to detect neutrinos above 100 GeV. The IceTop surface array consists of 162 water tanks filled with clear ice that identifies the CR air showers developing in the atmosphere. IceCube is capable of measuring the anisotropy in CR arrival directions at TeV to PeV energies. A more densely instrumented volume at the central and deeper part of the IceCube array called DeepCore extends the IceCube operation threshold down to 10 GeV energies. DeepCore enables IceCube in probing neutrino oscillation properties and dark matter searches.

The neutrino flavors at IceCube are classified based on the event topology, shown in Fig. 1.7. Charged-current (CC, involving the exchange of a Z boson) interactions of muon neutrinos with water molecules within the detector volume produces muons ($\nu_\mu + n \rightarrow \mu^- + p$) moving at ultrarelativistic speed. This muon emits Cherenkov radiation, which is recorded by the DOMs as a track and hence are called "track-like" events. In neutral-current (NC, involving the exchange of a W boson) interactions, the neutrino

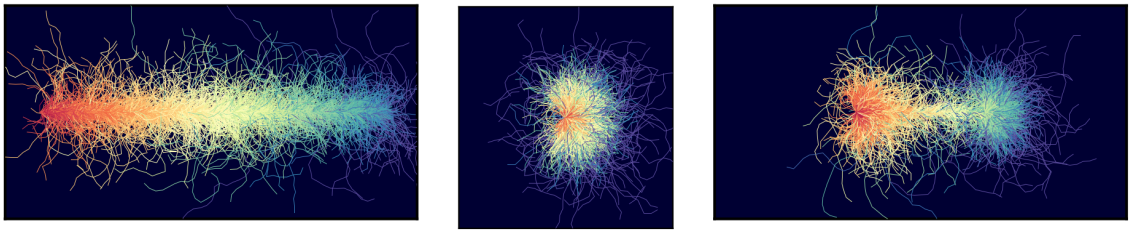

Figure 1.7: Simulations of Cherenkov light propagation in the Ice for various types of signatures, viz., a track-like event (left), a shower-like event (middle), and a double-bang event (right). The image is taken from Ref. [42].

remains a neutrino but transfers energy and momentum to a target particle before leaving the detector. "Shower-like" events are produced by NC interactions of all neutrino flavors and CC interactions of ν_e (all energies) and ν_τ ($E \leqslant 100$ TeV). The electron loses energy very fast and creates a spherical light pattern. High-energy ν_τ events exhibit a distinct signature, called the "double-bang" events. The τ generation vertex and the τ decay vertex can be identified separately when the track is longer than 20 m, and both vertices are contained within the detector volume [96].

Although an isotropic flux of astrophysical neutrinos has been observed, a neutrino point source is yet to be detected. The diffuse flux from cosmic sources can be found by integrating the spectral emission rate density Q_ν over redshift,

$$\phi_\nu(E_\nu) = \frac{c}{4\pi}\int_0^\infty \frac{dz}{H(z)} Q_\nu(z, E_\nu(1+z)) \quad \text{GeV}^{-1}\text{s}^{-1}\text{cm}^{-2}\text{sr}^{-1}. \tag{1.13}$$

Here $H(z)$ is the redshift-dependent Hubble expansion rate. We can write, $Q_\nu = \rho(z)Q_\nu(E)$, where $\rho(z)$ is the source density as a function of redshift. The luminosity distribution is not taken into account in this simplistic approach. The source spectra can be considered a power-law of the form $Q_\nu(E) \propto E^{-\gamma}$. The observed per-flavor diffuse flux is at the level of $E^2\phi_\nu \simeq 10^{-8}$ GeV s^{-1}cm^{-2}sr^{-1}. From this value, the average neutrino point-source luminosity can be calculated using Eqn. 1.13. The IceCube sensitivity to continuous point-source emission in the Northern Hemisphere is $E^2\phi^{\text{PS}}_{\nu_\mu+\overline{\nu}_\mu} \approx 10^{-12}$ TeV cm^{-2}s^{-1}. The single power-law model yields a best-fit spectral index $\gamma = -2.5$ for the diffuse astrophysical neutrino flux between 10 TeV and 2 PeV (cf. Fig. 1.8, grey-shaded region) [97]. Fig. 1.8 shows that the maximum contribution from 2LAC blazars is 19%–27%, assuming an equal weighting of γ-ray and neutrino flux. This is indicated for two different values of power-law index, viz., $\gamma = -2.2$ (green-shaded region), and $\gamma = -2.5$ (blue-shaded region) [98]. The upper-limit band width considers the dependence on the relative distribution of neutrino luminosities in the blazar sample. If a strict proportionality is assumed between the γ-ray flux at GeV energies and the neutrino intensity at TeV energies, the contribution from blazars is $\sim 10\%$ of the observed flux.

There can be another possible origin of the diffuse flux of cosmic neutrinos. UHECRs

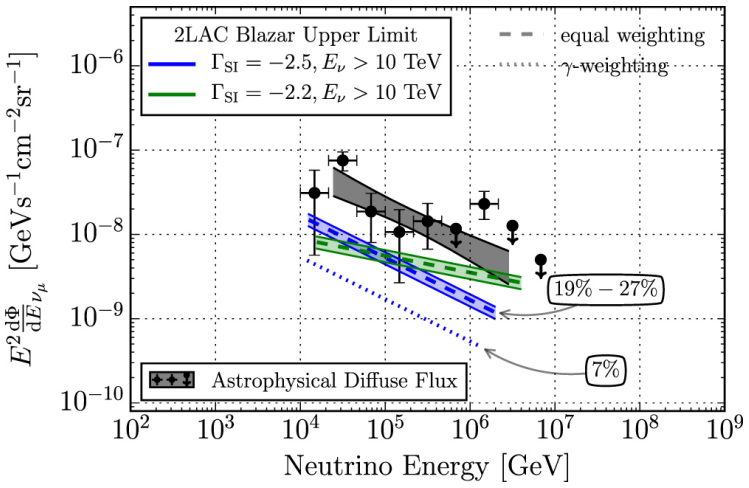

Figure 1.8: The data points show the observed astrophysical diffuse neutrino flux. The grey shaded region corresponds to 68% C.L. allowed region for the single power-law model, $\Phi_\nu = \phi(E/100\,\text{TeV})^{-\gamma}$. The flux upper limit from 2LAC blazars is shown using equal weighting for a power law with spectral index 2.5 (blue-shaded region) and 2.2 (green-shaded region).

undergo photopion production with CMB and EBL photons during propagation over extragalactic distances. The charged pions decay to produce neutrinos. Cosmogenic neutrinos are a "guaranteed" contribution to the high-energy neutrino flux, independent of the neutrino production mechanism inside astrophysical sources. The flux of neutrinos is highest for proton-dominated UHECR composition models. The neutrino flux of flavor i generated from the propagation of cosmic rays over cosmological distances can be expressed as an integral over redshift and proton energy E_p^s at the source [2],

$$\mathcal{F}_i(E_{\nu_i}) = \frac{c}{4\pi E_{\nu_i}} \int\int \mathcal{L}(z, E_p^s)\mathcal{Y}(E_p^s, E_{\nu_i}, z)\frac{dE_p^s}{E_p^s}dz \tag{1.14}$$

where the neutrino yield function and the source function per unit redshift is given by

$$\mathcal{Y}(E_p^s, E_{\nu_i}, z) = E_{\nu_i}\frac{dN_{\nu_i}}{dN_p dE_{\nu_i}}\,; \qquad \mathcal{L}(z, E_p^s) = \mathcal{H}(z)\eta(z)\mathcal{L}_0(E_p^s) \tag{1.15}$$

where $\mathcal{H}(z)$ parametrizes the cosmological source evolution, $\eta(z)$ describes the cosmological expansion, and $\mathcal{L}_0(E_p^s)$ is the source injection spectrum. About 60% of the final neutrino flux is generated within the first 50 Mpc of UHECR propagation. IceCube is capable of detecting cosmic neutrino signals beyond EeV energies. At these extreme energies, background events from atmospheric interactions are also absent. But any signature of cosmogenic neutrinos is yet to be observed. The flux upper limit from non-observation of cosmogenic neutrinos disfavors some of the proton dominated GZK models at the highest observed UHECR energies [99–101].

1.3.2 Gamma-ray constraints

The cosmic background light is dominated by the most abundant CMB photons, the thermal relic radiation from the last scattering surface. EBL consists of starlight at optical

wavelengths, thermal dust radiation in the infrared zone, and emission from AGNs in X-rays. However, the extragalactic γ-ray background (EGB) is completely non-thermal and the message-bearer of the high-energy universe. The diffuse background (IGRB), i.e., excluding the resolved sources from EGB, the nearly isotropic radiation comes from sources such as unresolved blazars and GRBs, star-forming galaxies, misaligned AGNs, millisecond pulsars, etc. A detailed account of the relative contribution of individual source classes is discussed in Ref. [102], and the references therein. Nonetheless, these are only a few of the vast ensemble of γ-ray sources that make up the EGB spectrum. The decay of neutral pions and the EM cascade of e^+e^- pairs, resulting from UHECR interactions, are efficient hadronic channels of γ-ray production, peaking at ~TeV energies. *Fermi*-LAT has measured the IGRB spectrum from 100 MeV up to 820 GeV [103]. The brightest γ-ray blazars do not appear as the brightest neutrino sources, a puzzle yet to be understood. Hence, the constraints from cosmogenic photons are still vague. They depend on UHECR source evolution with redshift, composition, and most importantly, the intensity of magnetic fields they propagate through [104]. We will come back to this in Chapter 2 and 3.

1.4 Current State of Reserach

This section summarises the recent advancements in the field of ultrahigh-energy cosmic rays and pertinent implications in astroparticle physics and high-energy astrophysics, in general. We consider them as the guidelines and motivation to continue research on the subject. We explore the UHECR mass composition from the relative dominance of heavy nuclei at the highest energies. The cosmogenic neutrino and photon flux upper limit imposed by IceCube and *Fermi*-LAT provides essential constraints to such a study (cf. Chapter 2). We check the feasibility of UHECR acceleration in TeV blazars, from consistent modeling of multiwavelength data showing unattenuated γ-ray emission. We investigate the multi-messenger connections between cosmic rays, neutrinos, and photons from line-of-sight UHECR interactions producing the observed γ-ray signal in the VHE regime (Chapter 3). We show that the composition prediction of the UHECR spectrum is compatible with a light nuclei component extending up to the highest-energy bin, in addition to a heavy nuclei injecting source population. We calculate the maximum allowed proton fraction near the cutoff at 3.5σ confidence level (cf. Chapter 4).

1.4.1 UHECR energy spectrum

At 60 EeV, the distance of 50% survival for UHECRs is smaller than 100 Mpc for H or Fe, and 20 Mpc for intermediate-mass nuclei [106]. The Pierre Auger Observatory reconstructs the longitudinal profile of the energy deposit (dE/dX) by the air shower in the atmosphere (cf. Fig. 1.3). Thereby, the amount of energy lost by the primary particle is $E_{\rm cal} = \int (dE/dX) dX$. The total energy ($E_{\rm tot}$) is obtained by adding the energy carried to the ground ($E_{\rm inv}$) by high energy muons and neutrinos. The observed profile of dE/dX

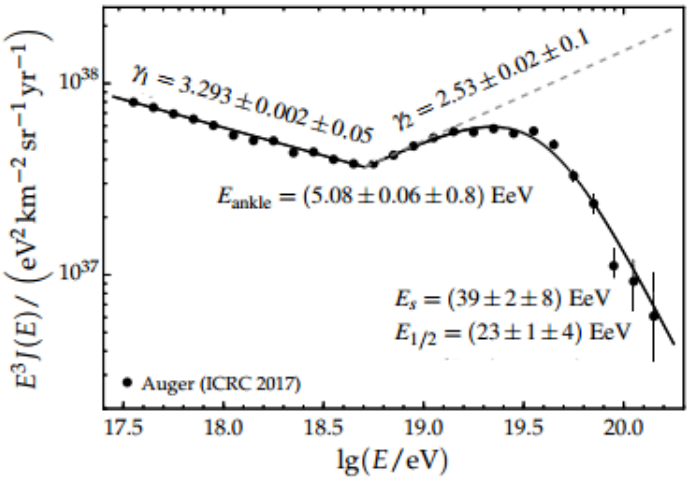

Figure 1.9: The combined UHECR energy spectrum data and the fit function. The best-fit values of the fit-parameters are also indicated. The image is taken from Ref. [105].

is fitted using the Gaisser-Hillas (GH) function [107]. But often for low-energy showers, only a part of the energy deposition is intercepted by PAO. Correction procedures are adopted to resolve such problems and to improve the energy calibration of SD and FD. Also, data samples are refined to include inclined air showers, where the EM component is absorbed by the atmosphere, and muons dominate the SD signal. [105]. A likelihood function is defined that fits four types of data sets, viz., SD 1500 vertical ($\theta_z < 60°$), SD 1500 horizontal ($\theta_z > 60°$), SD 750, and the hybrid detection including both SD and FD. The combined energy spectrum obtained from maximum likelihood analysis is shown in Fig. 1.9. The ankle and cutoff feature can be seen as prominent features at $10^{18.7}$ eV and $10^{19.6}$ eV, respectively. The following function fits the combined spectrum,

$$J(E) = \begin{cases} J_0 \left(\dfrac{E}{E_{\rm ankle}}\right)^{-\gamma_1} & (E \le E_{\rm ankle}) \\ J_0 \left(\dfrac{E}{E_{\rm ankle}}\right)^{-\gamma_2} \left[1 + \left(\dfrac{E_{\rm ankle}}{E_{\rm s}}\right)^{\Delta\gamma}\right] \left[1 + \left(\dfrac{E}{E_{\rm s}}\right)^{\Delta\gamma}\right]^{-1} & (E > E_{\rm ankle}) \end{cases} \tag{1.16}$$

The best-fit values of the parameters are also indicated in the figure. The first error corresponds to statistical uncertainties, while the second is due to systematic uncertainties. The latter is dominated by the energy calibration error of $\sim$ 14%. The fit uses the data collected from January 2004 to December 2016, thus using a total exposure exceeding 67,000 km^2 sr yr. The error is greatly reduced below $\log_{10}(E/\mathrm{eV}) = 19.5$. The uncertainties at the highest energies are due to low statistics. The systematic uncertainty due to energy calibration is 14% for Auger and 21% for TA experiment. The spectrum reported by both experiments conform with each other in the energy range between $10^{18.4} - 10^{19.4}$ eV, if the Auger energies are increased by 5.2% and the TA energies are reduced by 5.2%. These shifts are well within the respective energy scale uncertainties. However, a large disagreement remains above $\simeq 10^{19.5}$ eV, in the cutoff region [108].

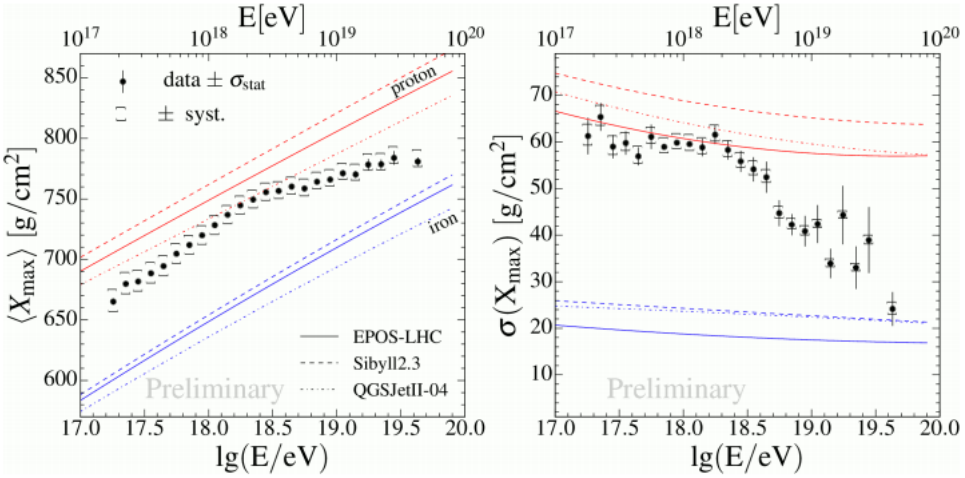

Figure 1.10: The mean (left) and standard deviation (right) of the maximum shower depth distribution, as a function of energy. The corresponding values of proton and iron primaries, obtained from air shower simulations, for various hadronic interaction models are also shown. The figure is taken from Ref. [105].

1.4.2 UHECR mass composition

The mass composition of UHECRs is essential to understand the transition from Galactic to extragalactic cosmic rays and to reveal the dominant physical processes at various energies. The rigidity of heavier nuclei is lower for a given maximum acceleration energy at the sources, constraining them to originate from near-extragalactic sources. The composition fractions are derived from the distribution of the depth of shower maximum X_{max}, measured by the fluorescence detectors at the PAO [109]. The HEAT telescopes have expanded the field of view of the Coihueco site (CO) and allow the observation of showers down to $10^{17.2}$ eV. The first two moments of X_{max} are calculated by the following equations and fitted with four elemental groups ^{1}H, ^{4}He, ^{14}N, and ^{56}Fe.

$$\langle X_{max} \rangle = \langle X_{max} \rangle_p + f_E \langle \ln A \rangle \tag{1.17}$$

$$\sigma^2(X_{max}) = \langle \sigma^2_{sh} \rangle + f_E^2 \sigma^2(\ln A) \tag{1.18}$$

Here, $\langle X_{max} \rangle_p$ and $\langle \sigma^2_{sh} \rangle$ represents the mean X_{max} for protons and the composition-averaged shower-to-shower fluctuations, respectively. f_E is a parameter that depends on the hadronic interaction models. It can be noted from Fig. 1.10, the value of observed X_{max} shows a steepening beyond $\log_{10}(E/\text{eV}) = 18.5$, implying that the proton fraction decreases with increasing energy for all the post-LHC hadronic models. The fluctuations in X_{max} also show a decline above $10^{18.3}$ eV. It is thus inferred that UHECR composition becomes progressively heavier with increasing energy. The shower propagation codes, eg., CORSIKA [110] , CONEX [111], etc., depends on the air-UHECR interaction cross-sections. For EPOS-LHC [112–115] and SYBILL2.3C [116–121] models, N dominates at $10^{19.6}$ eV, but for QGSJET-II.04 [122–127] it is found that He makes up for the total

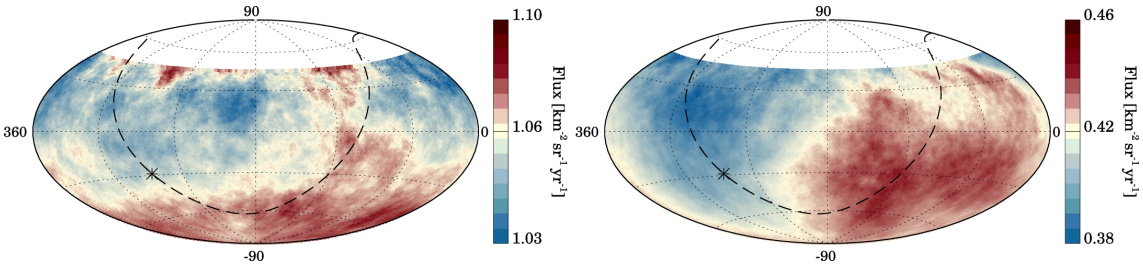

Figure 1.11: Maps of UHECR flux smoothed in windows of 45°, shown by a hammer projection in equatorial coordinates. The left and right panels correspond to the energy bins [4, 8] EeV and $E \geqslant 8$ EeV, respectively [130].

composition fraction at the highest energy bin. The interaction cross-sections are derived by extrapolation of hadronic interactions in laboratory accelerators to higher energies [128, 129]. However, the interpretation of shower development may change with a change in this extrapolation. Auger probes hadronic interactions at center-of-mass energies up to $\sqrt{s} \sim 400$ TeV, while terrestrial accelerators can go up to 13 TeV.

1.4.3 Anisotropy in arrival directions

The location of UHECR sources can be most efficiently identified from the anisotropy in their arrival directions, i.e., looking for clustering of events from any particular direction. However, CRs being charged particles are deflected from their source direction by Galactic and extragalactic magnetic fields (GMF and EGMF), the magnitude of which are still uncertain [131, 132]. A 60 EeV proton traveling a distance of 50 Mpc undergoes a deflection of few degrees in an EGMF of rms value 1 nG [133]. An order of magnitude estimate can be obtained by using the relation,

$$\Phi_{\rm rms} \approx 4^\circ \frac{60\ {\rm EeV}}{E/Z} \frac{B_{\rm rms}}{10^{-9}\ {\rm G}} \sqrt{\frac{D}{100\ {\rm Mpc}}} \sqrt{\frac{l_c}{1\ {\rm Mpc}}} \tag{1.19}$$

where l_c is the turbulent correlation length of the magnetic field, and D is the distance traveled. The cosmic magnetic field models are derived from the large scale structure (LSS) simulations of the universe [134–136]. The Galactic magnetic fields are parametrized by using the Faraday rotation and starlight polarization measurements [137–139]. Telescope Array collaboration has reported a "hotspot" observed in the northern sky with 5.1σ statistical significance, wherefrom an oversampling of events compared to the background is evident over 20° radius circles [140]. Hints of intermediate scale ($\sim 10^\circ - 20^\circ$) anisotropies have also been observed by PAO above 40 EeV, viewed as localized flux excess. Nevertheless, a significant excess around the Galactic center, the Galactic plane, or the Super-Galactic plane was not found. Thus, UHECRs at such high energies must be extragalactic, arising from a source distribution away from the Super-Galactic plane, provided the magnetic field deflections are not substantial [141]. A large-scale ($\sim 45^\circ$) anisotropy is obtained from the analysis of 3×10^4 UHECR events with energies above

8 EeV. The observed anisotropy distribution is compatible with a dipolar modulation of amplitude $d = 6.5^{+1.3}_{-0.9}$ %, pointing towards $(\alpha_d, \delta_d) = (100°, -24°)$ [142]. A less statistically significant dipole is also seen for 4 EeV < E < 8 EeV. Fig. 1.11 shows the UHECR flux in equatorial coordinates for both energy ranges.

1.5 Thesis Objectives

1.5.1 Motivation of UHECR research

We summarize below the motivation for surveying the origin and propagation of UHECRs. Thus, the foundations are laid that guide the research work undetaken.

- Despite the considerable progress in model predictions, numerical and simulation methods to understand the propagation and interaction of UHECRs, the correlation of a UHECR event with an astrophysical source is yet to be made. The dipolar modulation in event rates, observed at large angular scales, provides strong evidence that the magnetic field alone cannot yield an anisotropic flux from an initially isotropic distribution. If Galactic sources in the disk were capable of accelerating cosmic-ray particles to ultrahigh energies, then the dipole amplitude in the range 4 EeV < E < 8 EeV must be larger than the current estimate. The dipole at E > 8 EeV points at a direction, which is ~ 125° away from the Galactic center. All these pieces of observational facts put together yield a smoking gun evidence of the extragalactic origin hypothesis.

- The propagation distance will play an important role in the spectral features and the produced cosmogenic neutrino and γ-ray fluxes. However, such fluxes cannot be deduced independently of the mass composition and cutoff energy at injection. The source parameters, in turn, depend on the potential candidates of UHECR acceleration. AGN jets are modeled to be viable sites because of the high source emissivity and number density. But the blazar subset alone is incapable of explaining the UHECR spectrum, although they can significantly contribute to the diffuse neutrino and photon background. Catalog-based correlation studies have identified overdensities in event rates at $E > 10^{19.6}$ eV from the direction of starburst galaxies. The EGMF can vary over several orders of magnitudes in cosmic filaments, galaxy clusters, and voids.

- The transition from Galactic to extragalactic cosmic rays occurs at some point in between the knee and ankle. The knee at 3×10^{15} eV may result from the inefficient cosmic-ray diffusion through the Galactic disk magnetic field or the maximum acceleration energy of Galactic sources. A series of knee features at different energies must occur due to heavier mass nuclei if protons induce the steepening at 3 PeV. KASCADE-Grande has provided indications of an "iron-knee" at 100 PeV from analysis of their observed data [143]. Beyond this second knee, the composition

becomes lighter as we approach the ankle, and then again starts to become heavier at energies $E > 10^{18.3}$ eV. But, the UHECR rigidity increases with energy, implying that the increase in UHECR mass is slower than the rise in energy [38].

1.5.2 Aim of the thesis

The above-mentioned advancements and limitations in UHECR studies have paved the way for further research in this field. We try to establish a framework that answers the following questions.

- *Chapter 2:* Is it possible to explain the entire UHECR spectrum using a light nuclei composition consisting of H and He? Since post-LHC air shower models compel us to disapprove of a pure proton composition, how significant is the change in cosmogenic neutrino flux predictions in H+He model? Can neutrino flavor identification act as a discriminator of composition models? What source population can explain the sub-ankle spectrum in the case of heavy nuclei injection? Which processes lead to the formation of ankle and cutoff phenomena in the spectrum?

- *Chapter 3:* Since photons from extreme blazars are attenuated by EBL absorption, can line-of-sight UHECR interactions produce the observed γ-ray signals at the very high-energy range? What are the conditions for UHECR acceleration and escape in such sources? What can we infer about the EGMF from the survival of UHECRs along the direction of propagation? What are the prospects of cosmic-ray and neutrino detection (multimessenger studies) under such a lepto-hadronic scenario? How does the luminosity budget hold compared to the Eddington limit?

- *Chapter 4:* In the absence of a model-independent method to probe the UHECR composition, can we improve the composition fit by the addition of a light nuclei component that extends up to the highest observed energies? How does it affect the parameters of the second population injecting light-to-heavy nuclei? What is the statistical significance of improvement in such a two-population source model compared to the one-population model? Can we detect the GZK neutrinos in the future from the proton injecting sources? What can we infer from this about the cutoff in the UHECR spectrum?

We delve into the answer to these questions in the following chapters. We use the Monte Carlo simulation tool CRPROPA 3, for the extragalactic propagation of UHECRs [144] from their sources to the Earth. The simulation allows us to mimic suitable astrophysical environments, by including various energy loss processes of UHECRs through a modular structure. Additionally, it is possible to add EGMF of various types and incorporate templates of GMF. Source classes or point sources can be defined with intended injection parameters. Cosmological effects and adiabatic expansion of the universe are

taken into account. The secondary neutrino and electromagnetic (EM) particles can also be stored and propagated. The cascade development by EM particles can be analyzed using a shipped version of external codes like DINT [145] and EleCa [146]. Additionally, they can be propagated by inherent interaction modules within the CRPROPA simulation chain [147]. More details on the cascade calculations are provided at respective places within the research work. The CRPROPA code allows shared memory multiprocessing using OpenMP. The modules are written in C++ and can be used from a Python interface.

All the analysis codes for modeling the UHECR spectrum and composition were written and developed using Python library functions Numpy and SciPy. Numerical methods and techniques used for integration, interpolation, differential equations, etc., were also done using Python programming. NAIMA [148] and GAMERA [149] codes were used for modeling of non-thermal radiation spectrum from γ-ray sources. Appropriate reference of data files, wherever used for analysis purposes, are duly mentioned. We discuss the impact of our results and draw our conclusions in Chapter 5. The scope of multimessenger observations and future upcoming experiments are also discussed in brief.

2

UHECR Composition & Cosmogenic Neutrinos

The spectrum of UHECRs at $E \gtrsim 0.1$ EeV possesses interesting features. The most notable ones are the hardening of the spectrum near the "ankle" at around $5 \cdot 10^{18}$ eV and a flux suppression at $6 \cdot 10^{19}$ eV, followed by a sharp decline in the number of observed events, called the "cutoff". The proton dip model predicts that UHECRs near the cutoff are protons, accelerated by sources with a steep injection spectral index ($\alpha \gtrsim 2.0$) within the GZK sphere, and they propagate through the extragalactic space to reach Earth. In such a model the ankle is formed due to e^+e^- pair production losses (Bethe-Heitler interaction) of UHECR protons on the CMB. The spectral cutoff in this case occurs as a consequence of the $p\gamma$ interaction on CMB photons through the Δ-resonance channel, known as the "GZK phenomenon". However, current observations of the maximum shower depth distribution ($X_{\rm max}$) by PAO finds that the composition becomes progressively heavier with energy beyond $2 \cdot 10^{18}$ eV [150]. In such a scenario, the contribution at the highest energy comes from heavier nuclei, indicating the sources to be situated in nearby galaxies.

2.1 Background

Since the deduction of $X_{\rm max}$ from shower simulations depend on hadronic interaction models, the uncertainties in composition prediction of UHECRs is considerable [129]. For some hadronic models, the $\langle X_{\rm max} \rangle$ fit reveals a composition between H and He at $\approx 10^{18.2}$ eV, and the highest-energy bin corresponding to $10^{19.5} - 10^{20.0}$ eV is dominated by nuclei between He and N. While for other models this corresponds to intermediate-mass nuclei between N and Fe. But the measure of shower-to-shower fluctuation $\sigma(X_{\rm max})$ indicates a mass composition between H and He at $10^{19.5}$ eV for all UHECR-air interaction models and between He and N in the highest-energy bin ($10^{19.5} - 10^{20.0}$ eV) [151]. A combined fit analysis of the spectrum and mass composition performed by PAO, above the ankle $E \approx 5 \cdot 10^{18}$, explores several combination of UHECR propagation models, photodisintegration cross-section, and EBL models; with a mixed composition of representative elements ^{1}H, ^{4}He, ^{14}N, ^{28}Si, and ^{56}Fe at injection [151, 152]. The best-fit obtained with a homogeneous source evolution corresponds to a hard spectrum $\alpha \lesssim 1$. For all cases, the best-fit Fe fraction is found to be zero. Here the ankle is interpreted as due to a transition between two (or more) different class of sources. Also, the low value of maximum rigidity suggests the cutoff arises from maximum acceleration energy at the sources.

A more recent study extends the analysis done by PAO to specific cases of source redshift evolution, viz., AGN, SFR, GRB, and a power-law redshift dependence [153]. A best-fit is found for the power-law evolution model of source emissivity $(1 + z)^m$,

with negative value of the free parameter m. This implies that the number density of sources, and hence their contribution decreases with increase in redshift. Their model too prefers a hard injection spectrum and low values of rigidity cutoff ($R_{\rm cut} < 10^{19}$ eV) for composition at injection dominated by intermediate mass nuclei (N and Si groups). Cosmogenic neutrinos, which provides a guaranteed contribution to the neutrino flux at ultrahigh energies, are a definite probe of UHECR models [154]. Unlike cosmic rays or EM particles, they travel undeviated by magnetic fields and interacts weakly with matter and radiation. Current neutrino detectors [95, 155] have limited sensitivities to neutrinos at energies $> 10^{16}$ eV but plans are underway to construct bigger and more sensitive experiments to detect such energetic neutrinos [156–161]. The upper limits imposed by 9 years of IceCube data can constrain the UHECR source parameters [162].

In this work, we fit the UHECR spectrum with two different composition models. One with H and He at injection, where we fit the data points above $10^{18.2}$ eV up to the highest observed energies. Here the ankle is caused by two phenomena, viz., a changing composition between H and He in some cases of injection spectral indices, and also due to e^+e^- pair production of UHECR protons on CMB photons. In another model, we inject a mixed composition comprising of H, He, N, and Si and fit the spectrum at $E \gtrsim 5 \cdot 10^{18}$ eV. In the latter, the contribution from separate source populations creates the ankle feature. We calculate the cosmogenic neutrino fluxes for all the best-fit cases and constrain the possible values of accelerator parameters [163]. We also calculate the flux of individual neutrino flavors obtained at Earth by virtue of neutrino oscillations. We see that the ratio of fluxes corresponding to individual flavors can act as a discriminator between various UHECR mass composition at injection. We also check the cosmogenic photon fluxes arising from the same photohadronic interactions of UHECRs, as those producing neutrinos. For our allowed best-fit cases, the photon fluxes near ~ 1 TeV energies is found to be lower than the diffuse gamma-ray background measured by *Fermi*-LAT [103].

2.2 Simulation Setup & Analysis Framework

We use a Monte-Carlo simulation framework CRPROPA 3, for the propagation of UHECRs through the Galactic and extragalactic space, from their sources to the Earth [144]. CRPROPA 3 takes into account all energy loss processes, viz., nuclear decay, interactions in cosmic background photons, deflections in GMF or EGMF, and can be implemented selectively based on the astrophysical scenario, owing to the modular structure of the program. The primary and secondary particle yields, such as that of protons, pions, nuclei, charged leptons, neutrinos, and photons can be obtained at the position of the observer and compared with the observed spectra. CRPROPA 3 also allows for the development and propagation of EM cascades through numerical siimulations. The secondary EM particles ($e^{\pm}$, γ) produced from the interactions of CR hadrons could be propagated either via the cosmic-ray transport code DINT [145] or the cascade simulator EleCa [146],

as an external program from within CRPROPA 3. A combined DINT+EleCa propagation is also possible, whereby particles above a particular threshold energy are propagated via EleCa and that below are propagated by DINT. This threshold is chosen typically between $10^{17} - 10^{18}$ eV. Latest updates implemented in the software allows EM particles to be propagated as an integral part of CRPROPA simulation chain, thus fully replacing the EleCa code [147]. For one-dimensional simulations, DINT can be run in combination with EleCa or CRPROPA. Since we compare the cosmogenic photon flux with measured IGRB background at TeV energies, a pure DINT propagation is adopted.

The simulations done here are essentially one-dimensional, considering a null magnetic field. At ultrahigh energies, the cosmic rays interact with background radiation comprised of CMB and EBL. The CMB spectrum and its redshift evolution is well known to a high precision and can be characterized by an isotropic blackbody spectrum with $T \approx 2.73$ K [164]. The EBL models implemented in CRPROPA 3 are Kneiske *et al.* [165], Stecker *et al.* [166], Franceschini *et al.* [167], Finke *et al.* [168], Domínguez *et al.* [169], Gilmore *et al.* [170] and also the upper and lower bounds determined by Stecker *et al.* [171]. We include photopion production, Bethe-Heitler pair production, photodisintegration, nuclear decay, and also energy loss due to adiabatic expansion of the universe. We explore the parameter space in light of the "CTD" propagation model, i.e., with TALYS 1.8 photodisintegration cross section [74] and Domínguez et al. EBL model [169]. We consider elements are injected with energies between $0.1 - Z{*}1000$ EeV from the sources following an exponential cutoff power-law injection spectrum,

$$\frac{dN}{dE} = A_0 \left(\frac{E}{E_0}\right)^{-\alpha} f_{\rm cut}(E, ZR_{\rm cut}) \tag{2.1}$$

where A_0 and E_0 are arbitrary normalization and reference energy, respectively. α is the injection spectral index. The cutoff function can be expressed in the following form

$$f_{\rm cut} = \begin{cases} 1 & (E \leqslant ZR_{\rm cut}) \\ \exp\left(1 - \dfrac{E}{ZR_{\rm cut}}\right) & (E > ZR_{\rm cut}) \end{cases} \tag{2.2}$$

$R_{\rm cut} = E_{\rm cut}/Z$ is the maximum rigidity of injected particles and Z is the nuclear charge. UHECRs lose energy on interactions with both CMB and EBL. We take into account a power-law evolution of source emissivity $(1 + z)^m$, where m is a free parameter. For calculations of electromagnetic cascade via DINT, an rms magnetic field strength of 0.1 nG is considered. The goodness-of-fit of the simulated spectrum with the observed data is calculated using a standard χ^2 formalism,

$$\chi^2_{\rm spec} = \sum_{i=1}^{N} \left[\frac{y_i^{\rm obs}(E) - y_i^{\rm mod}(E; a_M)}{\sigma_i}\right]^2 \tag{2.3}$$

where $y_i^{\rm obs}(E)$ and $y_i^{\rm mod}(E)$ are the observed and simulated values of UHECR flux in the i-th bin corresponding to energy E. The errors in flux are given by σ_i. We add the

asymmetric errors in quadrature and consider $\sigma_i(E) = \sqrt{y_i^{\rm obs}(E)}$ for data points where no error is available.

2.3 Light Nuclei Composition

2.3.1 UHECR parameters

In our first astrophysical scenario, we fit the UHECR spectrum measured by PAO, with only ^{1}H and ^{4}He at injection. In this case, it is possible to explain the entire ultrahigh-energy range for $E > 10^{18}$ eV. We constrain the range of UHECR parameter values allowed in such a case from the cosmogenic neutrino fluxes produced. The parameters varied and their range of values considered in the H+He model is shown in Table 2.1. The rigidity cutoff $R_{\rm cut}$ is varied between 40 – 100 EV in steps of 10 EV. The source spectral index is varied over the discrete values α = 2.2, 2.4, and 2.6. The redshift of the sources z is restricted to $z_{\rm min} \leqslant z \leqslant z_{\rm max}$, where $z_{\rm min}$ = 0.0007 is considered corresponding to the distance to Centaurus A, and $z_{\rm max}$ is varied through 2, 3, and 4. The $z_{\rm max}$ values considered is beyond z = 0.06, the GZK horizon and also extends above $z \simeq 2$, where the star-formation rate peaks. The source evolution index m is varied through 0, 1, 2, and 3. The abundance fraction of H and He is denoted by $K_{\rm H}$ and $K_{\rm He}$ and is restricted by the condition $K_{\rm H} + K_{\rm He}$ = 100%.

Table 2.1: UHECR parameters used for simulations in H+He model

Parameter	Description	Values
α	Source spectral index	$2.2 \leqslant \alpha \leqslant 2.6$
$R_{\rm cut}$	Cutoff rigidity	$40 \leqslant R_{\rm cut} \leqslant 100$ EV
$z_{\rm min}$	Minimum redshift	$z_{\rm min} = 0.0007$
$z_{\rm max}$	Cutoff redshift	$2 \leqslant z_{\rm max} \leqslant 4$
m	Source evolution index	$0 \leqslant m \leqslant 3$
K_i	Abundance fraction	$0.0\% \leqslant K_i < 100\%$
A_0	Flux normalisation	$A_0 > 0$

We adopt a precision of 0.1% for $K_{\rm H}$ and $K_{\rm He}$ in our study. For each possible combination of fixed values $\{\alpha, z_{\rm max}\}$, we find the best-fit value of $R_{\rm cut}$, m, $K_{\rm p}$. Hence the number of parameters varied is three. Considering normalization to be an additional free parameter, the number of degrees of freedom is $N_{\rm d} = 21 - 3 - 1 = 17$, since we fit the simulated spectrum to 21 Auger data points. The highest-energy data point has large error, thus contributing very little to the total χ^2 value. We list all the 36 best-fit cases obtained from the parameter scan in Table 2.2. To select the best-fit cases from this study, we impose the criteria $\chi^2_{\rm spec} < 27.95$, i.e., the cases within 2σ confidence level for 17 degrees of freedom. This condition inevitably disfavors the $m = 0$ cases for $\alpha = 2.2$ and $m \neq 0$ cases for $\alpha = 2.6$. Since PAO suggests a pure-proton composition at the highest energies is unacceptable,

this disfavors the $m = 0$ cases too for $\alpha = 2.6$ and also the $m = 3$ cases for $\alpha = 2.4$.

2.3.2 UHECR energy spectrum

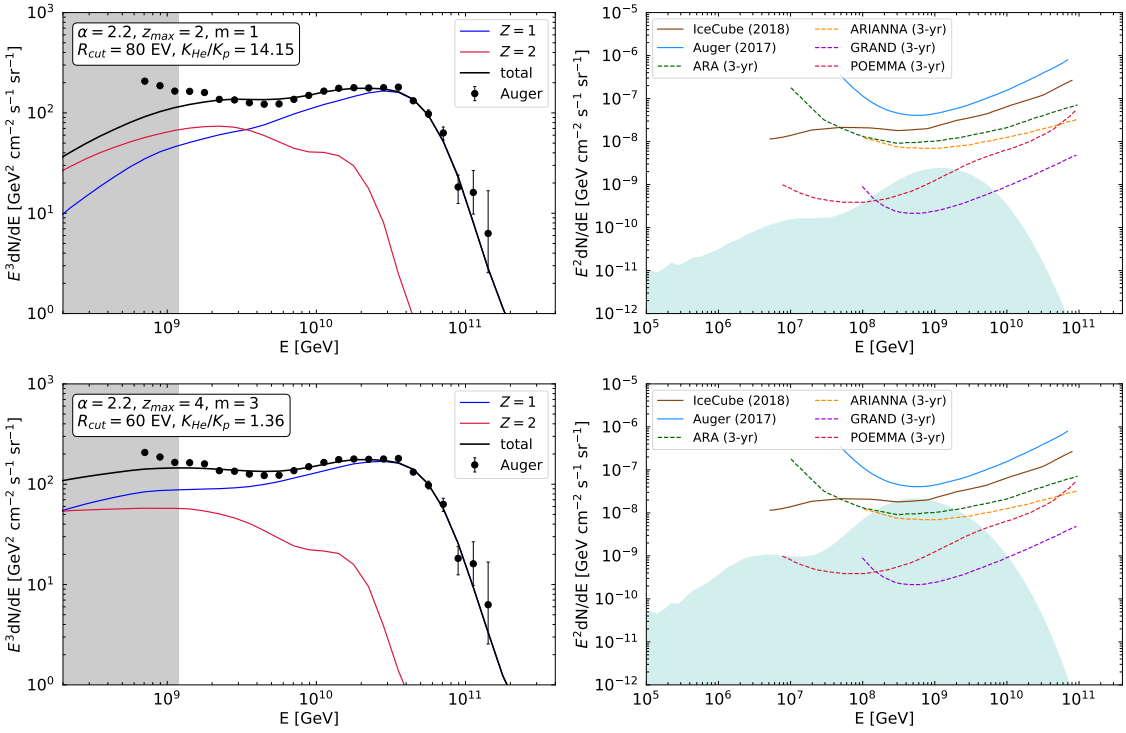

Figure 2.1: UHECR spectra (left) and cosmogenic neutrino spectra (right) for $\alpha = 2.2$. The top (case 2) and bottom (case 12) panels show the best-fit cases listed in Table 2.2 for which the difference in the cosmogenic neutrino flux is the maximum.

From the remaining cases in Table 2.2, we show the UHECR spectra (left) and resulting cosmogenic neutrino fluxes (right) for some of the cases in Figs. 2.1–2.3. We choose the cases corresponding to the minimum and maximum cosmogenic neutrino flux at the higher energy peak for each α value, among the allowed ones based on χ^2 values. The scenario with maximum neutrino flux coincides with the lowest χ^2 values of spectrum fit, for all α. Although all the cases studied here corresponding to $\alpha = 2.6$ are disfavored, we follow the aforementioned trend and display the UHECR spectrum and neutrino fluxes for completeness. The respective cases shown are 2 and 12 from top to bottom in Fig. 2.1; cases 13 and 23 in Fig. 2.2; cases 25 and 33 in Fig. 2.3. The region of the spectrum excluded in the fitting is shaded by grey color. For our choice of the $R_{\rm cut}$ values, the highest energy data points in the spectrum are well covered. The UHECR spectra are shown in E^3dN/dE units (GeV^2 cm^{-2}s^{-1}sr^{-1}) and the neutrino fluxes are plotted in E^2dN/dE units (GeV cm^{-2}s^{-1}sr^{-1}). Some general trends of the UHECR parameters can be observed from the best-fit spectra. These can be listed as follows:

- The ratio of He to H abundance $K_{\rm He}/K_{\rm H}$ decreases with increasing values of α, keeping all other parameters fixed, and for $\alpha = 2.6$, the spectrum corresponds to

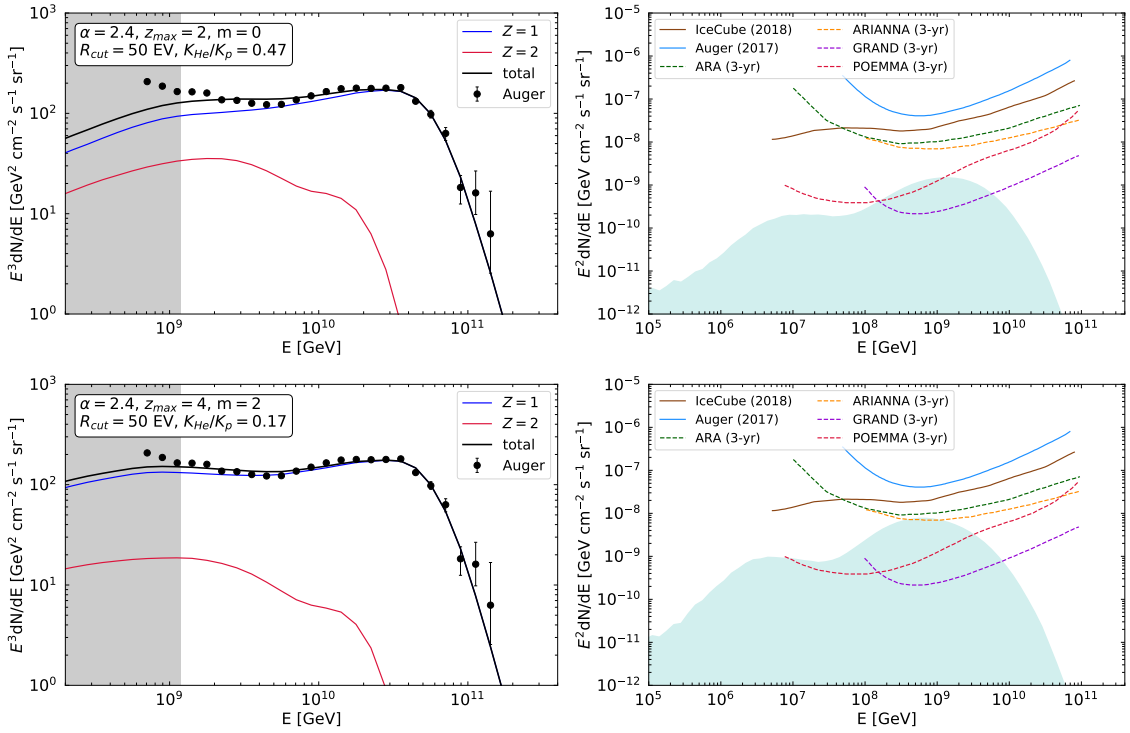

Figure 2.2: UHECR spectra (left) and cosmogenic neutrino spectra (right) for $\alpha = 2.4$. The top (case 13) and bottom (case 23) panels show the best-fit cases listed in Table 2.2 for which the difference in the cosmogenic neutrino flux is the maximum.

Figure 2.3: UHECR spectra (left) and cosmogenic neutrino spectra (right) for $\alpha = 2.6$. The top (case 25) and bottom (case 33) panels show the best-fit cases listed in Table 2.2 for which the difference in the cosmogenic neutrino flux is the maximum.

that of a pure-proton composition.

- He fraction in the observed spectrum decreases sharply beyond a few tens of EeV and proton dominates at the highest energies [172]. Thus the cutoff in the spectrum must be due to photopion production of UHECR protons on CMB.
- For $\alpha = 2.2$, the requirement of He is higher than H. Near the ankle a crossover can be seen between the He spectrum and H spectrum, indicating the ankle feature is generated by a changing composition.
- For $\alpha = 2.6$, ankle feature is generated purely due to e^+e^- pair-production dip, since there is no He at injection. Hence, for steeper injection spectrum the dip model becomes prominent, however, disfavored.
- For higher values of m, there is a hardening of the spectrum in the sub-ankle region. Thus, for a fixed $z_{\rm max}$, increasing m decreases the He fraction at injection, and improves the fit.
- The fit to UHECR spectrum changes only slighly with the variation of $z_{\rm max}$ values considered. Thus UHECRs originating from distances beyond $z_{\rm max} = 2$ have negligible contribution.

The χ^2 values indicated in Table 2.2 suggest the fit becomes progressively better for lower α values. But as we go below $\alpha = 2.2$, it is difficult to fit the spectrum from ~ 1 EeV with only H+He at the sources. We keep the EBL model fixed to Domingüez et al. throughout this study.

2.4 Multi-messenger Constraints

2.4.1 Cosmogenic neutrino fluxes

The cosmogenic neutrino fluxes are calculated by considering all neutrino production channels as described in Sec. 1.1 and using the same normalization factor required to fit the UHECR spectrum. The neutrino fluxes, summed over all flavors are indicated by shaded regions in the right panels of Figs. 2.1–2.3. UHECR interactions on CMB and EBL yield a neutrino spectra with characteristic features. The double-peak shape is obtained due to interactions with separate photon backgrounds. The high-energy peak is caused by resonant photopion production of the highest energy UHECR protons on CMB photons, the so called "GZK neutrinos". EBL photons having energy higher than CMB photons interact with lower energy UHECRs, producing the low-energy peak in the neutrino spectrum. The maximum flux values at the higher energy peak are listed in Table 2.2. We deduce the following features apparent from the neutrino spectra:

- The difference in flux values of high- and low-energy peak is maximum for harder injection spectrum, i.e., $\alpha = 2.2, 2.4$. For steeper injection spectrum, the fluxes at

Table 2.2: Best-fits to UHECR spectrum for H+He composition. Here the peak value of neutrino fluxes are expressed in units of GeV cm^{-2} s^{-1} sr^{-1}.

α	z_{max}	m	R_{cut}(EV)	K_H	K_{He}	K_{He}/K_H	χ^2_{spec}	Case	Neutrino flux	Remarks
2.2	2	0	80	1.7	98.3	57.82	38.41	1	1.385×10^{-9}	Disfavored
		1	80	6.6	93.4	14.15	25.69	2	2.347×10^{-9}	
		2	80	13.2	86.8	6.58	17.06	3	4.366×10^{-9}	
		3	60	42.7	57.3	1.34	12.58	4	8.704×10^{-9}	
	3	0	80	1.3	98.7	75.92	36.34	5	1.488×10^{-9}	Disfavored
		1	90	0.0	100.0	∞	23.69	6	2.809×10^{-9}	
		2	80	12.7	87.3	6.87	15.41	7	5.949×10^{-9}	
		3	70	31.3	68.7	2.19	12.00	8	1.464×10^{-8}	
	4	0	80	1.3	98.7	75.92	37.15	9	1.530×10^{-9}	Disfavored
		1	80	6.2	93.8	15.13	24.37	10	2.983×10^{-9}	
		2	80	12.8	87.2	6.81	15.76	11	7.159×10^{-9}	
		3	60	42.3	57.7	1.36	11.36	12	2.079×10^{-8}	
2.4	2	0	50	67.9	32.1	0.47	21.91	13	1.456×10^{-9}	
		1	50	76.2	23.8	0.31	17.41	14	2.459×10^{-9}	
		2	50	86.4	13.6	0.16	14.39	15	4.524×10^{-9}	
		3	50	99.0	1.0	0.01	12.78	16	9.055×10^{-9}	Disfavored
	3	0	50	68.6	31.4	0.46	20.89	17	1.595×10^{-9}	
		1	50	77.0	23.0	0.3	16.73	18	2.947×10^{-9}	
		2	50	87.5	12.5	0.14	14.05	19	6.301×10^{-9}	
		3	50	100.0	0.0	0.0	12.72	20	1.541×10^{-8}	Disfavored
	4	0	50	67.4	32.6	0.48	20.02	21	1.611×10^{-9}	
		1	50	75.6	24.4	0.32	15.54	22	3.172×10^{-9}	
		2	50	85.8	14.2	0.17	12.58	23	7.595×10^{-9}	
		3	50	98.3	1.7	0.02	11.04	24	2.183×10^{-8}	Disfavored
2.6	2	0	60	100.0	0.0	0.0	27.89	25	1.553×10^{-9}	Disfavored
		1	60	100.0	0.0	0.0	36.20	26	2.456×10^{-9}	Disfavored
		2	70	100.0	0.0	0.0	52.56	27	4.509×10^{-9}	Disfavored
		3	90	100.0	0.0	0.0	79.96	28	8.980×10^{-9}	Disfavored
	3	0	60	100.0	0.0	0.0	29.02	29	1.686×10^{-9}	Disfavored
		1	60	100.0	0.0	0.0	38.72	30	2.920×10^{-9}	Disfavored
		2	70	100.0	0.0	0.0	56.45	31	6.140×10^{-9}	Disfavored
		3	90	100.0	0.0	0.0	85.32	32	1.464×10^{-9}	Disfavored
	4	0	60	100.0	0.0	0.0	24.89	33	1.716×10^{-9}	Disfavored
		1	60	100.0	0.0	0.0	32.60	34	3.168×10^{-9}	Disfavored
		2	70	100.0	0.0	0.0	48.70	35	7.378×10^{-9}	Disfavored
		3	90	100.0	0.0	0.0	75.93	36	2.062×10^{-9}	Disfavored

both peaks become comparable, as can be seen for $\alpha = 2.6$.

- The abundance fraction of H and He plays a major role in the maximum flux values. The exact position of the peak is governed by the redshift evolution of sources, rigidity cutoff $R_{\rm cut}$, and also the maximum source distance $z_{\rm max}$.

- Higher values of $z_{\rm max}$ allows for higher UHECR propagation distance, thus increasing the interaction probability. This results in higher neutrino flux for higher source distances, although the UHECR spectrum is particularly insensitive to variation of $z_{\rm max}$ beyond a value of 2.

We also show the sensitivities of cosmogenic neutrino detection for current and upcoming detectors in the right panels of Fig. 2.1–2.3. Currently operating neutrino detectors have not detected cosmogenic neutrinos yet [95, 155]. We show the detection sensitivity curves for Auger [173, 174] and the flux upper limits from IceCube [97, 162, 175]. Nine years of data measured by IceCube puts a 90% C.L. all-flavor differential flux upper limit on the maximum possible cosmogenic neutrino flux [162]. The peak value of neutrino flux for $\alpha = 2.2$ in our model (case 12) is comparable with the IceCube upper limit. Thus, a detection should be possible in near future with further increase in exposure time. For our $\alpha = 2.6$ cases shown in Fig. 2.3, corresponding to a pure proton composition, the peak neutrino flux is much lower than the IceCube upper limit. PAO can detect the electromagnetic counterparts of the inclined air showers produced by downward-going neutrinos of energy $E_\nu > 0.1$ EeV. The single flavor sensitivity of PAO is multiplied by a factor of three to obtain the all-flavor flux upper limit, assuming an equal flavor ratio. The maximum neutrino flux obtained in our model is much lower than the differential upper limit of $E^2\Phi_\nu \approx 4 \cdot 10^{-8}$ GeV cm^{-2}s^{-1}sr^{-1} imposed by PAO at 0.6 EeV.

The extrapolated 3-yr sensitivities of future detectors like ARA [158], ARIANNA [159], GRAND [161, 176, 177], and POEMMA [160, 178], obtained from simulations of antenna response are shown in the figures. ARA and ARIANNA will detect the Cherenkov radiation resulting from Askaryan effect in the Antarctic ice to identify neutrino events beyond 1 EeV. They shall detect the high neutrino flux cases for $\alpha = 2.2$ and 2.6. Presently under construction in the Mediterranean sea, KM3NeT will employ several cubic kilometres of sea water to detect these highest energy neutrinos [157, 179, 180]. The proposed IceCube-Gen2 is expected to detect cosmogenic neutrinos in the near future. GRAND and POEMMA presents the most ambitious sensitivities and must detect neutrinos for all the cases studied here, testing the viability of our light nuclei composition model.

GRAND proposes to extend the all-flavor integral sensitivity down to $\sim 1.5{\times}10^{-10}$ GeV cm^{-2}s^{-1}sr^{-1} above 0.5 EeV with a sub-degree angular resolution. 3 years of observation by GRAND can detect nearly ~100 neutrinos for a cosmogenic neutrino flux of 10^{-8} GeV cm^{-2}s^{-1}sr^{-1}. The maximum neutrino flux amongst the cases listed in Table 2.2 is 2.08×10^{-8} GeV cm^{-2}s^{-1}sr^{-1}, which occurs for case 12, i.e., $\alpha = 2.2$, $z_{\rm max} = 4$, $m = 3$.

GRAND will apparently detect neutrinos for this case or constrain the UHECR model parameters, within a few years of operation. For our pessimistic scenario, a neutrino flux of $E^2\Phi_\nu \approx 2.35 \times 10^{-9}$ GeV cm^{-2}s^{-1}sr^{-1} is expected from $\alpha = 2.2$, $z_{\rm max} = 2$, $m = 1$. In this case, GRAND will detect roughly ~ 20 neutrinos in 3 years, nearly one-tenth of the event rate compared to the most optimistic scenario.

2.4.2 Constraints from cosmogenic photons

UHECR protons can undergo $p\gamma$ interactions with CMB and EBL to produce neutral pions (π^0), electrons/positrons ($e^\pm$). The neutral pions decay to produce γ-rays ($\pi^0 \rightarrow \gamma\gamma$). The EM particles ($e^\pm$, γ) can initiate electromagnetic cascades that extends down to $\sim$ 1 GeV energies [78, 80, 181]. The main energy loss process for He and heavier nuclei is photodisintegration, whereby contribution to photon fluxes is low [182–184]. The measurement of the isotropic diffuse γ-ray background (IGRB) by *Fermi*-LAT puts an upper limit on the maximum possible cosmogenic photon fluxes [103]. For our $\alpha = 2.6$ injection spectrum, the best-fit indicates $K_{\rm H} = 100\%$ and $m = 0$. We plot the cosmogenic photon spectrum in Fig. 2.4, obtained for various $z_{\rm max}$ values with $\alpha = 2.6$, $m = 0$. We show the measured IGRB spectrum for one of the Galactic foreground models. The simulated photon fluxes obtained for these cases saturate the observed IGRB flux at the highest-energy bin corresponding to a mean energy of 820 GeV. This conforms with the results obtained in earlier studies that show only $m = 0$ is allowed by *Fermi*-LAT data for $\alpha = 2.6$ [78]. Also, the photon fluxes for $z_{\rm max} = 2$, 3, and 4 coincide with each other for $m = 0$ in our study. Similar conclusions were drawn in [153], for $m = 0$ and 3.

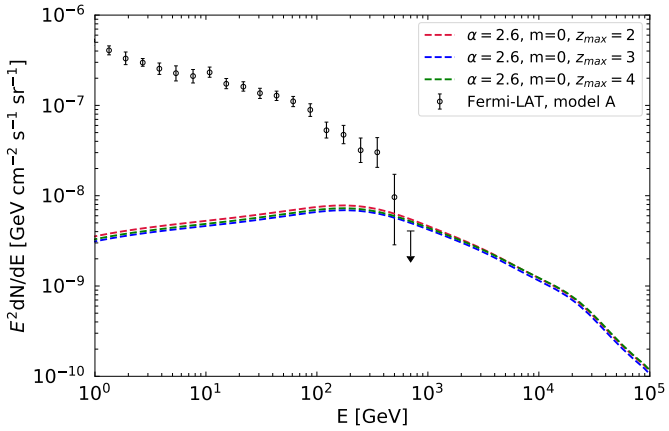

Figure 2.4: Cosmogenic photon fluxes for the $m = 0$ best-fit cases, with $\alpha = 2.6$ and $z_{\rm max} = 2$, 3, and 4. The measured diffuse gamma-ray background by Fermi-LAT is shown.

For $\alpha = 2.4$ injection spectrum, the maximum photon flux within the *Fermi*-LAT upper limit is obtained for $z_{\rm max} = 3$, $m = 3$, and a pure proton composition (see Table 1 of [78]). However, we allow a maximum value of $m = 2$ to add a substantial He contribution, as discussed in Subsec. 2.5.2. He produces lesser cosmogenic photon flux than proton, keeping all other parameters fixed. Hence, the photon flux generated by our $\alpha = 2.4$ cases

must be lower than the measured IGRB flux. Thus, cases allowed by neutrino flux upper limit are also allowed by the IGRB constraints. For all $\alpha = 2.2$ cases, the He abundance is more than 50%. This effectively reduces the production of cosmogenic photons. Thus the flux is expected to be even lower than the aforementioned cases. However, for $z_{\rm max} = 4$, $m = 3$, the neutrino flux touches the IceCube upper limit. Hence, the photon flux for this case too may saturate the IGRB flux and is thus disfavored.

2.5 A New Technique of Composition Analysis

Neutrinos can change their lepton flavor while propagating over astrophysical distance, via the phenomenon of "neutrino oscillation". The probability of such flavor conversion from ν_α to ν_β is given by $P_{\alpha\beta} = \sum_{j=1}^{3} \left|U_{\beta j}\right|^2 \cdot \left|U_{\alpha j}\right|^2$, where $\alpha, \beta = e, \mu, \tau$ and U is the Pontecorvo-Maki-Nakagawa-Sakata (PMNS) mixing matrix between the neutrino flavor and mass eigenstates. For our calculations, we use the current best-fit values of the mixing angles (for the normal mass hierarchy): $\sin^2\theta_{12} = 0.297$, $\sin^2\theta_{23} = 0.425$, $\sin^2\theta_{13} = 0.0215$ and the CP-violating phase $\delta = 1.38\pi$ [185]. The corresponding probability matrix is written as,

$$\begin{pmatrix} P_{ee} & P_{e\mu} & P_{e\tau} \\ P_{\mu e} & P_{\mu\mu} & P_{\mu\tau} \\ P_{\tau e} & P_{\tau\mu} & P_{\tau\tau} \end{pmatrix} \approx \begin{pmatrix} 0.56 & 0.24 & 0.20 \\ \ldots & 0.38 & 0.38 \\ \ldots & \ldots & 0.42 \end{pmatrix} \tag{2.4}$$

which is the same for neutrinos and antineutrinos with $P_{\alpha\beta} = P_{\beta\alpha}$. If we set $\delta = 0$, then a $\sim 10\%$ change in the probabilities is obtained, viz., $P_{e\mu} \approx 0.28$, $P_{e\tau} \approx 0.17$, $P_{\mu\mu} \approx 0.35$ and $P_{\tau\tau} \approx 0.46$. However, the probabilities P_{ee} and $P_{\mu\tau}$ remain unchanged. The value of the CP-violating phase δ can be probed with a precise knowledge of the mixing angles and cosmogenic neutrino fluxes.

2.5.1 Neutrino flavor components

The neutrino fluxes of different flavors on the Earth after oscillation is given by,

$$\Phi_{\nu_\alpha+\bar{\nu}_\alpha} = P_{e\alpha}(\Phi^0_{\nu_e} + \Phi^0_{\bar{\nu}_e}) + P_{\mu\alpha}(\Phi^0_{\nu_\mu} + \Phi^0_{\bar{\nu}_\mu}) + P_{\tau\alpha}(\Phi^0_{\nu_\tau} + \Phi^0_{\bar{\nu}_\tau}) \tag{2.5}$$

where Φ^0_α are the fluxes at production. The neutrino events observed by IceCube are detected from the deep-inelastic neutrino-nucleon scattering. The main signatures to distinguish neutrino events in IceCube are "track-like" events arising from muons produced in charged-current (CC) interactions of ν_μ and "shower-like" events generated in neutral-current (NC) interactions of all neutrino flavors, as well as CC interactions for $\nu_{\rm e}$ and ν_τ. In addition to these, high energy ν_τ can produce the "double-bang" and other event signatures [162, 186–188].

The ratios of cosmogenic fluxes of different flavors can be written as

$$r_{\alpha/\beta} = \frac{\Phi_{\nu_\alpha+\bar{\nu}_\alpha}}{\Phi_{\nu_\beta+\bar{\nu}_\beta}} \tag{2.6}$$

For typical 1 : 2 : 0 initial flavor ratios, the expected ratio on the Earth is just ratio of the probabilities given as

$$r_{\alpha/\beta} = \frac{P_{e\alpha} + 2P_{\mu\alpha}}{P_{e\beta} + 2P_{\mu\beta}} \tag{2.7}$$

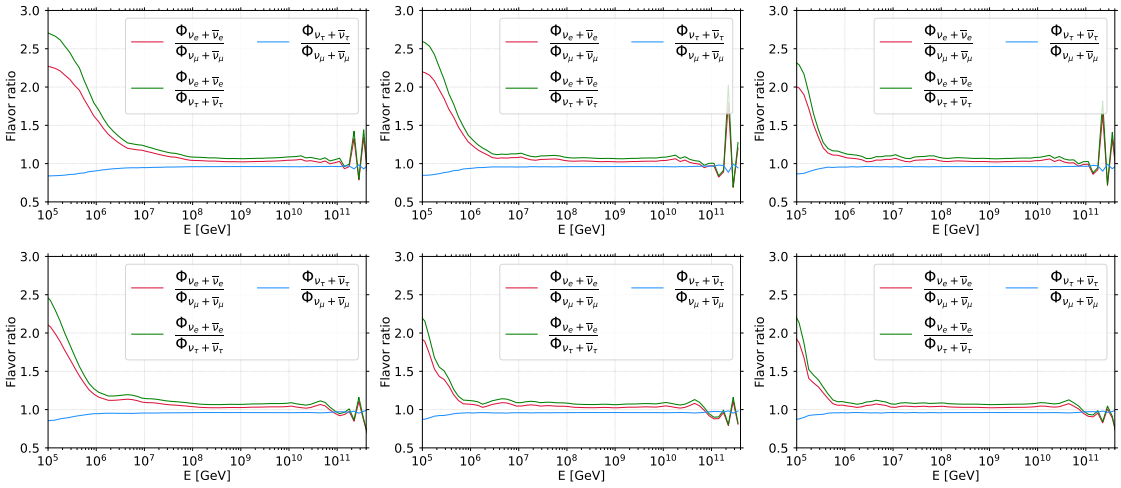

Figure 2.5: Ratio of the neutrino flux of different flavors for the best-fit cases. The left panels, middle panels and right panels are for $\alpha = 2.2$, 2.4 and 2.6 respectively. The top and bottom figures correspond to the case with lowest neutrino flux and maximum neutrino flux respectively for each α, i.e., for the cases plotted in Figs. 2.1–2.3

We plot the ratios $r_{e/\mu}$, $r_{\tau/\mu}$ and $r_{e/\tau}$ obtained at Earth for our H+He composition models in Fig. 2.5. The left to right panels show the ratios for $\alpha = 2.2$, 2.4 and 2.6, respectively. The plots in the top and bottom rows correspond to the same cases as shown accordingly in top and bottom plots of Figs. 2.1–2.3. At the highest energy end, the ratios are not well defined due to lesser number of neutrino events. Below $\approx 10^{20}$ eV, the ratios are roughly constant for a number of decades in energy depending on the different source parameters. These constant ratio parts are roughly consistent with the expected values of $r_{e/\mu} = 1.03$ (red lines), $r_{\tau/\mu} = 0.96$ (blue lines) and $r_{e/\tau} = 1.08$ (green lines); from typical pion-decay flavor ratios 1 : 2 : 0 at production. A shift from these values at low energies is due to neutron beta decays and is an indicator of He/p ratio of the UHECR flux at injection. The $\alpha = 2.2$ cases require larger He/H ratio, hence the deviation from constant flavor ratios happen at energies $\lesssim 10^{17}$ eV, while for the pure-proton injection cases ($\alpha = 2.6$), the flavor ratios are constant down to 10^{15} eV.

2.5.2 Correlation of fit parameters

We find the qualitative correlation between the UHECR parameters varied in our analysis to fit the observed spectrum. To do this, we vary the parameters $R_{\rm cut}$, m, and $K_{\rm H}$ simultaneously over an extended range of values with minute intervals. Since, such variation of parameters is computationally costly, we adopt 3 sets of fixed values for $\{\alpha, z_{\rm max}\}$. Such an analysis must be guided by some physical trends already observed to

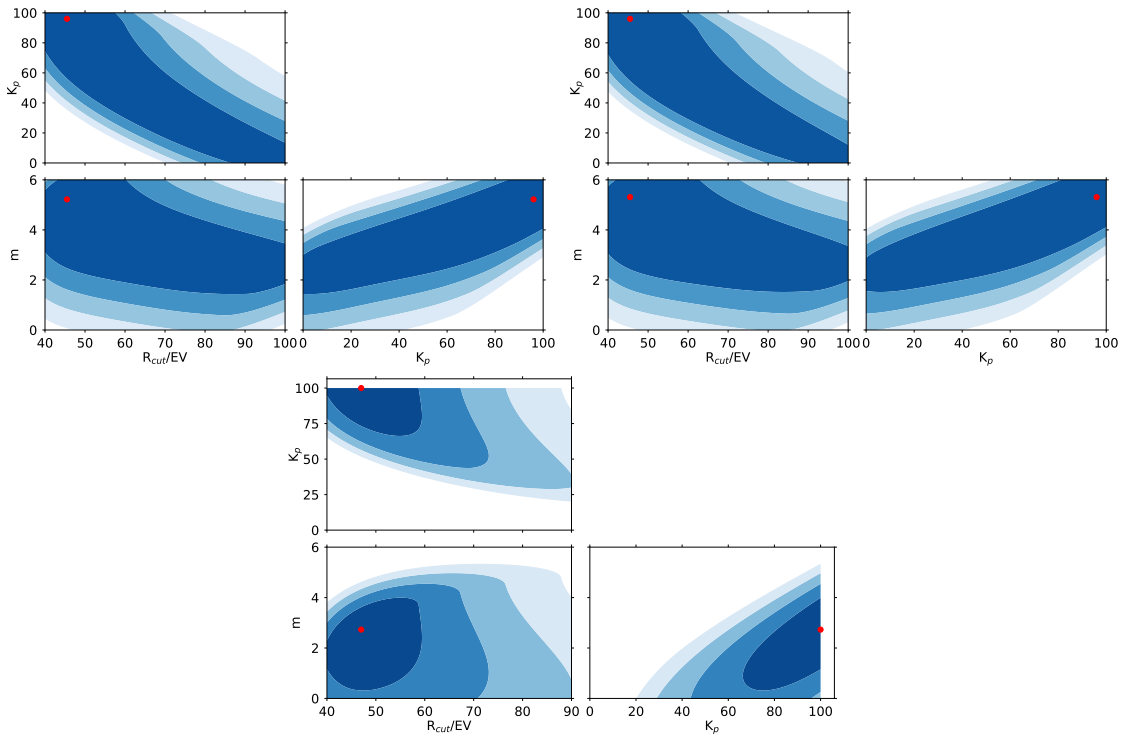

Figure 2.6: Correlation of fit parameters and best-fit values (indicated by a red dot). *Top left*: $\alpha = 2.2$, $z_{\max} = 3$. *top right*: $\alpha = 2.2$, $z_{\max} = 4$. *Bottom*: $\alpha = 2.4$, $z_{\max} = 3$. The 4 shaded regions from dark to light blue are the intervals for 1σ, 2σ, 3σ and 4σ standard deviations.

locate the most sensitive regions of study. Now, Table 2.2 indicates that for all values of α, the best-fit χ^2 value changes very little with the change in $z_{\max}$. This indicates that contribution from sources beyond $z_{\max} = 2$ is insignificant. However, increasing m for any value of $\{\alpha, z_{\max}\}$ noticeably improves the fit, except for $\alpha = 2.6$. For the latter case, the $m = 0$ fits are found to be better than others. Also, noticeable is the change in He requirement as we go to steeper injection spectrum. The value of $K_{\rm He}/K_{\rm H}$ decreases with increasing α, until a pure-proton dominance is seen for $\alpha = 2.6$. All this leads us to consider m, $K_{\rm H}$, and $R_{\rm cut}$ as important parameters in the fitting. The latter also changes between different α values and also between different source distances $z_{\max}$.

Table 2.3: Best-fit values in parameter space [p+He] and in the energy range $E > 10^{18}$ eV

α	$z_{\max}$	m	$R_{\rm cut}$	$K_{\rm p}$	$K_{\rm He}$	χ^2
2.2	3	5.22	45.5 EV	96%	4%	8.29
2.2	4	5.31	45.5 EV	96%	4%	7.04
2.4	3	2.73	47.0 EV	100%	0%	12.01

We vary $R_{\rm cut}$ in the range $40 - 100$ EV with a grid spacing of 10 EV; m is varied in the range $0 - 6$ at intervals of 0.03. The proton fraction $K_{\rm H}$ is varied from 0%s to 100% at step size of 1%. Thus we scan a three-dimensional parameter space with $121 \times 201 \times 101$ grid

points. The scan is repeated for three sets of values of $\{\alpha, z_{\max}\}$, viz., $\alpha = 2.2$, $z_{\max} = 3$; $\alpha = 2.2$, $z_{\max} = 4$; and $\alpha = 2.4$, $z_{\max} = 3$. A corner plot indicating the relative dependence of the parameter variation for these three sets are shown respectively in the top left, top right and bottom panel of Fig. 2.6. The colored regions indicate the Bayesian confidence intervals for 1σ, 2σ, 3σ, and 4σ standard deviations, and 17 d.o.f. The darkest region corresponds to 1σ region, containing the best-fit case indicated by a red dot, and the shaded regions are progressively light-colored for higher σ values. The best-fit parameter values are shown in Table 2.3. We see that for $\alpha = 2.2$, the best-fit corresponds to a very strong source evolution and 96% proton composition. Such huge proton fraction at the highest energies and high value of evolution index leads to copious production of pion decay neutrinos by UHECRs at the highest energies. Fig. 2.7 shows the spectrum fit and the cosmogenic neutrino spectrum for $\alpha = 2.2$ and $z_{\max} = 3$. Although, the UHECR spectrum fit is extremely good, the neutrino flux violates the IceCube upper limit [162]. Also, the composition corresponds to that of a pure-proton, a direct contradiction of Auger predictions on UHECR composition. This resonates with the fact already studied in [189, 190] with an older version of Auger data, that pure proton composition cannot explain the UHECR spectrum as it overproduces the neutrino and γ-ray flux. The fit to Auger data for UHECR spectrum turns out to be extremely good (shown in the left panel of Fig. 2.7), but the composition is very near to pure proton up to the highest observed energies. The standard deviation in the shower depth distribution, $\sigma(X_{\max})$ indicates a composition that lies between p and He up to $10^{19.5}$ eV. Thus, we reject the best-fit parameter sets obtained for $\alpha = 2.2$.

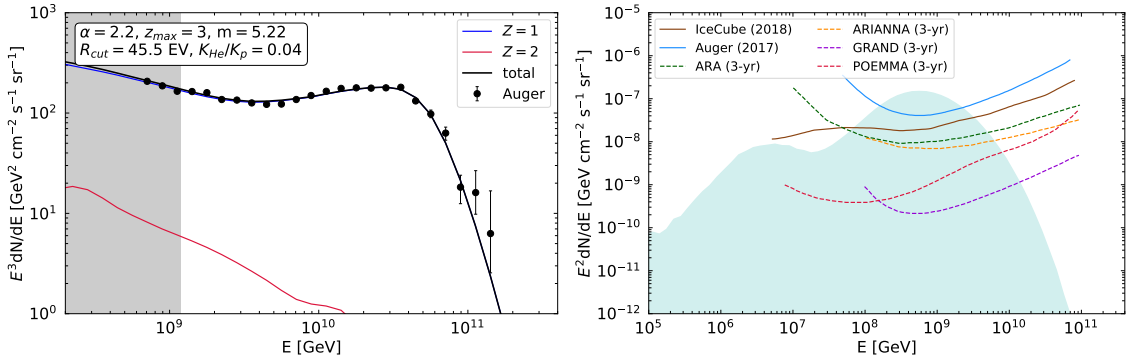

Figure 2.7: UHECR spectrum (*left*) and cosmogenic neutrino flux (*right*) for the best-fit case corresponding to $\alpha = 2.2$ and $z_{\max} = 3$, found by scanning over a wide range of parameter space

Hence, we restrict ourselves to $m \leqslant 3$ to increase $K_{\rm He}$ and thus reduce the neutrino flux at the high-energy peak. A comparison of the top left and top right panel of Fig. 2.6 indicates that the change in best-fit parameter values is infinitesimal due to an increase in $z_{\max}$, within the precesion of our study. We see in the bottom panel of Fig. 2.6, for $\alpha = 2.4$, the best-fit corresponds to 100% proton composition and a source evolution index $m = 2.73$. To avoid a pure-proton composition and prevent the neutrino flux from

exceeding the IceCube upper limit, we restrict ourselves to $m \leqslant 2$. The latter leads to a significant He contribution near the ankle. For $\alpha = 2.6$ cases, all values of $m \geqslant 0$ gives a pure proton composition and the fit progressively worsens for higher m. Since, we restrict ourselves to positive values of the source evolution index in the H+He model, the value of m cannot be constrained any further to include He abundance at injection. We have checked that no best-fit could be found for $\alpha = 2.6$, within 1σ confidence level for the range of parameter values considered here. Hence, $\alpha = 2.6$ or steeper injection cases can be discarded as a plausible UHECR scenario. An interesting point to note is that the 1σ contours shown in Fig. 2.6 for $\alpha = 2.2$ and 2.4 encompasses all the best-fit cases listed in Table 2.2 for the corresponding values of $\{\alpha, z_{\rm max}\}$.

2.6 Heavy Nuclei Composition

In the analysis done by PAO, the differences between the various propagation models with different physical assumptions are much larger than the statistical errors on the parameters. We explore another scenario of UHECR composition within the "CTD" propagation model, in which the sources inject a mixed composition of representative elements ^{1}H, ^{4}He, ^{14}N, and ^{28}Si. We consider the ^{56}Fe fraction to be zero as found for all the UHECR propagation models considered by PAO. Photodisintegration of heavier nuclei leads to the production of protons, contributing at each energy bin. This leads to the mass dispersion in observed composition. Only those nuclei which are injected by sources within $\sim$ 100 Mpc may be detected with a small mass dispersion. Unlike light composition, it is difficult to produce the sharp ankle feature using a heavier composition and a rigidity dependent cutoff at injection. Hence, in this case, we start our fit to the UHECR spectrum from $5{\cdot}10^{18}$ eV. This demands for heavy nuclei to dominate at the highest energies, resulting in the requirement of an additional source population to explain the sub-ankle spectrum. The best-fit values of the parameters, found by PAO, in the "CTD" propagation model for a flat source evolution ($m = 0$) are $\alpha = -1.5$, $\log_{10}(R_{\rm cut}/V) = 18.15$, and $K_{\rm H} : K_{\rm He} : K_{\rm N} : K_{\rm Si} = 45 : 52 : 3 : 0.06$. The uncertainties in the best-fit values of α extends down to $\alpha = -1.5$, the lowest value considered in their study.

2.6.1 UHECR energy spectrum

Here, we extend the analysis to $\alpha < -1.5$ in the range $[-2.5, 0]$ considering a source evolution of the form $(1+z)^m$. The parameter $\log_{10}(R_{\rm cut}/V)$ is varied between the interval [17.8, 18.3]. We scan the parameter space with grid spacing of 0.1 in α and 0.1 in $\log_{10}(R_{\rm cut}/V)$. Again, we consider that sources inject particles with energy between $0.1 - 1000$ EeV, i.e., the heavier nuclei have $E_{\rm max} = Z{*}1000$ EeV, following the injection spectrum of Eqn. 2.1. For heavier elements to dominate at the highest energies, they must originate from sources at $z \lesssim 0.5$ to contribute in the super-ankle region. Hence, we consider a maximum redshift $z_{\rm max} = 1$ in our study. It is shown in other studies that source evolution becomes insignificant beyond this value [153]. To cover the highest

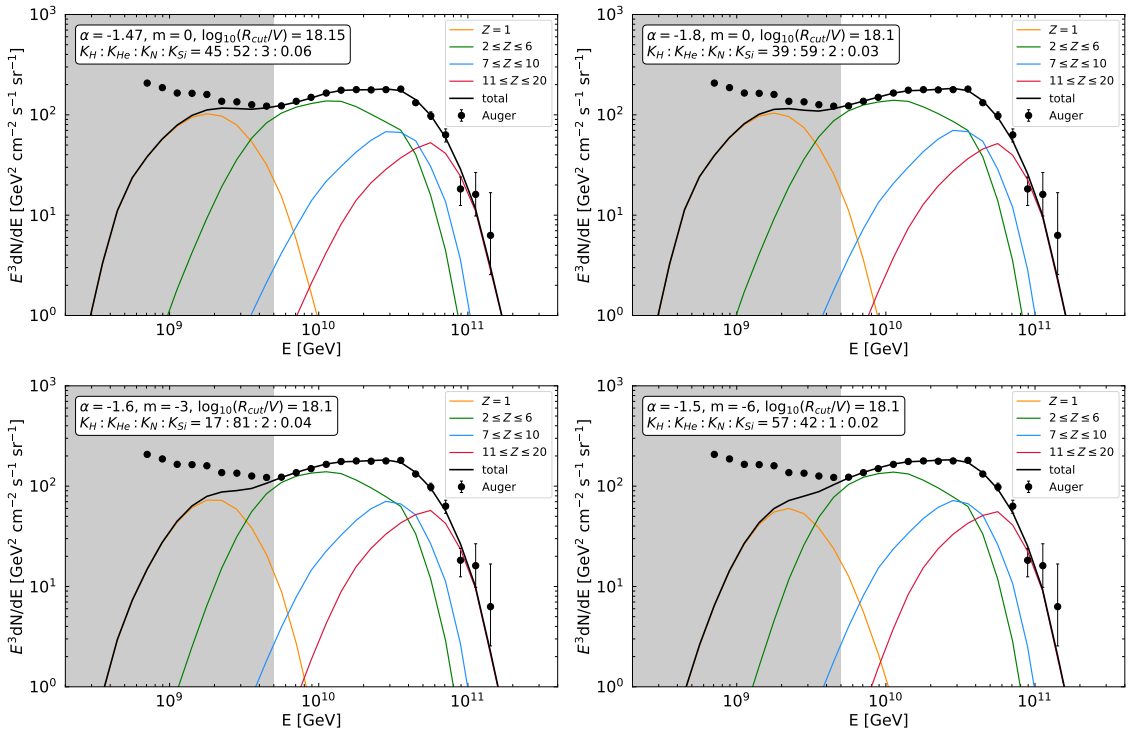

Figure 2.8: UHECR spectra for the best-fit parameters of CTD model as found by PAO for $m = 0$ (top left), and that calculated in this work for $m = 0, -3, -6$ by extending the range of α used to scan the parameter space. The top right, bottom left and bottom right spectrum corresponds to $m = 0$, $m = -3$ and $m = -6$ respectively as indicated in the figure labels.

energy data points, one has to consider $z_{\rm min} = 0$, or increase the $R_{\rm cut}$ value in the case of heavier nuclei composition. To increase the value of α in order to achieve a steeper injection spectrum conforming with most acceleration models, we find negative values of m are preferred over others. We do our analysis for three discrete values of m, viz., 0, −3, and −6. We also present the best-fit spectrum obtained with the paramter values found by PAO in the top left panel of Fig. 2.8. The spectrum differs only slightly from the best-fit found here, mainly because of different paramter ranges and grid spacings considered.

Table 2.4: Best-fit values in parameter space for a mixed composition at injection [H+He+N+Si]. The fit is performed in the energy range $E > 10^{18.7}$ eV.

m	α	$\log_{10}(R_{\rm cut}/{\rm V})$	K_H	$K_{\rm He}$	$K_{\rm N}$	$K_{\rm Si}$	$\chi^2_{\rm spec}$
0	−1.8	18.1	39	59	2	0.03	2.59
−3	−1.6	18.1	17	81	2	0.04	2.57
−6	−1.5	18.1	57	41	1	0.02	2.66

The best-fit values of the cases studied here are listed in Table 2.4. The corresponding spectra for $m = 0, -3$, and -6 are shown in Fig. 2.8. The cosmogenic neutrino flux for these cases and the ratio of fluxes of individual neutrino flavors are shown in the left and right

panel of Fig. 2.9. Since, the propagation length of the majority of UHECRs decreases with decreasing values of m, a reduced rate of $p\gamma$ interactions leads to a reduced neutrino flux. This can be seen in he left panel of Fig. 2.9, where peak value of the flux decreases with more and more negative values of m. The $m = 0$ case yields the maximum cosmogenic neutrino flux corresponding to 9.6×10^{-11} GeV cm^{-2}s^{-1}sr^{-1} at 60 PeV. However, the neutrino fluxes are too low to be detected by currently operating or upcoming neutrino detectors. Even the $m = 0$ case is beyond the reach of extrapolated 3-yr GRAND sensitivity. The ratio of individual flavors are presented in the right panel of Fig. 2.9, where the flavor ratios are denoted as $r_{e/\mu} = r_1$, $r_{e/\tau} = r_2$ and $r_{\tau/\mu} = r_3$. Although, a difference in the flavor ratios is missing for various m values, a general trend of significant increase in ν_e flux is observed. This can be attributed to the fact, more heavier nuclei results in higher flux of β-decay neutrinos.

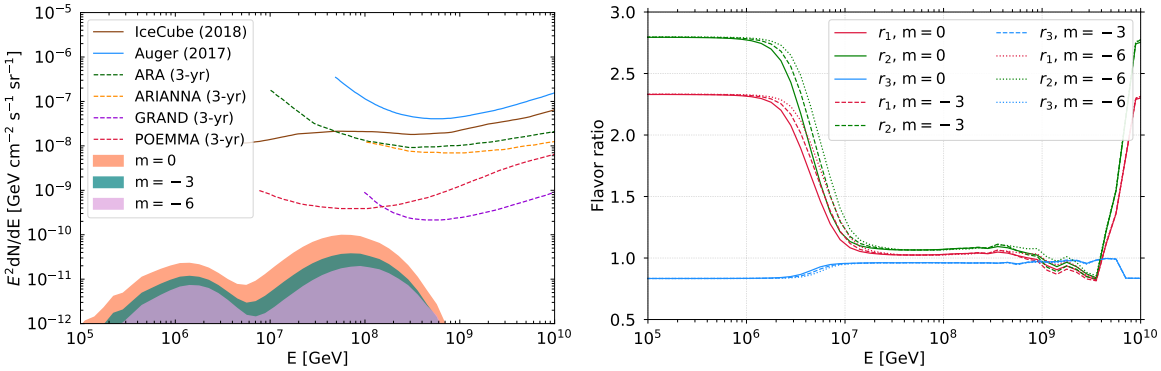

Figure 2.9: *Left*: Cosmogenic neutrino fluxes for the best-fit parameters of CTD model, as listed in Table 2.4. *Right*: The ratio of neutrino flavor components for the evolution cases studied.

2.6.2 Difficulties in heavy nuclei model

However the fit to UHECR spectrum using heavy nuclei injection at the sources poses some physical problems, difficult to comprehend. These are listed below:

- For heavier nuclei to dominate at the highest observed energies, the injection spectral index becomes too hard ($\alpha < 0$) to be explained by conventional acceleration mechanisms, such as the Fermi acceleration model.

- A strong negative redshift evolution ($m < 0$) implies more sources to be present in the local neighbourhood of our Galaxy. However, the observed distribution of γAGNs or other ultra-luminous sources does not confirm with this prediction.

- A lower value of $R_{\rm cut}$ ($\approx 10^{18.1}$ V) necessarily implies increased interaction of UHECRs on EBL than on CMB. But, the photodisintegration cross-section of medium nuclei elements (CNO) on EBL is not well-constrained [3].

- The ankle feature is difficult to be generated by a hard injection spectrum and heavier

nuclei at injection. Hence, an additional source population of unknown nature is required to fit the spectrum below the ankle.

Several propositions have been made to explain the hard spectral indices required in case of a mixed composition at injection. The spectrum of accelerated particles can be different from the spectrum of escaping particles because of increased interaction near the sources with ambient matter and radiation [153]. Thus the injection spectrum, attributed to the latter spectrum, becomes hardened. Other scenarios that invoke magnetic reconnection are also theoretically possible. The infrared peak of the EBL models affects the propagation of heavy nuclei strongly. A lower rigidity cutoff, in addition to a hard spectral index, is preferred in this case to avoid overproduction of secondary protons [151]. The lower value of $R_{\rm cut}$ decreases the maximum energy of secondary protons and thus allows heavier elements to dominate at higher energies, requiring negative values of α. The uncertainties in the EBL model, various air shower models, and cross section for photodisintegration of medium nuclei on EBL translates into a considerable uncertainty in determining the mass composition [3, 191, 192]. Low-luminosity BL Lacertae (BL Lac) objects are suggested as candidates of UHECR accelerator, possessing negative redshift evolution and are more numerous at low redshifts [193]. Increasingly negative values of m leads to a steeper injection spectra, thus conforming with Fermi acceleration model. However, the number density of high-luminosity BL Lac objects peaks at a redshift of $z \simeq 1.2$, which is beyond the redshift range considered.

2.7 Implications & Discussions

⊙ We have explored plausible astrophysical scenarios of injected mass composition to fit the observed UHECR spectrum. We consider two cases, viz., one with only light elements H+He at injection and another with a mixed composition of representative elements H+He+N+Si. For the former, a fit to the spectrum is achievable starting from $E \approx 10^{18}$ eV, whereas for the latter, a fit is possible only for $E > 5 \cdot 10^{18}$ eV, i.e., beyond the ankle. We adopt the "CTD" propagation model, using CRPROPA 3 propagation, TALYS 1.8 photodisintegration cross-section, and Domínguez et al. EBL model; for a source evolution in redshift of the form $(1+z)^m$ [189]. Striking differences are observed between the two cases, particularly in the best-fit values of the source evolution index m. While a light nuclei composition is compatible with the most prevalent positive source evolution index, heavier nuclei at injection prefer a negative source evolution. The injection spectrum is too hard for the heavy nuclei cases, with the highest energies dominated by N and Si. The rigidity cutoff required in the latter case is more than an order of magnitude lower than that required for light nuclei composition.

⊙ The H+He mass composition has also been studied earlier in Ref. [194] using an older set of Auger data [195], and no cosmological evolution of the sources. Various studies have also derived a lower limit of proton-to-helium ratio based on shower depth

distribution and considering various hadronic interaction models [196]. We find that good fits to the UHECR spectrum are obtained for the range of α values considered in our study. We limit the plausible injection spectrum for this case within $2.2 \leq \alpha \leq 2.6$. For lower values of α, it becomes difficult to explain the spectrum from $E \approx 10^{18}$ eV with only light elements at injection. For $\alpha = 2.6$, reasonable fits are obtained for only $m = 0$ cases. However, all $\alpha = 2.6$ cases are disfavored because of their pure proton composition. This conforms with earlier studies that show a pure proton dip model supersedes the IceCube upper limit due to the over-production of neutrinos. Similar constraints have been put from studies of cosmogenic γ-ray fluxes.

⊙ In Ref. [197], it is shown that the pure proton dip model exceeds the neutrino flux upper limit by IceCube for various combinations of α, m and $E_{\rm max}$. A similar inference is given from studies of maximum possible cosmogenic photon fluxes in a pure proton scenario [78, 80, 190]. A study of luminosity and number density of steady sources show that UHECRs cannot be pure protons at $E > 8 \times 10^{19}$ eV [154]. For $\alpha < 2.6$, the addition of other nuclei to composition becomes indispensable. These results indicate a pure proton composition is impossible to comprehend at energies $E > 8 \cdot 10^{19}$ eV.

⊙ The reference model "SPG" in the analysis by PAO [151] considers *Simprop* propagation [4] with the PSB model of photodisintegration [70] and Gilmore et al. EBL model [170]. There are two minima found in the measure of goodness-of-fit, corresponding to two best-fit cases [151]. One of them corresponds to $\log_{10}(R_{\rm cut}/V) = 18.5$ and $\alpha \approx 1$. The other minima corresponds to $\log_{10}(R_{\rm cut}/V) = 19.55$ and $\alpha \approx 2.04$. Correspondingly, the former case prefers a heavy nuclei composition dominating at the highest energies, whereas the light component extends up to the highest-energy bin for the latter. Since uncertainties in the EBL model, photodisintegration cross-section, and hadronic interaction models translate to uncertainties in the mass composition of the observed spectrum [3], it is reasonable to consider both the cases as a plausible scenario. This provides us an impetus and motivation for the analyses done here. We have considered the alternate scenario of mixed composition at injection within the "CTD" propagation model and calculated the best-fit values of their abundance fraction (K_i), cutoff rigidity ($R_{\rm cut}$), and the spectral index (α). As expected, the fits obtained corresponding to low values of $R_{\rm cut}$ and a hard injection spectrum.

⊙ In the case of light nuclei injection model, the proton spectrum contributes to the cutoff region. Also, the high value of $R_{\rm cut}$, in this case, suggests that the cutoff occurs as a result of photopion production of UHECR protons on CMB, through the Δ-resonance channel. Thus the cutoff here is a natural limit occurring due to the impenetrable nature of UHECRs through the cosmic background photons. However, in the case of heavy nuclei injection model, the contribution at the highest energies comes from N and Si. The UHECRs must originate in nearer sources ($z \lesssim 0.5$) to survive photodisintegration and contribute to the region of the spectrum beyond the ankle ($E \gtrsim 5 \times 10^{18}$ eV). This corre-

sponds to low R_{cut} values and thus, the cutoff in the UHECR spectrum must result from the maximum acceleration energy at the sources. Also, the ankle in case of H+He model is due to a combination of e^+e^- pair-production interaction of UHECRs and changing composition between H and He. However, in the case of heavy nuclei model, the sub-ankle spectrum must be explained by another extragalactic source population, owing to the incapability of Galactic SNRs to accelerate cosmic rays beyond a few PeV. The recent proposition of increased photohadronic interactions close to the accelerator may be able to solve this problem [198].

⊙ We have also calculated the cosmogenic neutrino fluxes for both models. Currently operating neutrino detectors are yet to reach the necessary sensitivity to detect cosmogenic neutrinos. However, 9-yrs of data measured by IceCube provides a flux upper limit to the allowed neutrino spectrum [162]. This can constrain the UHECR source models and thus, the range of parameter values. For our light nuclei model, $\alpha = 2.6$, $m = 0$ cases yield a cosmogenic flux of magnitude at least ten times lower than the IceCube upper limit. For lower values of α, some of the cases have peak neutrino flux comparable to the IceCube limit, at ~ 1 EeV. Upcoming detectors like GRAND and POEMMA provides a promising sensitivity, capable of constraining most UHECR source models [160, 161, 176, 178]. They plan to reach a sub-degree angular resolution and detect neutrinos at energies beyond a few PeV up to $\approx 10^{20}$ eV. We also propose a technique by which the ratio of the flux of individual neutrino flavors can act as a discriminator of UHECR composition at injection. This will rely on the event topology of ultrahigh-energy neutrinos if detected in the future [157]. The neutrino flux resulting from the heavy nuclei model is extremely low, and a detection in the near future seems improbable.

2.8 Conclusions

UHECR mass composition depends on various factors such as redshift evolution of sources, maximum energy of primary particles and also on the injection spectrum which is determined by the acceleration mechanism. The much acknowledged choice of power-law injection with source spectral index near $\alpha \approx 2$ originates in the well known Fermi acceleration model. Latest measurements by the Pierre Auger Observatory favors a low spectral index and present a fit to the UHECR spectrum starting from $E \approx 5 \times 10^{18}$ eV. PAO assumes a mixed composition at injection, with the precise element fractions being determined by the specific propagation model, photodisintegration cross-section, and EBL spectrum. In this paper, we have studied a model called "CTD", with CRPROPA 3 propagation, TALYS 1.8 photodisintegration cross-section, Domínguez et al. EBL model, assuming sources inject only H and He nuclei. We constrain the range of injection spectral index and the cut-off rigidity feasible in this light nuclei composition model. We vary the abundance fraction at injection to find the best-fit cases for a wide range of UHECR parameter values. We find, a fit to the entire spectrum is possible starting from E $\approx 10^{18}$ eV

with a single population of extragalactic sources. We have also calculated the cosmogenic neutrino fluxes from all production channels. We plot the spectra of best-fit cases which represent the entire range of neutrino fluxes possible for α =2.2, 2.4, and 2.6. All the best-fit cases yield neutrino spectra consistent with the flux upper limits imposed by the present detectors. This suggests that the abundance fraction of H and He considered in the best-fit cases are plausible. The ratio of fluxes of different flavors obtained on earth after neutrino oscillation are consistent with our expectations. A departure from the constant flavor ratio at lower energy occurs due to neutron beta decay. The χ^2 values obtained in the fitting procedure of UHECR spectrum favors $\alpha = 2.2, 2.4$ over the pure proton $\alpha = 2.6$ cases. We also explore the plausible parameter space for a mixed composition at injection. Source redshift evolution is found to play a significant role in determining the flux as well as the position of peak in the cosmogenic neutrino spectrum. We also note, with the increase in maximum source redshift ($z_{\rm max}$) there is an increase in neutrino flux, due to increased propagation length of primary particles. Future neutrino telescopes with higher sensitivities at $>$ 1 PeV energies, will be able to probe a range of flux models we predict. A measurement will be able to constrain the maximum redshift of the UHECR source distributions. Furthermore, neutrino flavor identification will shed light on the abundance fraction of nuclei in the UHECR spectrum at injection, as shown in neutrino flavor ratios for our flux models. While we show that a H+He composition model is capable of fitting UHECR data, future cosmogenic neutrino data will provide a robust test for this scenario.

3

VHE Gamma-Rays from UHECR Interactions

NASA launched the *Fermi* Gamma-Ray Space Telescope in 2008 and the Large Area Telescope (LAT) on board has been observing the γ-ray sky since then [103]. The current sensitivity of operation lies between 5 MeV – 1 TeV energy range. It has detected several point sources of high-energy emission. In particular, the Active Galactic Nuclei (AGNs) comprises the majority of extragalactic γ-ray sources. However, γ-rays beyond the *Fermi*-LAT upper limit has also been detected by other terrestrial detectors such as HESS [199], MAGIC [200], VERITAS [201], and HAWC [202, 203], etc., experiments. The observation of long-term light-curve from the point sources consolidated in all wavebands gives us the spectrum of radiation spanning the entire electromagnetic range. This multi-wavelength spectrum is of utmost importance to understand the high-energy radiative processes inside black hole jets. The jets are also the power-house of the most energetic particles, the ultrahigh-energy cosmic rays (UHECRs, $E \gtrsim 0.1$ EeV) and other extreme energy particles including γ-rays and neutrinos. The astrophysical environment inside the jets of supermassive black holes (SMBHs) are not known to a high precision.

AGNs are powered by the accretion onto a SMBH, producing a collimated beam of outflow in the direction of angular momentum and/or along the spin axis of the central black hole. Often jets on both sides of the AGN have been observed. The main components are the subparsec-scale rotating accretion disk (AD) surrounding the SMBH, a dust-free gas cloud relatively close to the center (broad-line region, BLR) under the gravitational influence of SMBH, a dusty torus (DT) farther away obscuring the BLR, and a ionized narrow-line region (NLR) extending out from $\sim$ 1 pc to several kpc under the gravitational influence of the host galaxy. In addition, the radio-loud AGNs exhibit a collimated radio synchrotron emission. The jets of relativistic plasma moving outwards have been observed on scales from subparsec to Mpc lengths with occasional presence of diffuse radio-lobes near the termination. For a more detailed description of the AGN structure, please see Ref. [204]. For some radio-loud AGNs, these jets are oriented close to the line-of-sight of the observer and are luminous from radio to GeV/TeV γ-ray range. The AGNs of this subclass are called blazar. There can be two types of blazar, based on their radiative properties and the observed photon spectrum, viz., the BL Lacertae (abbv. BL Lac) objects and the flat spectrum radio quasers (abbv. FSRQs).

3.1 Background

The spectral energy distribution (SED) of blazars display a non-thermal continuum spectrum consisting of two peaks. Analysis of the SED yields important properties of

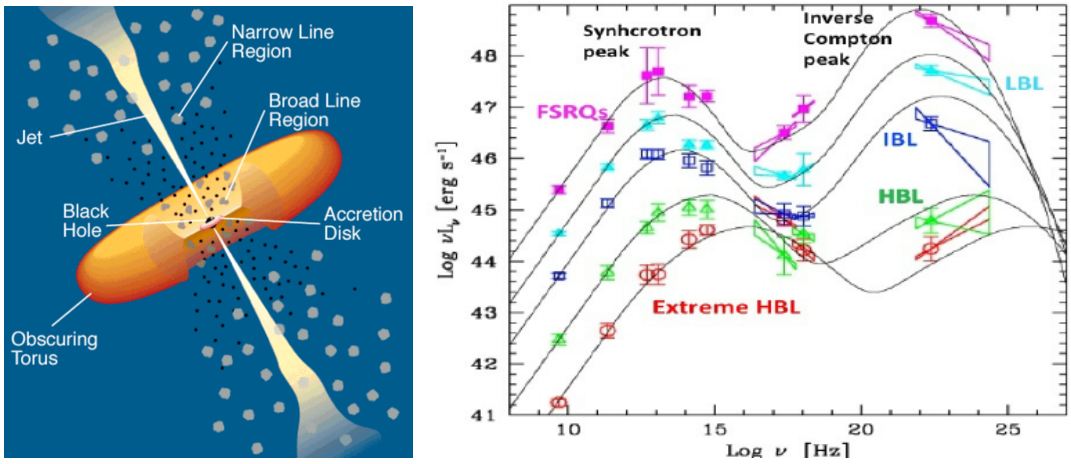

Figure 3.1: *Left:* The AGN physical model illustrating the broad scales of the key regions, viz., the accretion disk, jet, BLR, NLR, and dusty torus. The figure is reproduced from Ref. [204]. *Right:* The relative luminosities and frequencies of peak emission for different class of blazars, known as the blazar sequence. The image is taken from Ref. [205].

the jet and hence, about the blazar. The jet emission also shows variability over diverse timescales at different wavebands and there may also exist a time delay between them [206]. The radiative process inside the jet responsible for this flaring activity is not well understood. The low-energy peak, between optical and X-ray energies, is almost certainly due to the synchrotron radiation of relativistic electrons, accelerated within the jet. The high-energy peak presumably originates from the inverse-Compton (IC) scattering of synchrotron photons (synchrotron self-Compton, SSC), or external photons (AD, BLR, DT). However, the high-energy peak for some BL Lac objects may exhibit an unattenuated hard intrinsic spectrum up to TeV energies. This is difficult to explain using leptonic model alone. The doppler factor is required to be extremely high for the relativistic beaming of very high-energy (VHE; 30 GeV $< E <$ 30 TeV) γ-rays towards the observer. Often to resolve this problem, a lepto-hadronic model is employed whereby the VHE spectrum is explained by photohadronic interactions of cosmic rays inside or outside the jet [6].

The synchrotron loss rate is inversely proportional to the square of the mass of charged particles. The energy loss rate is given as

$$-\left.\frac{dE}{dt}\right|_{\text{synch}} = \frac{e^4 B^2}{6\pi\epsilon_0 c m^2}\Gamma^2\beta^2\sin^2\alpha \tag{3.1}$$

where Γ is the Lorentz factor and βc is the relativistic velocity of the electron. Cosmic-ray hadrons, also accelerated in the jets of relativistic outflow, can undergo a variety of interactions transporting energy and momentum over large distances. Interaction of these hadrons with synchrotron or IC photons produces electron-positron pairs (e^+e^-) or charged and neutral pions (π^0, π^+). The e^+e^- pairs can radiate in the magnetic field of the jet by synchrotron process. The neutral pions decay to produce γ photons ($\pi^0 \rightarrow \gamma\gamma$). The charged pions and muons may undergo synchrotron emission, before decaying to

electrons/positrons. The mass of pions and muons is nearly two order of magnitude higher than electrons. Hence, their contribution via synchrotron emission will be much lower compared to electrons. These γ-rays produced through hadronic channels are also expected to contribute at the high-energy end of blazar SED. Some models have evoked a proton synchrotron scenario in the context of explaining hard TeV spectrum of extreme BL Lac objects [207]. In the latter case, the peak of synchrotron radiation occurs at a few TeV. However, this requires very high doppler factor $\delta \sim 100$ or ultrahigh-energy protons radiating in kilo-Gauss magnetic fields. Often such requirement leads to the violation of Eddington luminosity budget while constraining the total kinetic power in the jet [208].

The SED of high-frequency peaked BL Lac objects (HBLs) reveal their synchrotron peak in the UV-to-X-ray energy range and possess unattenuated γ-ray spectrum up to multi-TeV energies. If such high-energy photons are produced inside the jet emission region, then they must be absorbed due to intrinsic $\gamma\gamma$ collision with target photons originating from BLR, DT, or AD region. Another contributing factor to their attenuation may be due to the $\gamma\gamma_{\rm bg}$ pair production interactions with the extragalactic background light (EBL). Also, a very hard intrinsic TeV spectrum is difficult to be explained by a leptonic model, because of the Klein-Nishina effect. The latter causes a suppression in the IC energy-loss rate of relativistic electrons at high frequencies. For higher values of photon energy in electron rest frame, $\gamma\epsilon >> m_e c^2$, the Compton scattering cross-section depends on incoming photon energy and IC emission becomes less efficient. The differential cross-section for unpolarized radiation is given by the Klein-Nishina formula,

$$\frac{d\sigma}{d\Omega} = \frac{r_0^2}{2}\frac{\epsilon_1^2}{\epsilon^2}\left(\frac{\epsilon}{\epsilon_1} + \frac{\epsilon_1}{\epsilon} - \sin^2\theta\right) \tag{3.2}$$

where, ϵ and ϵ_1 are the energies of incident and scattered photons in the laboratory frame. θ is the scattering angle. At low frequencies $\epsilon_1 \sim \epsilon$, the cross-section reduces to the classical Thomson limit.

In this research, we consider yet another framework of VHE γ-ray production. The UHECRs accelerated in the jets of extreme blazars can escape from the sources and interact with the cosmic background photons to produce electromagnetic (EM) particles ($e^{\pm}$, γ-rays) [209]. These secondary particles can initiate electromagnetic cascade down to GeV energies and produce a resultant γ-ray spectrum peaking at TeV energies [27, 28, 210–215]. Thus, the line of sight interaction of UHECRs leads to a significant contribution in the observed VHE spectrum of HBLs. The HBLs must be placed at distances higher than the mean interaction length of UHECR protons for photohadronic interactions. However, for very distant sources, the majority of cascade photons produced are either scattered off from the line of sight or completely absorbed by the EBL photons. Hence, to increase the efficiency of such a process, the redshift of the blazar is crucial. UHECRs with $E \geqslant 50$ EeV undergoes resonant photopion production with the CMB photons, while interaction with EBL photons dominate at lower energies.

Among the γ-ray sources in the *Fermi*-Lat 8 yr source catalog (4FGL), more than 3130 of the identified or associated sources are blazars [216]. The companion catalog of AGNs, the 4LAC catalog divides the blazars into three types, viz., 650 belonging to the FSRQ class, 1052 BL Lac objects, and 1092 blazars of unknown type [217]. FSRQs have higher luminosity but are mostly low-synchrotron peaked. The BL Lac objects are more or less equally distributed between low-synchrotron peaked, intermediate-synchrotron peaked and high-synchrotron peaked subclasses. The redshift is unknown for the majority of BL Lac objects. For our study, we select a representative sample of a few HBLs with prominent TeV emission and no variability. We model the multiwavelength SED in the quiescent state by a one-zone leptonic synchrotron/SSC model upto the highest energy possible for the jet parameters considered. The VHE spectrum is explained using the cascade photons originating from the line-of-sight UHECR interactions with CMB and EBL. We show, the requirement of this additional component is inevitable for the HBLs considered in our study.

During the propagation of UHECRs, they are deflected from the line of sight by the EGMF. We consider the propagation though a random turbulent EGMF and put constraints on its rms value, such that UHECR protons are collimated close to the line of sight of the observer. The losses due to attenuation in the EBL and deflections in the EGMF increases the total jet power required to explain the observed SED. The possible origin of VHE γ-ray production from hadronic interactions inside the jet has been studied earlier in great details [6, 218–221]. But the efficiency of photohadronic interactions in the high-energy limit is $\sim 10^{-3}$ times of the the peak $\gamma\gamma$ pair production rate [222, 223]. Hence, although high-energy photons can be created inside the jet, their escape is greatly reduced. Cosmogenic neutrinos will be produced in the same UHECR interactions, as producing photons. These neutrinos contribute to the diffuse astrophysical neutrinos. We find an estimate of the neutrino flux produced in our model to compare with the flux upper limit measured by IceCube [162] and Pierre Auger experiments [173]. We infer the prospects of cosmogenic neutrino detection is weak in the near future.

3.2 Theoretical Framework

3.2.1 Leptonic modeling

Particles are accelerated inside the jet to relativistic energies which emits radiation via different physical processes. The emission region can be considered as a spherical blob of radius R, consisting of a relativistic plasma of electrons, protons moving through a magnetic field B. This is the assumption made in a diffusive shock acceleration model. The steady injection spectrum of electrons in the comoving frame of the jet is given by

$$Q_{\rm e}(E_{\rm e}) = A_{\rm e}\left(\frac{E_{\rm e}}{E_0}\right)^{-\alpha} \exp\left(-\frac{E_{\rm e}}{E_{\rm e,cut}}\right) \tag{3.3}$$

where we consider the value of reference energy $E_0 = 0.5$ GeV. We obtain the best-fit values of other parameters, viz., the cutoff energy ($E_{\rm e,cut}$), injection spectral index (α), and the minimum electron energy ($E_{\rm e,min}$) by modeling the synchrotron spectrum. The resulting IC spectrum is obtained with synchrotron spectrum as the seed photons. The SSC spectrum is adjusted such that the γ-ray flux extends up to the highest energies possible. We use the open-source code GAMERA[1] to model the radiative losses incurred in a leptonic model [224]. The one-dimensional transport equation is written as

$$\frac{\partial N_e}{\partial t} = Q_e(E_e, t) - \frac{\partial}{\partial E}(bN_e) - \frac{N_e}{t^e_{\rm esc}} \tag{3.4}$$

Here, $N_e(E_e, t)$ is the spectrum of particles at a time t. The energy loss rate of leptons is given by $b = b(E_e, t)$ and $t^e_{\rm esc}$ is the timescale in which the leptons (e^+, e^-) escape from the system (emission region). In the quasi-steady state, the injection is balanced by radiative cooling and/or particle escape.

The cooling rate of electrons via radiative losses is significantly higher than protons, inside the blob. Hence the escape timescale is relatively higher. In this work, we consider the escape to be independent of energy and time, given by the dynamical timescale $t^e_{\rm esc} = t_{\rm dyn} = R/c$. Hence, we do not consider diffusion losses in this case, which becomes more important for hadrons. We calculate $N_e(E_e, t)$ at a time much greater than that required to obtain the steady state, corresponding to the injection spectrum $Q_{\rm e}(E_{\rm e})$. Hence, all variabilities are averaged out and GAMERA yields the quiescent state photon spectrum. We denote the doppler factor of relativisting beaming for photons coming out from the jet by $\delta_D = [\Gamma(1 - \beta\cos\theta)]^{-1}$. We denote the bulk Lorentz factor by Γ, and βc is the velocity of the emitting plasma. $\theta \lesssim 1/\Gamma$ is the viewing angle of the blazar with respect to the emission direction. The synchrotron and SSC luminosities are doppler boosted by δ_D^4 in the observer frame [225]. The kinetic power in electrons in the AGN frame is given by

$$L_{\rm e} = \pi R^2 \Gamma^2 c u'_e \tag{3.5}$$

where the energy density of electrons in the comoving frame of the jet is given by $u'_e = (1/V) \times \int_{E_{e,\rm min}}^{E_{e,\rm max}} dE_e\ Q(E_e)E_e$, and V is the volume of the emitting blob. The luminosity in magnetic field is the total power carried as Poynting flux,

$$L_{\rm B} = \frac{1}{8} R^2 \Gamma^2 \beta c B^2 \tag{3.6}$$

3.2.2 Hadronic modeling

Now, alongside electrons, the hadrons are also accelerated in the jets of AGNs. In this simplistic approach we justify our model using protons as the contributing particle to the hadronic channel. The maximum acceleration energy of cosmic rays can be estimated from the Hillas condition [8],

$$E_{\rm p,max} \sim 2\beta c Z e B R \tag{3.7}$$

[1] http://libgamera.github.io/GAMERA/docs/main_page.html

Now, protons are not cooled sufficiently by radiative processes inside the jet and the particle spectrum over a sufficiently long time period is balanced by only injection and escape. Hence, empirically $N_p(E_p) = t_{\rm dyn} Q_p(E_p)$. We show later, escape dominates over photohadronic interaction rate for protons. Hence, we assume that protons are injected into the ISM following the power-law spectrum,

$$N_p(E_p) = \frac{dN}{dE_p} = A_p E_p^{-\alpha} \tag{3.8}$$

Since both leptons and hadrons are accelerated by the same processes, we assume the same injection spectral index throughout. We consider $E_{\rm p,min} = 0.1$ EeV and $E_{\rm p,max} = 10$ EeV. Instead of an exponential cutoff, we consider a steep cutoff. The reason for this is two-fold. The spectrum of secondary photons, resulting from UHECR interactions and electromagnetic cascade, is primarily governed by the CMB and/or EBL photon density, along with EGMF. Hence, the signatures of an exponential factor in the injection spectrum is greatly obscured. Also, the low value of $E_{\rm p,max}$ ensures that majority of interactions is with EBL photons, relatively close to Earth.

The seed photons for photohadronic interactions inside the jet are synchrotron and SSC photons. The timescale of interactions is calculated by [182],

$$\frac{1}{t_{\rm p\gamma}} = \frac{c}{2\gamma_p^2} \int_{\epsilon_{th}/2\gamma_p}^{\infty} d\epsilon'_\gamma \frac{n(\epsilon'_\gamma)}{\epsilon'^2_\gamma} \int_{\epsilon_{th}}^{2\epsilon\gamma_p} d\epsilon_r \sigma(\epsilon_r) K(\epsilon_r) \epsilon_r \tag{3.9}$$

where $\sigma(\epsilon_r)$ and $K(\epsilon_r)$ are the cross-section and inelasticity respectively of photopion production or Bethe-Heitler pair production as a function of photon energy ϵ_r in the proton rest frame [69, 81, 226, 227]. $\rm n(\epsilon'_\gamma)$ is the seed photon density per unit energy interval as a function of photon energy ϵ'_γ in the comoving jet frame. It is related to the observed photon spectrum by the relation [228, 229],

$$4\pi R^2 c\, \epsilon'^2_\gamma n(\epsilon'_\gamma) = 4\pi d_L^2 \delta_D^{-p} \left(\epsilon_\gamma^2 \frac{dN_\gamma}{d\epsilon_\gamma dt dA} \right)_{\rm obs} \tag{3.10}$$

where $p = n + 2$ and $n = 2, 3$ for continuous jet and a moving sphere respectively. The subscript 'obs' in Eqn. (3.10) represents the quantity in the observer frame. The photon energy transforms as $\epsilon_\gamma = \delta_D \epsilon'_\gamma/(1+z)$. For a source at redshift z from the observer, $d_L = (1+z)d_c$ is the luminosity distance and d_c is the comoving distance. The escape timescale of protons from the source is given as,

$$t^p_{\rm esc} = \frac{R^2}{4D} \tag{3.11}$$

where we write the diffusion coefficient as, $D = D_0 (E/E_0)^{2-q}$, where q is the turbulence spectral index and is taken to be $q = 3/2$ for the Kraichnan model. The acceleration timescale is calculated from,

$$t^p_{\rm acc} \simeq \frac{20\eta}{3} \frac{r_L}{c} \simeq \frac{20\eta}{3} \frac{\gamma_p m_p c}{eB} \tag{3.12}$$

η is the ratio of the mean magnetic field energy density to the turbulent magnetic field energy density [51]. We consider $\eta = 1$ in our calculations.

The protons which escapes from the jet travel extragalactic distances to interact with the CMB and EBL photons, and produces secondary electrons, positrons, photons, and neutrinos by Bethe-Heitler pair production or photopion interactions.

$$p + \gamma_{bg} \rightarrow p + e^+e^- \tag{3.13}$$

$$p + \gamma_{bg} \rightarrow \Delta^+ \rightarrow \begin{cases} n + \pi^+ \\ p + \pi^0 \end{cases} \tag{3.14}$$

The neutral pions decay to produce γ photons ($\pi^0 \rightarrow \gamma\gamma$) and the charged pions decay to produce neutrinos ($\pi^+ \rightarrow \mu^+ + \nu_\mu \rightarrow e^+ + \nu_e + \overline{\nu}_\mu + \nu_\mu$). The secondary photons and electrons can initiate electromagnetic cascades down to GeV energies. The secondary γ photons interact with cosmic background radiations and universal radio background (URB) leading to Breit-Wheeler pair production or double pair production. The relativistic cascade electrons and positrons also lose energy by synchrotron radiation on deflections in EGMF, triplet pair production, and IC scattering of background photons. The neutrinos propagate undeflected by the EGMF and unaffected by matter and radiation fields. The proton luminosity required in the AGN frame is calculated as,

$$L_{\rm p} = \pi R^2 \Gamma^2 c u'_p \tag{3.15}$$

We use the public astrophysical simulation framework CRPROPA 3 to propagate the UHECR protons from the source to observer [144] and calculate the flux of secondary particle yields obtained at Earth. CRPROPA 3 provides two external codes, DINT [145] and EleCa [146], to calculate the development of EM cascades. DINT solves the transport equations to produce the observed spectrum and is thus computationally more efficient. EleCa, on the other hand, does a full Monte Carlo tracking of individual particles. For 1D simulations, DINT can also be combined with EleCa or CRPROPA, whereby particles above a specified crossover energy are simulated using Eleca or CRPROPA and the remaining part below the crossover is calculated from DINT [147]. The crossover energy is usually chosen to be 0.1 EeV. We propagate the EM particles produced from UHECR interactions using DINT only, since we are interested in the γ-ray spectrum peaking at TeV energies. We consider the Gilmore et al. EBL model [170] and a random turbulent EGMF with a Kolmogorov power spectrum of RMS field strength $B_{\rm rms} = 10^{-5}$ nG.

The total luminosity of the HBL is calculated from the sum of individual kinetic powers in the jet $L_{\rm jet} = L_{\rm e} + L_{\rm p} + L_{\rm B}$. We compare the obtained value of $L_{\rm jet}$ with the Eddington luminosity $L_{\rm Edd}$ of the SMBH. Thus, we can check whether a scenario that invokes UHECR interactions can account for the origin of γ-rays observed at the highest energies from the HBLs.

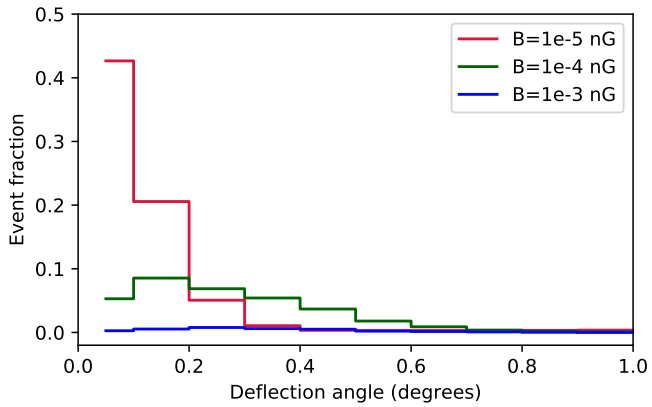

Figure 3.2: Distribution of propagated UHECRs as a function of deflection angle in a random turbulent EGMF.

3.3 Line-of-sight UHECR Interactions

3.3.1 Deflections in EGMF

We calculate the survival rate of UHECRs and hence the secondary particles along the line of sight of the observer, for various magnetic field strengths. The root mean square (rms) deflection in the trajectories of cosmic rays on propagation over a distance D, in a random turbulent magnetic field with coherence length l_c, can be approximated as [133],

$$\Phi_{\rm rms} \approx 4^\circ \frac{60\ {\rm EeV}}{E/Z} \frac{B_{\rm rms}}{10^{-9}\ {\rm G}} \sqrt{\frac{D}{100\ {\rm Mpc}}} \sqrt{\frac{l_c}{1\ {\rm Mpc}}} \tag{3.16}$$

The Pierre Auger Collaboration has been doing correlation analysis of UHECR arrival directions with various catalogs of γ-ray emitting sources. The correlation with the AGN distribution yields the following condition for turbulent EGMF models [131],

$$B_{\rm rms}\sqrt{l_c} \leqslant 10^{-9} G \sqrt{1\ {\rm Mpc}} \tag{3.17}$$

From Eqn. 3.16, the deflection of a 1 EeV proton traversing a distance of 1 Gpc from the source to the observer through a random turbulent EGMF with $B_{\rm rms} = 10^{-5}$ nG comes out to be $\approx 0^\circ.0076$. However for astrophysical scenario we consider the energy of the UHECR protons are not monoenergetic, but follows the distribution accorrding to Eqn. 3.8.

To obtain an order of magnitude estimate of the survival rate of UHECR protons along the line of sight in various $B_{\rm rms}$, we have performed test simulations using CRPROPA 3 for the propagation of an injected UHECR distribution through a distance of 1000 Mpc from its source to the observer. We do this for different values of $B_{\rm rms}$ corresponding to a magnetic field, whose Fourier modes are taken from a Gaussian distribution and $\langle |B(\mathbf{k})|^2 \rangle$ is given by a Kolmogorov power spectrum. We set the value of turbulence correlation length $l_c = 1$ Mpc for all the test cases, and hence the radius of the observer sphere centered at Earth is also set to $R_{\rm obs} = 1$ Mpc. Protons are injected following a spectrum

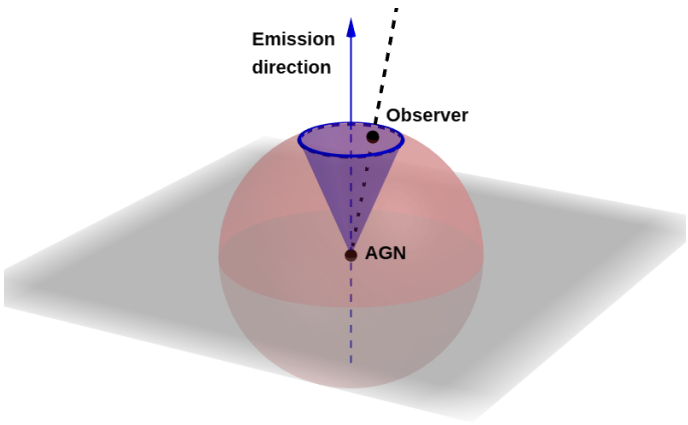

Figure 3.3: The emission from the blazar centered on the sphere is assumed to be constricted within the blue cone. The black dashed line represents the line of sight towards the center of the sphere for an observer on the surface.

$dN/dE_p \propto E^{-2}$ within the energy range $0.1 - 10$ EeV. We consider all relevant energy loss proceses, viz., photopion production, Bethe-Heitler pair production, nuclear decay and adiabatic energy loss due to the expansion of the Universe. The momentum vector of the particles are initially directed towards the position of the observer. Deflection suffered during propagation is measured with respect to this direction. The final amount of deflection on arrival at the surface of the observer sphere is shown in Fig. 3.2 for the entire UHECR population. The observed events are binned at intervals of $0°.1$. The fraction of events within the bin $0° - 0°.1$, i.e., close to the initial direction of propagation will have the most significant contribution in the spectrum of secondary particles, originating from line of sight UHECR interactions.

From Fig. 3.2, we see that the survival rate of UHECRs increases with decreasing $B_{\rm rms}$, as well as, with higher containment angles. Since we are interested in the contribution from UHECR interactions to the observed γ-ray SEDs of HBLs, we find the survival rate of UHECRs within $0°.1$ of the direction of propagation in which the observer is positioned and denote it by ξ_B. Accordingly, from the results of the 3D simulations, we consider $B_{\rm rms} = 10^{-5}$ nG for the rest of our study, to increase the fraction of events close to the direction of jet emission axis of HBLs. In some studies, a lower bound of $\sim 10^{-6}$ nG is found for the EGMF [230]; while others have estimated it to be, as low as, 10^{-7} nG [28] or 10^{-8} nG [231]. An increase in the survival rate along the direction of emission for blazars will essentially increase the detection rate along the line of sight of the observer. The Fermi-LAT angular resolution to observe a single photon at $E > 10$ GeV is $\sim 0°.15$ [216].

3.3.2 Luminosity requirement in UHECRs

Fig. 3.3 shows the jet emission axis by a vertical solid line directed upwards. The sphere has a radius d_L equivalent to the luminosity distance from the source to the observer. The source is at the center of the sphere. The cone is the extrapolation of the jet emission from

Table 3.1: UHECR model parameters

HBL	z	d_L	ξ_B	$f_{\rm CR}$	f_ν
1ES 1011+496	0.212	1085 Mpc	0.45	0.084	0.00064
1ES 0229+200	0.140	687 Mpc	0.46	0.052	0.00039
1ES 1101–232	0.186	938 Mpc	0.48	0.079	0.00058
1ES 0414+009	0.287	1529 Mpc	0.39	0.085	0.00077

the HBL, with a semi-apex angle equal to the jet opening angle $\theta_{\rm jet}$. The observer is at the position where the dashed line pierces through the surface of the sphere. The line of sight is thus directed towards the center of the sphere along the line passing through the observer, and may also lie outside the emission cone. When the line of sight lies outside the jet opening angle, the collimation of outflow along the observer's direction becomes poor and thus the required jet power increases. However, we do not include any angular dependence for varying observer position in our analysis and assume the jet emission stays collimated along the line of sight. The observer sphere is not shown in this diagram since $R_{\rm obs} \ll d_L$. Assuming the angle between the emission direction and line of sight to be a few degrees, the viewing angle $\theta \lesssim 1/\Gamma$. Now, the flux of secondary cascade photons will be distributed across the area of the spherical cap subtended on the surface of the sphere by the emission cone.

DINT solves the transport equation in 1D for the propagation and electromagnetic cascade of secondary e^+, e^- and γ photons produced from UHECR interactions on CMB and EBL. Hence, we run 1D simulations in CRPROPA for the propagation of UHECRs, producing EM particles, to calculate the secondary photon flux at the Earth. To find the flux intercepted by the observer's line of sight in the presence of an EGMF, we multiply this photon flux by ξ_B. Although ξ_B is calculated for an observer sphere of radius $R_{\rm obs} = 1$ Mpc, this introduces little error as $l_c = 1$ Mpc and also, the mean free path for energy loss of UHECRs in the energy range considered is much greater than this value [133, 147]. In this process, we already reject the contribution to secondary photons from all UHECRs outside of $0^\circ.1$ w.r.t the propagation direction along which the observer is located.

Now, $L_p = L_p^{E<0.1\ \rm EeV} + L_p^{E>0.1\ \rm EeV}$. Thus, the luminosity required in UHECR protons, $L_{\rm UHECR}$ can be calculated from the expression,

$$L_{\rm UHECR} = L_p^{E>0.1\ \rm EeV} = \frac{2\pi d_L^2 (1-\cos\theta_{\rm jet})}{\xi_B f_{\rm CR}} \int_{\epsilon_{\gamma,\rm min}}^{\epsilon_{\gamma,\rm max}} \epsilon_\gamma \frac{dN}{d\epsilon_\gamma dA dt} d\epsilon_\gamma \tag{3.18}$$

where $2\pi d_L^2(1-\cos\theta_{\rm jet})$ is the area of the spherical cap region. We consider typical values of $\theta_{\rm jet} \sim 0.1$ radians [232, 233]. $f_{\rm CR}$ is the ratio of the power in produced secondary photons $L_{\gamma,\rm p}$ due to propagation of UHECRs and cascade of resulting EM particles in all directions, to the injected UHECR power $L_{\rm UHECR}$. Both ξ_B and f_{CR} will be a function of propagation distance. The values of these quantities obtained for the sources in our study,

while modeling the VHE γ-ray component, are listed in Table 3.1. The integral is over the flux of secondary photons of hadronic origin, required to fit the observed blazar SED. We obtain the secondary EM particles and cascade photons from 1D simulations, and account for the conical distribution by calculating the luminosity according to Eqn. (3.18).

3.3.3 EBL attenuation effect on γ-rays

The observed photon flux from inside the jet will be attenuated due to absorption in EBL and is taken into account using the Gilmore *et al.* model. The optical depth for a γ-ray observed at energy E_γ is calculated by the following integral along the line of sight to the target at redshift z [170],

$$\tau(E_\gamma, z_0) = \frac{1}{2}\int_0^{z_0} dz \frac{dl}{dz} \int_{-1}^{+1} du(1-u) \times \int_{E_{\rm min}}^{\infty} dE_{\rm bg}\, n(E_{\rm bg}, z)\sigma(E_\gamma(1+z), E_{\rm bg}, \theta) \tag{3.19}$$

where $E_{\rm min}$ is the redshifted threshold energy $E_{\rm th}$ for a background photon to interact with a γ-ray of energy E_γ.

$$E_{\rm min} = E_{\rm th}(1+z)^{-1} = \frac{2m_e^2c^4}{E_\gamma(1+z)(1-\cos\theta)} \tag{3.20}$$

$n(E_{\rm bg}, z)$ is the proper density of target background photons as a function of energy $E_{\rm bg}$ and redshift z, and $u = \cos\theta$. The cosmological line element dl/dz is given by,

$$\frac{dl}{dz} = \frac{c}{(1+z)H_0} \frac{1}{\sqrt{\Omega_m(1+z)^3 + \Omega_\Lambda}} \tag{3.21}$$

The attenuation affects only the high energy end of the SSC spectrum, as can be seen in Fig. 3.5 producing a flux $F_\gamma^{\rm obs}(E,z) = F_\gamma^{\rm int}(E,z)\exp[-\tau(E_\gamma, z_0)]$. An intuitive treatment of $\gamma\gamma_{bg}$ attenuation is also done in [234] (see Eqn. 17 there). The attenuation effect on the cascade photons due to the EBL is incorporated in the DINT code. We implement the Gilmore et al. EBL model in DINT for the propagation and cascade initiated by secondary EM particles. Our results do not depend significantly on the choice of other recent EBL models, e.g., [168, 169].

3.3.4 Interaction timescales inside the source

We consider the HBL sources: 1ES 1011+496, 1ES 0229+200, 1ES 1101–232, and 1ES 0414+009. These representative class of HBLs covers a wide range in redshift (indicated in Table 3.1) and hence provides a laboratory for testing the plausibility of γ-ray production from UHECR interactions. First, we calculate the timescale of photopion ($t_{p\gamma}$) and Bethe-Heitler interactions ($t_{\rm BH}$), inside the jet and compare it with the escape timescale $t_{\rm esc}$, using Eqn. (3.9) and Eqn. (3.11). The seed photons are considered to be synchrotron as well as IC photons. We also calculate the acceleration timescale t_{acc} using Eqn. (3.12). The various timescales and interaction rates are shown in Fig. 3.4. In the Bohm diffusion

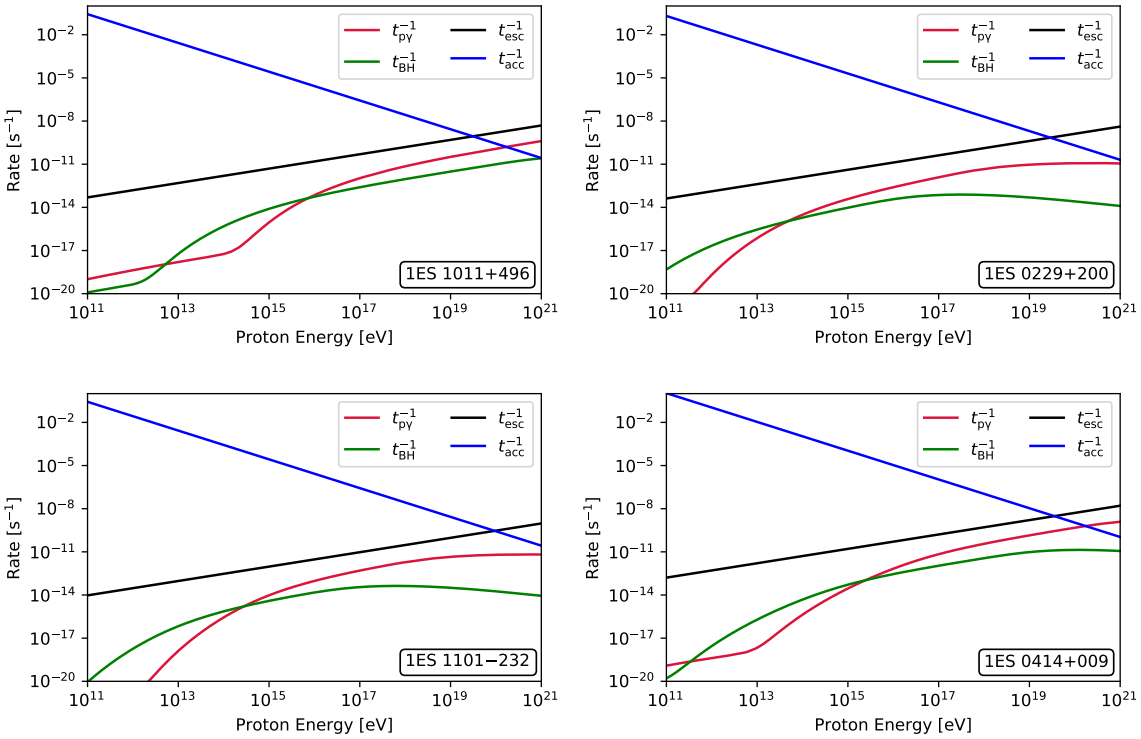

Figure 3.4: Timescale of photohadronic interactions inside the jet, with target photons from synchrotron and IC emission, calculated using Eqn. (3.9). The acceleration timescale ($t_{\rm acc}$) and escape timescale ($t_{\rm esc}$) are also shown for comparison, calculated from Eqn. (3.11) and Eqn. (3.12) respectively. The Bohm condition gives the minimum diffusion leading to a lower value of t_{esc}. Particles can be more diffusive than this and thus, $t_{\rm esc}$ is adjusted by varying the diffusion coefficient D_0 such that acceleration dominates up to 10^{19} eV (see text for more details). The $p\gamma$ and Bethe-Heitler interaction rates are found to be orders of magnitude less than escape rate. The photon spectrum from π^0 decay inside the jet is calculated and found to be $\sim$ 10 orders of magnitude less than the peak VHE flux, for the same normalization as required for contribution from UHECR interactions.

approximation, the difffusion co-efficient can be written as $D = \eta r_L c/3$. However, particles can be more diffusive than this and we consider the Kraichnan model of diffusion $D = D_0(E/E_0)^{0.5}$ with the diffusion co-efficient D_0 adjusted between 10^{27} to 10^{30} cm^2/s, such that the acceleration rate dominates over escape rate at least up to $E = 10^{19}$ eV. The maximum acceleration energy of protons ($E_{\rm p,max}$) inside the blob is found to be a few EeV from Eqn. (3.7), for the sources studied. In view of the dominance of acceleration over escape and uncertainties in fit parameters, we set $E_{\rm p,max} = 10^{19}$ eV for all the sources considered. The Eddington luminosity of the blazars can be calculated using the expression $L_{\rm Edd} = 10^{47}(M_{\rm BH}/10^9 M_\odot)$ erg/s. In the absence of an estimated BH mass, we consider $M_{\rm BH} = 10^9\ M_\odot$ for 1ES 1101–232. For the other sources, the masses of the SMBHs are taken from Ref. [235]. We assume $\delta_D \simeq \Gamma$ in our calculations, which is valid for a viewing

angle of the order of few degrees.

3.4 Multiwavelength SED Modeling

3.4.1 Representative HBL sources

1ES 1011+496: The optical data, X-ray data and radio-to-X-ray flux ratio show typical properties of an HBL [236, 237]. It is situated at a redshift $z = 0.212$ and the VHE γ-ray emission was first discovered by MAGIC observations triggered by an optical outburst in March 2007 [238]. The source has been well observed in $0.1 - 300$ GeV band by Fermi-LAT [239] and $0.3 - 10$ keV band by Swift-XRT [240]. The source is also listed in the second catalog of hard Femi-LAT sources. A photohadronic scenario to explain the high-energy SED is employed in [241]. The flux value of the low- and high-energy peak are comparable. We find, a pure-leptonic model is unable to cover the highest energy data points due to EBL attenuation. Increasing $E_{\rm e,cut}$ worsens the fit for synchrotron spectrum. In the lepto-hadronic fit, photon spectrum from UHECR interactions can indeed explain the highest energy data points.

1ES 0229+200: This BL Lac object at redshift $z = 0.140$ [242] shows an extremely hard intrinsic TeV spectrum with the synchrotron spectrum peaking at exceptionally high energies near hard X-ray regime [243]. It has one of the highest inverse-Compton (IC) peak frequency and the narrowest electron distribution among the extreme blazars known [244]. The source was first discovered by HESS in 2004 [245]. The X-ray-to-radio flux ratio classifies it as an HBL [246]. The SED in the high-energy (HE) band has been modeled using reprocessed GeV emission from pair production on EBL and subsequent cascade [247], using a similar method applied to γ-ray bursts in Ref. [248]. The HE data is obtained from Fermi-LAT [249] and the VHE data is obtained from HESS [250] and VERITAS collaboration [251, 252]. In our pure-leptonic modeling, there is no significant change in the SSC spectrum on increasing $E_{\rm e,cut}$ beyond the value considered, due to KN suppression. We show, the necessity of an additional component is inevitable and the spectrum arising from UHECR interactions well explains the highest energy data points.

1ES 1101–232: This HBL resides in a elliptical host galaxy at redshift $z = 0.186$. It was first detected by Ariel-5 X-ray satellite and was misidentified with the Abell 1146 galaxy cluster at redshift $z = 0.139$ [253, 254]. The optical and radio data led to the correct identification as a BL Lac object [255, 256]. The highest energy data points exhibit very hard TeV spectra, which has been explained earlier using hadronic origin inside the jet emission region [257]. The HE and VHE γ-ray data is obtained from Fermi-LAT and HESS observations [250, 258]. It can be seen that that the highest energy data points are not well-covered by the SSC spectrum alone in a pure-leptonic fit. The fit improves considerably in the entire VHE range with the addition of the hadronic component originating in line-of-sight UHECR interactions.

1ES 0414+009: The optical spectrum of this HBL at redshift $z = 0.287$ is described

by the sum of the emission due to a standard elliptical galaxy and a relatively flat power law [259]. It was first detected by HEAO 1 satellite [260] in the energy range 0.2 keV − 10 MeV. It is one of the furthest VHE blazar with very hard TeV γ-ray spectrum and well-determined redshift. The supermassive black hole (SMBH) at the center has a mass $2 \times 10^9 M_\odot$ [235]. The HE (100 MeV − 100 GeV) data is obtained from Fermi-LAT and the source is listed in the Fermi 4FGL catalog. The VHE ($E > 100$ GeV) γ-ray data is taken from observations by HESS [261] and VERITAS [262] collaborations. Despite the attenuation due to EBL background, a good fit to the observed SED is achieved using a pure-leptonic model alone. However, the fit to data points at the highest energy improves on adding the photon spectrum from UHECR interactions.

3.4.2 SEDs using lepto-hadronic model

The synchrotron spectrum is modeled using a one-zone leptonic emission in GAMERA. The jet parameters obtained from the fit is used to calculate the SSC spectrum and is adjusted to extend up to the highest energy possible. Beyond this energy, the hadronic contribution dominates. The photon spectrum produced in UHECR interactions, peaking at ∼ TeV energies, is incorporated to well explain the data points in the entire VHE range. The synchrotron and SSC luminosities are doppler boosted in the observer frame by δ^4. Here the multiwavelength data is taken for the quiescent state. The fit to photon SEDs obtained from a pure leptonic origin are presented in the left panels of Fig. 3.5. The corresponding parameter values are given in top section of Table 3.2. Petropoulou *et al.* [263] have done a detailed analysis of hadronic losses inside the jet resulting in photon spectrum in the high-energy regime. The proton jet power is much higher in Petropoulou *et al.* [263] compared to ours. We have calculated the efficiency of $p\gamma$ interactions inside the jet using the formalism in Ref. [264] and found that the photon spectrum resulting from π^0 decay is insignificant in our case compared to the observed flux. Thus, we consider the interactions of UHECR protons only, during propagation over cosmological distances. The SSC flux depends on the radius of the spherical blob of emitting zone inside the jet and is adjusted suitably in case of a lepto-hadronic fit. The fit parameters used to model the observed SEDs using a combined leptonic + hadronic (UHECR) scenario are listed in the bottom section of Table 3.2 and the multiwavelength fits are presented in the right panels of Fig. 3.5.

3.5 Multi-messenger Constraints

3.5.1 UHECRs from HBLs

Now, since the survival rate of UHECRs within $0°.1$ of the propagation direction towards the observer is found to vary between 39% and 48% at a distance of 1 Mpc from the observer and the turbulent correlation length is taken to be $l_c = 1$ Mpc, UHECR events from the source should arrive at Earth. Although γ-rays travel mostly undeflected once

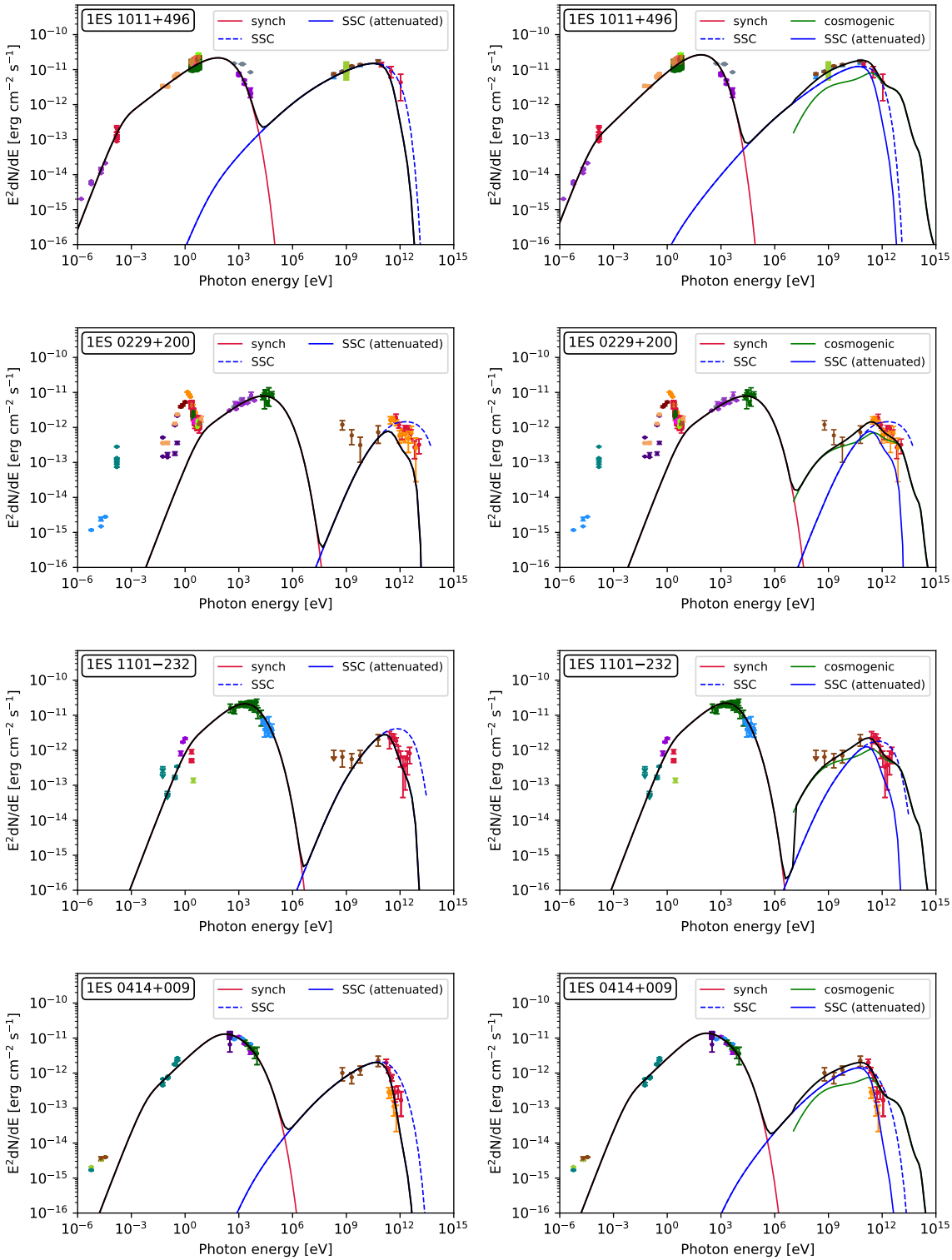

Figure 3.5: Multiwavelength spectrum of the HBLs, modeled using a pure leptonic model (*left*) and a leptonic + hadronic model (*right*).

Table 3.2: Fit parameters for the multiwavelength SED modeling in Fig. 3.5

HBL	$E_{\mathrm{e,min}}$ [GeV]	$E_{\mathrm{e,cut}}$ [GeV]	α	R [cm]	B [Gauss]	δ_D	L_{e} [erg/s]	L_{B} [erg/s]	L_{UHECR} [erg/s]	L_{Edd} [erg/s]
Pure leptonic model										
1ES 1011+496	0.08	75.0	2.2	1.5×10^{17}	0.024	20	5.8×10^{38}	1.9×10^{43}	–	
1ES 0229+200	10.00	1500.0	2.2	1.0×10^{16}	0.015	40	1.3×10^{38}	1.3×10^{41}	–	
1ES 1101–232	5.70	550.0	2.0	8.4×10^{16}	0.020	22	6.0×10^{37}	5.1×10^{42}	–	
1ES 0414+009	0.20	200.0	2.0	7.0×10^{16}	0.080	22	7.6×10^{37}	5.7×10^{43}	–	
Leptonic + hadronic (UHECR) model										
1ES 1011+496	0.04	65.0	2.0	2.2×10^{17}	0.020	20	3.8×10^{38}	2.9×10^{43}	4.8×10^{44}	5.1×10^{46}
1ES 0229+200	10.00	1500.0	2.2	1.0×10^{16}	0.015	40	1.3×10^{38}	1.3×10^{41}	2.6×10^{43}	1.7×10^{47}
1ES 1101–232	5.70	500.0	2.0	1.4×10^{17}	0.020	22	3.5×10^{37}	1.4×10^{43}	3.0×10^{43}	1.0×10^{47}
1ES 0414+009	0.20	200.0	2.0	9.0×10^{16}	0.080	22	5.9×10^{37}	9.4×10^{43}	1.0×10^{44}	2.0×10^{47}

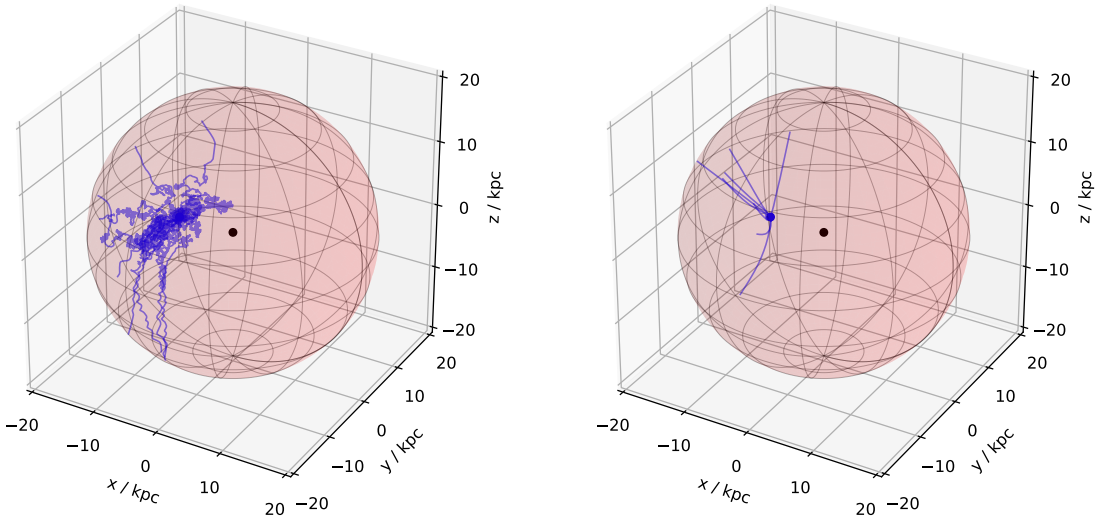

Figure 3.6: 3D trajectories of 10 UHECR anti-protons emitted isotropically and backtracked from the Earth in Janson & Farrar magnetic field of the Galaxy upto a halo radius of 20 kpc. The black dot indicates the Galactic center. See text for more details. *Left:* For $E = 0.1$ EeV, the deflections are high and no directionality information can be retained. *Right:* For $E = 10$ EeV, the deflections are small and the anti-protons travel in almost straight lines, escaping the Galaxy.

produced, the Galactic magnetic field (GMF) being many orders of magnitude stronger than the EGMF, can deflect the UHECRs significantly. The deflection suffered by UHECRs in the GMF can be approximated as [265],

$$\theta_{\rm def,MW} \approx \frac{0.9^\circ}{\sin b}\left(\frac{60\ {\rm EeV}}{E/Z}\right)\left(\frac{B}{10^{-9}\ {\rm G}}\right)\left(\frac{h_{\rm disk}}{1\ {\rm kpc}}\right) \tag{3.22}$$

where b is the galactic latitude of the source and $h_{\rm disk}$ is the height of the Galactic disk. The GMF may create a strong shadowing effect on the true location of the sources [266]. This makes a direct estimation of the observed event rate difficult. The computational efficiency of forward propagation accounting for magnetic field effects over large distances with a point observer is very low in CRPROPA 3. We do backtracking simulations of cosmic rays with opposite charge from the observer to the edge of the Galaxy for showing a graphical representation of UHECR trajectories in GMF. We consider a realistic magnetic field, such as that of Jansson & Farrar field model (JF12) with both random striated and random turbulent components [138, 139]. For backtracking, 10 UHECR anti-protons are injected isotropically from the Earth and is similar to protons traveling towards Earth in forward simulations. In JF12 model the field is set to zero for $r > 20$ kpc and in a 1 kpc radius sphere centered on the Galactic center. The trajectories originating from Earth terminates at the boundary of the 20 kpc radius sphere. We consider two such cases when the UHECR protons are observed at Earth with $E_{\rm obs} = 0.1$ EeV and 10 EeV. The resulting trajectories are shown in the left and right panels of Fig. 3.6, respectively. The black and

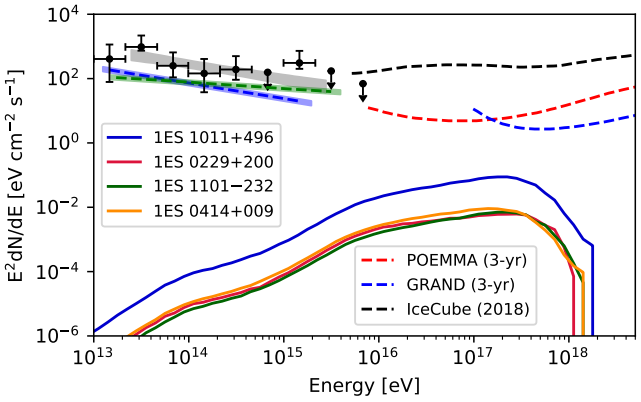

Figure 3.7: All-flavor neutrino flux at Earth produced in the same UHECR interactions as producing EM particles. The POEMMA and GRAND-200K sensitivities are multiplied by 4π steradians to compare with the neutrino fluxes in same units. The differential upper limit on extremely-high-energy cosmic neutrino flux by IceCube is also shown [162]. The black data points show the observed astrophysical diffuse neutrino flux [97]. The flux upper limit from 2LAC blazars is shown using equal weighting for power-law with spectral index 2.5 (blue shaded region) and 2.2 (green shaded region) [98].

blue dots represent the Galactic center and the Earth at a distance of 8.5 kpc from the Galactic center, respectively.

An estimate of the number of UHECR events that can be expected at the Pierre Auger observatory (PAO) in Malargüe, Argentina can be calculated from,

$$N_{\rm evt,p} = \frac{1}{\xi_B}\frac{\Xi\omega(\delta)}{\Omega}\int_{E_{\rm th}^{\rm obs}}^{E_{\rm max}^{\rm obs}}\frac{dN}{dE}dE \tag{3.23}$$

where $\omega(\delta)$ is the relative exposure at a point source in the sky compared to the largest exposure on the sky [267] and Ξ is the total integrated exposure over the detector's field of view. Here the additional factor ξ_B accounts for UHECRs surviving within $0^\circ.1$ of the initial propagation direction, at a distance of 1 Mpc from Earth. Since the maximum UHECR energy $E_{\rm p,max}$ is taken to be only 10 EeV for all the sources, the UHECR events are subjected to large deflections in the GMF. The value of $E_{\rm max}^{\rm obs}$ being smaller compared to the GZK cutoff energy [268, 269] or, the energy threshold for AGN correlation analysis by PAO [131], an intermediate-scale anisotropy study is difficult to do. Also in large-scale anisotropic studies, the most significant signal found is the dipolar modulation in right ascension at energies $E > 8$ EeV [130, 142]. In the latter case, a statistically significant oversampling at any grid point in the sky, compared to the background events is unexpected owing to the deflection and huge number of observed events at these low energies. Therefore, if the energy of the UHECRs from the HBLs we considered is restricted to below 10 EeV as required by our model, then it will be difficult to detect them directly as discussed in [28].

3.5.2 Cosmogenic neutrinos

Since neutrinos travel unhindered by interactions and undeflected by magnetic fields, the neutrinos produced from the sources near to the line-of-sight direction are expected to arrive at Earth. The obtained luminosity in neutrinos is constrained from the luminosity requirement in UHECRs to explain the VHE γ-ray flux. Thus, we can write,

$$L_\nu = L_{\rm UHECR} \times f_{\rm CR\to\nu} \times \xi_B \tag{3.24}$$

where $f_{\rm CR\to\nu}$ is the ratio of the power in produced secondary neutrinos $L_{\nu,p}$ due to the propagation of UHECRs in all directions, to the injected UHECR power $L_{\rm UHECR}$. This gives the normalization of secondary neutrino flux arriving within 0.1 degrees of the direction of propagation in which the observer is situated. The resulting all-flavor neutrino fluxes are shown in Fig. 3.7. The extrapolated 3-year sensitivities for the proposed future detectors POEMMA [160, 178] and the 200,000 antenna array GRAND-200K [161, 176] are also shown. The detector sensitivities are multiplied by 4π steradians to obtain the isotropic sensitivity that can be compared with the calculated neutrino flux in units of eV cm^{-2} s^{-1}. A 3-years full operation by these detctors will not be sufficient to constrain the neutrino flux from the sources studied.

The secondary neutrino flux from 1ES 1011+496 is higher compared to the other sources. This is expected because of its higher flux value of the high energy bump in the multiwavelength SED, leading to a higher γ-ray flux required from hadronic interaction channels and hence a higher proton luminosity. The neutrino flux obtained peaks at 2.2×10^{17} eV. The IceCube 8-year differential flux upper limit [162], isotropized at this peak-energy, is of the order of 10^3 times higher than the peak flux from 1ES 1011+496, as shown in figure. Thus a possibility of detection of the neutrino flux obtained from the BL Lac objects in our study is unfavorable. The lower energy peak in the neutrino spectrum is not well pronounced because of the proton injection spectral index value $\alpha \approx 2$ considered for the sources. The observed astrophysical diffuse neutrino flux is shown in Fig. 3.7. The grey shaded region indicates the best-fit power law with spectral index ~2.5 [97]. Assuming the neutrino flux follows the measured γ-ray energy flux exactly, the TeV–PeV upper limit from 2LAC blazars is also shown for two spectral indices viz., 2.2 (shown in green shaded region) and 2.5 (shown in blue shaded region). This yields a maximum of 19%–27% contribution of the total 2LAC blazar sample to the observed best-fit value of the astrophysical neutrino flux [98].

3.6 Effects of Maximum UHECR Energy

The spectrum of the observed γ-rays is governed primarily by the EM cascade of secondary particles produced from UHECR interactions on the CMB and EBL. The intrinsic source parameters have little or no effect on the VHE spectrum. However, the luminosity requirements can vary widely with source parameters, particularly $E_{\rm p,max}$, provided

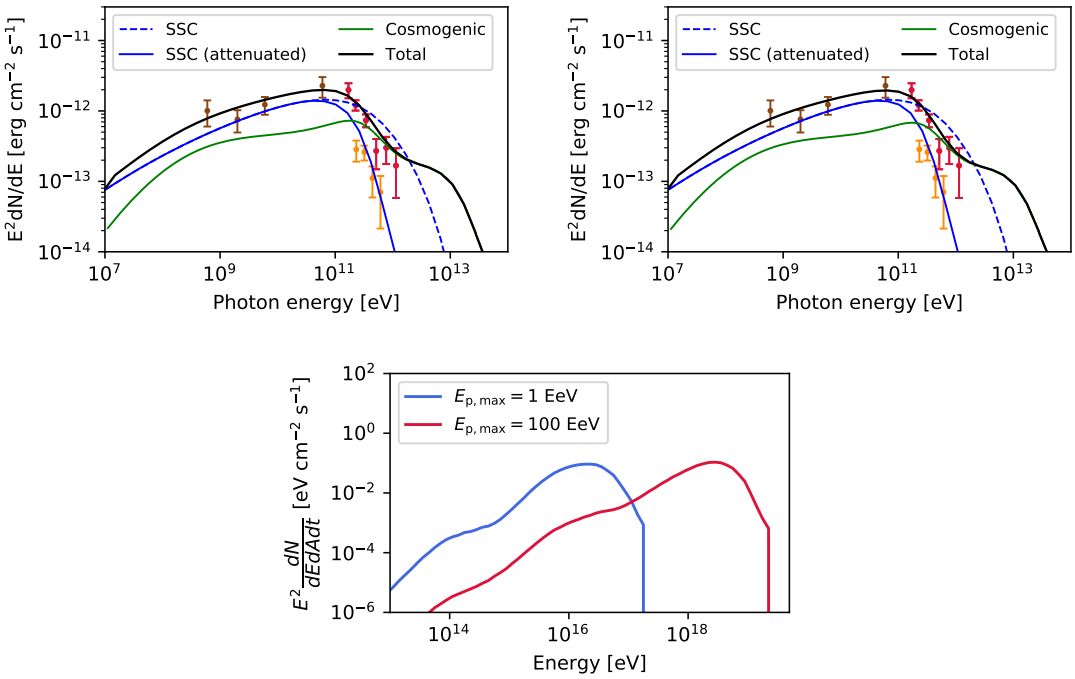

Figure 3.8: The high-energy spectrum of the HBL 1ES 0414+009, fitted with varying maximum proton energy at the source. The left and middle panels show the fit for $E_{\rm p,max}$ = 1 and 100 EeV, respectively. Not much variation can be seen in the spectral features. However, due to different survival rates in the EGMF and different energy conversion efficiency from UHECRs to γ-rays and neutrinos, the luminosity requirement at the source is different. The right panel shows the neutrino fluxes for both cases. See the main text for details.

the UHECRs propagate for distances long enough to traverse multiple mean interaction lengths. In our work, we consider $E_{\rm p,max}$ = 10 EeV based on the Hillas criterion and the comparison between acceleration and escape timescales (cf. Fig. 3.4). But a different value obtained from a different modeling can have a significant effect on $L_{\rm UHECR}$ due to increased or decreased interactions on CMB and EBL. We check the effects due to the choice of maximum proton energy $E_{\rm p,max}$ on luminosity requirements. For this, we consider two values, $E_{\rm p,max}$ = 1 and 100 EeV and fit the high-energy peak of the HBL 1ES 0414+009. This source has the highest redshift among those studied here. As a result, the effect of $E_{\rm p,max}$ variation on the survival rate of UHECRs along the line of sight, after suffering deflections in the EGMF, is expected to be the most prominent. The value of ξ_B is found to be 0.259 and 0.397 for $E_{\rm p,max}$ values of 1 and 100 EeV, respectively. The UHECR injection index is taken to be α = 2, and all other parameters are kept the same as in Sec. 3.4. The ratio of power in produced γ photons to the injected UHECR power, $f_{\rm CR}$ is also calculated. The value of $f_{\rm CR}$ comes out to be 0.0052 and 0.2559, differing by two orders of magnitude, for $E_{\rm p,max}$ values 1 and 100 EeV respectively. The resultant fits are shown in the left and middle panel of Fig. 3.8. The differences are negligible. The lower energy part of the spectrum remains unchanged and hence is not shown.

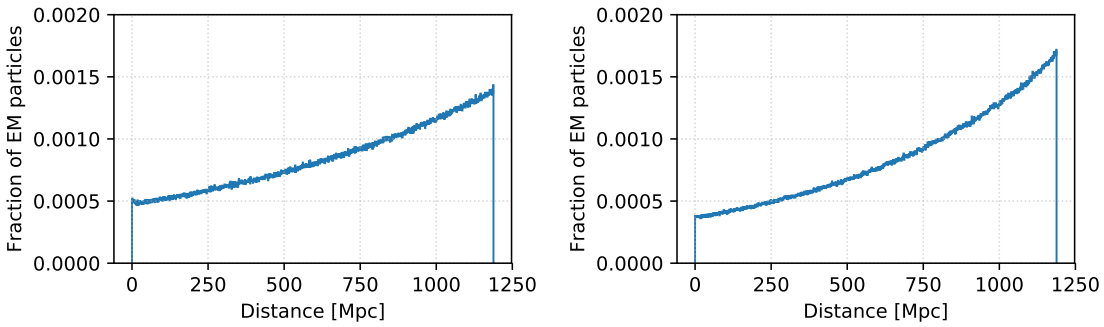

Figure 3.9: Fraction of total EM particles (e^+, e^-, γ) produced from UHECR interactions, binned over distance from the observer, for proton energy cutoff $E_{p,max}$=1 EeV (*left*) and 100 EeV (*right*). The source is at $d_c \sim 1189$ Mpc.

The required luminosity is also found to differ by two orders of magnitude, being 2.47×10^{45} erg/s for $E_{p,max} = 1$ EeV and 3.05×10^{43} erg/s for $E_{p,max} = 100$ EeV. The distribution of EM particles produced from UHECR interactions at distance steps of 1 Mpc from the observer to the source is shown in Fig. 3.9. For higher $E_{p,max}$, more secondaries will be produced near the sources, tending to reduce the observed γ-rays along the line of sight. But, the value of f_{CR} also increases for higher $E_{p,max}$ due to increased photopion production on CMB, resulting in π^0 decay photons, and thus reducing the required value of L_{UHECR}. While for lower $E_{p,max}$, the main contribution to the observed γ-ray signals comes from EM cascade of e^+e^- pairs produced in Bethe-Heitler interactions on CMB and EBL. Thus the relative dominance of various processes changes due to varying maximum energy. This also leaves an imprint on the subsequent neutrino spectrum. Resonant photopion production on CMB with UHECRs of energy $\sim$ 50 EeV produces the so-called GZK neutrinos and shifts the peak flux at higher energy. This can be seen on the right panel of Fig. 3.8.

3.7 Implications & Discussions

⊙ The one-zone leptonic emission model is often found to be inadequate in explaining the high-energy γ-ray spectrum of a number of BL Lac objects. These high-energy BL Lac objects (HBLs) exhibit a hard intrinsic TeV spectrum, which requires an alternate explanation. In many studies, multi-zone emission is employed to fit the broadband spectrum up to the highest observed energies [see, eg., 270, 271]. Among hadronic origin γ-ray models, those which invoke proton synchrotron emission requires extremely high kinetic power and very high values of doppler factor or magnetic field [272]. If protons are cooled efficiently by synchrotron photons produced from accelelerated electrons, the contribution from photopion production, Bethe-Heitler interactions and muon synchrotron emission becomes important [273, 274].

⊙ In this study, we exploit yet another hadronic scenario where the UHECRs escaping

from the jet can interact with cosmic background photons (CMB and EBL), to produce secondary electromagnetic particles. These particles can initiate EM cascades, during propagation over cosmological distances, leading to the production of VHE γ-ray spectrum near the high-energy bump in the blazar SEDs [209]. Hadronic losses inside the blazar jet is found to be insignificant for the jet parameters considered in our model, facilitating the escape of UHECRs. For simplicity, we consider protons as the only UHECRs injected by these sources. We explain the multiwavelength SED of the HBLs by a suitable utilization of this lepto-hadronic model. The parameters for leptonic contribution is adjusted to extend the spectrum up to the highest energies possible and to simultaneously fit the synchrotron spectrum. Beyond this, the contribution from UHECR interactions dominate. The jet power required in such a scenario is calculated and compared with the Eddington luminosity.

⊙ We find, this model is successful in fitting the broadband emission spectrum of selected HBLs without exceeding the luminosity budget. The total proton luminosity $L_{\rm p}$, considering relativistic protons down to $\sim$ 10 GeV energies, will be approximately $5-10$ times of the $L_{\rm UHECR}$ value calculated. Taking this into account doesn't affects the credibility of our model, and the total jet power, in our case, still remains lower than $L_{\rm Edd}$. It is shown in Ref. [28], that required $L_{\rm UHECR}$ increases with increasing values of the injection spectral index α and decreasing values of $E_{\rm p,min}$. They have found that the lower limit on the jet power exceeds the Eddington luminosity for injection spectral index $\alpha > 2.2$ for all the sources considered. In our analysis, we restrict ourselves to $\alpha \leqslant 2.2$.

⊙ The value of ξ_B considered in the analysis is the survival rate of UHECRs within $0^\circ.1$ of the initial propagation direction. This is not the same as $0^\circ.1$ within the line of sight of the observer because the origin of angle is different in the two cases. Such a restriction provides increased constraints, which decreases the observed photon flux and thus increases the required UHECR power. The two has a one-to-one correspondence depending on the source distance. Hence, this factor is important to constrict the propagation within a narrow cone leading to an increased probability of interception by the observer. This is not considered in earlier works, thus reducing the luminosity requirement in UHECRs. If we calculate the survival rate of UHECRs within a smaller deflection angle than 0.1 degrees, a lower value of EGMF will be necessary for a substantial contribution to photon flux from UHECR interactions. The value of $B_{\rm rms}$ considered in our study is 10^{-5} nG, which is higher than the lower limit estimated in [231].

⊙ Secondary charged EM particles produced within 0.1 degrees of the direction of propagation can still get deflected by the EGMF or GMF, reducing the observed cascade flux. This is not accounted for in the study. But it is also possible that contribution from shower development initiated outside of 0.1 degrees of propagation direction is intercepted along the line of sight. But the energy loss timescale of electrons/positrons being very low compared to protons, the fraction of events lost by such EM deflection

should be negligible. Also, calculating ξ_B only up to 1 Mpc introduces very negligible error, because only an infinitesimal fraction of total EM particles are produced nearer to 1 Mpc from the Earth and the coherence length is set to $l_c = 1$ Mpc. We checked the fraction for 1ES 1011+496 at $d_c = 895$ Mpc from 1D simulation, accepting 100% of the produced events along the propagation direction. The fraction of EM events produced at distances less than 1 Mpc is found to be 0.0006.

⊙ Since the acceleration rate dominates over the escape rate up to $\gtrsim 10^{19}$ eV and the maximum energy obtained from the Hillas condition comes out to be a few EeV, we consider $E_{\rm p,max} = 10^{19}$ eV in our analysis. This also accounts for the uncertainty in fit parameters arising because electrons lose energy much faster than protons and as a result they are restricted to a smaller region, while protons can travel larger distances without significant energy loss. Thus, the confinement regions of electrons and protons are most likely different. This can result in slightly different blob radii as viewed by electrons and protons. $E_{\rm p,max}$ is less than the threshold of photopion production on CMB, allowing the UHECR protons to travel cosmological distances and interact with EBL relatively close to Earth [209]. Hence, photopion interactions with EBL photons is dominant. Also, the proton injection is modeled to be a simple power law instead of an exponential cutoff power law. This makes no difference as the observed spectrum is not sensitive to the intrinsic source spectrum owing to the dominance of secondary photons from line-of-sight UHECR interactions [231]. However, the choice of the injection spectral index (α) does have significant impact on the secondary neutrino spectrum. The lower energy peak becomes more and more prominent with higher values of α [see, eg., 163].

⊙ The total kinetic power in UHECRs required to explain the VHE spectrum also depends on the redshift of the sources. For higher values of z, the conversion of UHECR energy to γ-ray energy will be higher and the value of $f_{\rm CR}$ will be higher. This will decrease the value of $L_{\rm UHECR}$. Again, with increasing z, the survival rate of UHECRs along the line of sight decreases. The HBLs selected for the study spans over a wide range in redshift and is highest for 1ES 0414+009 ($z = 0.287$). In this case also, the jet power required is less than that of a 10^9 $M_\odot$ SMBH. It is predicted in Ref. [211] that a hard intrinsic TeV spectrum of distant blazars showing no or little attenuation can be attributed to the fact that production of secondary γ-rays, occuring near to the observer compared to the source distance, dominates the observed γ-ray signal at the VHE regime. This justifies the competency of UHECR interaction model, implemented in explaining the very high-energy γ-ray spectra from distant AGNs.

⊙ In modeling the multiwavelength spectrum of blazar SEDs, an equipartition of energy density between magnetic fields and radiating particles is assumed in many studies to reduce the number of free parameters. In our pure-leptonic analysis, the emission region is far from equipartition. The ratio $u'_{\rm e}/u'_{\rm B}$ is very small in our case. The values of the magnetic field considered inside the jet is already low and decreasing them further

to lower u'_B will result in a poor fit for the synchrotron spectrum. A departure from equipartition results in more luminosity requirement than minimum, as is also obtained in Ref. [275]. But this doesn't pose a theoretical difficulty as long as $L_{jet} \lesssim L_{Edd}$, which is true in our case. In lepto-hadronic fits, the VHE emission being dominated by the hadronic component, the values of $(u'_e + u'_p)/u'_B$ are near to equipartition. The range of values obtained are between 16 and 200 and similar to that obtained for photohadronic interactions inside the jet in Ref. [257]. However, the energy density in electrons in the lepto-hadronic case is still low, resulting in low values of u'_e/u'_B. Lowering the magnetic field value further disallows the Hillas condition from achieving the required $E_{p,max}$ value [see 276, for a detailed discussion]. In Ref. [219], a departure from equipartition results from extremely high and dominant values of u'_p due to photohadronic interactions inside the jet.

⊙ The neutrino flux from individual BL Lac objects obtained in our analysis is too low to be detected by currently operating and upcoming future detectors. A stacked flux from all *Fermi*-LAT detected BL Lac objects with a similar UHECR production mechanism that we discussed could be interesting, however. The spectral shape is in accordance with that found in [210]. However, the neutrino flux they obtained for 1ES 0229+200 is many orders of magntude higher than that obtained in our calculations. The reason for this is the low luminosity requirement in UHECRs, as the VHE spectrum is modeled in our analysis using a comparable contribution from leptonic and hadronic counterparts at the peak. This hybrid contribution results in low L_{UHECR} for all the sources we have studied. The flux of secondary neutrinos is inversely proportional to redshift and the scaling is valid as long as the UHECR protons remain within the angular resolution of the detector [211]. Such a pattern is not seen in our results because of different peak VHE γ-ray flux of the sources, resulting in different UHECR luminosity requirements and hence distinct values of L_ν. Given the low maximum proton energy (10 EeV) required in our model, and deflections in the EGMF and GMF, identifying UHECRs coming from individual BL Lac objects we discussed will be difficult.

3.8 Conclusions

The hard intrinsic TeV spectrum of high-energy peaked BL Lac objects (HBLs) showing very less attenuation is an intriguing mystery in astroparticle physics. A fit to the multi-wavelength SEDs of selected HBLs, over a wide redshift range, is obtained by invoking contributions from hadronic channels arising in UHECR interactions on cosmic background photons. The resulting lepto-hadronic spectrum is well equipped to explain the observed SED in the VHE regime, even for the sources at the highest redshift considered in this study. AGN are extremely energetic astrophysical objects that can produce both γ-rays and UHECRs. However, energies beyond 10 EeV are not easily produced inside the jet. Thus, UHECR interactions on EBL dominates during cosmological propagation.

For a substantial contribution from UHECR interactions, the protons must be collimated along the line of sight of the observer. The secondary particles produced from interactions of UHECRs with the EBL photons initiate EM cascades. With detailed modeling of these cascades and their propagation, we have shown that these contributions from UHECRs can fit VHE gamma-ray data beyond the applicability of the leptonic emission from the jets of a number of BL Lac objects.

4

Two-Population Model of UHECR Sources

Identifying the sources of ultrahigh-energy cosmic rays (UHECRs, $E \gtrsim 0.1$ EeV) is one of the outstanding problems in astroparticle physics [36, 37]. Active Galactic Nuclei (AGNs) residing at the centers of nearby radio-galaxies are considered to be a potential candidate source class of UHECR acceleration [25, 133, 277–279]. Studies involving the origin of TeV γ-rays assert blazars as ideal cosmic accelerators [27, 28, 209, 280]. A recent analysis by the Pierre Auger Observatory has found a possible correlation between starburst galaxies and the observed intermediate scale anisotropy in UHECR arrival directions, with a statistical significance of 4σ in contrast to isotropy [281–284]. There are also propositions of other transient high-energy phenomena like gamma-ray bursts (GRBs) [18, 21, 285–288], tidal disruption events (TDEs) of white dwarfs or neutron stars [13–16], as well as, pulsar winds [289, 290] which can reach the energy and flux required to explain the observed UHECR spectrum. Nevertheless, a direct correlation of these known source catalogs, derived from X-ray and γ-ray observations, with an observed UHECR event is yet to be made [291–294]. The different source classes allow an extensively wide range of UHECR parameters to be viable in the acceleration region. UHECRs produce neutrinos and γ-rays on interactions with the cosmic background photons during their propagation over cosmological distances. The current multimessenger data can only constrain UHECR source models and provide hints towards plausible accelerator environments [38, 191], rejecting the possibility of a pure proton composition at the highest energies [78, 154, 189, 190, 197]. Deflections in Galactic and extragalactic magnetic fields pose an additional challenge in the UHECR source identification.

4.1 Background

The Pierre Auger Observatory (PAO) in Malargüe, Argentina [89] and the Telescope Array (TA) experiment in Utah, United States [295] are attaining unprecedented precision in the measurement of UHECR flux, composition, and arrival directions from 0.3 EeV to beyond 100 EeV using their hybrid detection technique [296, 297]. On incidence at the Earth's atmosphere, these energetic UHECR nuclei initiate hadronic cascades which are intercepted by the surface detector (SD), and the simultaneous fluorescence light emitted by the Nitrogen molecules in the atmosphere is observed using the fluorescence detector (FD). This extensive air shower (EAS) triggered by the UHECRs is recorded to measure the maximum shower-depth distribution ($X_{\rm max}$) [298]. However, even with the large event statistics observed by PAO, the mass composition is not as well constrained as the spectrum and anisotropy up to $\sim$ 100 EeV [151]. The first two moments of $X_{\rm max}$, viz., the

mean $\langle X_{\rm max} \rangle$, and its fluctuation from shower-to-shower $\sigma(X_{\rm max})$ serves the purpose of deducing the mass composition. The standard shower propagation codes, eg., CORSIKA [110], CONEX [111], etc., depend on the choice of a hadronic interaction model and photodisintegration cross-section, which are extrapolations of the hadronic physics to the ultrahigh-energy regime. Uncertainties in these models propagate to uncertainties in the reconstruction of the mass-composition of observed events. Lifting the degeneracy in the mass composition will be essential to constrain the source models.

The current LHC-tuned hadronic interaction models viz., SYBILL2.3C [119], EPOS-LHC [115], and QGSJET-II.04 [126] differ in their inherent assumptions and thus lead to different inferences of the mass composition using the same observed data. Current estimates from PAO predict that the relative fraction of protons decreases with increasing energy above $10^{18.3}$ eV for all three models. For the first two models, N dominates at $10^{19.6}$ eV, while for the third model, the entire contribution at the highest energy comes from He. The ankle at $E \approx 10^{18.7}$ eV corresponds to a mixed composition with He dominance and lesser contributions from N and H, except for QGSJET-II.04 which suggests a zero N fraction [150]. The ankle is often inferred as a transition between two or more different populations of sources, leading to a tension between the preference of Galactic or extragalactic nature of the sub-ankle spectrum. Based on the observed anisotropy and light composition, some UHECR models invoke increased photohadronic interactions of UHECRs in the environment surrounding the source. The magnetic field of the surrounding environment can confine the heavier nuclei with energies higher than that corresponding to the ankle, while they undergo photo-disintegration/spallation to produce the light component in the sub-ankle region [198, 299, 300]. This requires only a single class of UHECR sources that accelerate protons and nuclei. However, it is also possible to add a distinct light nuclei population of extragalactic origin that can explain the origin of the sub-ankle spectrum [22, 301, 302]. A purely protonic component, in addition to a Milky Way-like nuclear composition, has also been studied [302]. The proton fraction in the UHECR spectrum for various source models can be constrained through composition studies and compliance to multimessenger data [177, 303].

In this work, first, we perform a combined fit of spectrum and composition data at $E \gtrsim 5 \cdot 10^{18}$ eV measured by PAO [105], to find the best-fit parameters for a single-population of extragalactic UHECR sources injecting a mixed composition of representative elements (^{1}H, ^{4}He, ^{14}N, ^{28}Si, and ^{56}Fe). The best-fit ^{1}H abundance fraction is found to be zero in this case, conceivable within our choice of the photon background model, photodisintegration cross-section, and hadronic interaction model. Next, we show that within the permissible limit of current multimessenger photon and neutrino flux upper limits [103, 162], the addition of a purely protonic (^{1}H) component up to the highest-energy bin can significantly improve the combined fit of spectrum and composition. We consider this component originates from a separate source population than the one ac-

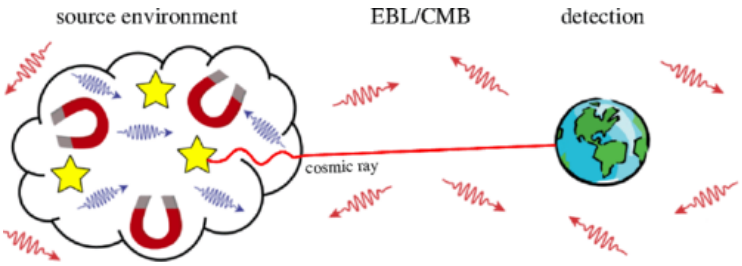

Figure 4.1: Schematic diagram showing the photodisintegration of injected nuclei in the magnetic field and radiation surrounding the source region. The image is taken from Ref. [198].

celerating light-to-heavy nuclei and fit the region of the spectrum above the ankle, i.e., $E \gtrsim 5 \cdot 10^{18}$ eV. The best-fit values of the UHECR parameters are calculated for both the populations, allowing for a one-to-one comparison with the single-population case. We study the effect of variation of the proton injection spectral index, which is not done in earlier studies and indicate the maximum allowed proton fraction at the highest-energy bin up to 3.5σ statistical significance. Lastly, we calculate the fluxes of cosmogenic neutrinos that can be produced by these two populations. We also explore the prospects of their observation by upcoming detectors, and probe the proton fraction at the highest-energy of the UHECR spectrum.

4.2 Extragalactic Origin of Sub-ankle Spectrum

A two-component model has been studied earlier to explain the origin of the sub-ankle spectrum, below 5×10^{18} eV [301]. From recent measurements by PAO, it can be inferred that a steeper injection spectrum ($\alpha \approx 2$) fails to explain the heavy-nuclei dominance at the cutoff. Hence "hard" injection spectrum ($\alpha \approx 1$) is the preferred scenario. But KASCADE-Grande, and also PAO data reveals a light nuclei composition below the ankle, which can be explained by a dominant contribution by H and He [143, 304]. This is found to be in accordance with the injection of a light nuclei component by another population of extragalactic sources. The source emissivity is considered to be 7×10^{49} erg Mpc^{-3}yr^{-1}, with injection spectral index $\alpha = 2.7$ and maximum acceleration energy, $R_{\rm cut} = 3 \times 10^{19}$ eV. The transition from Galactic to extragalactic cosmic rays is pushed to sub-EeV energies.

The entire UHECR spectrum up to the highest energies can also be explained by a single-mass injection, as studied in Ref. [198]. UHECR nuclei can undego increased interactions in the medium surrounding the source. The light component in the sub-ankle region originates from photodisintegration of the injected mass in the magnetic fields and radiations therein. The high-energy heavy nuclei particles escape undissociated, while the low-energy counterparts are trapped having higher escape timescales than interaction timescale. The resultant spectra after this first episode of interactions then propagate through the extragalactic distance to reach Earth (see Fig. 4.1). The injection of a single element ^{28}Si, with spectral index $\alpha = 1$ and a source evolution proportional to the star

formation rate, is found to be the best case scenario. A Milky Way-like mix of nuclear composition abundance is also studied and yields a suitable fit.

In a continuation of the above work, Ref. [302] have considered a pure proton component in addition to the aforementioned populations. The pure proton component is parametrized by the fraction of energy carried by protons relative to the total energy of all cosmic rays, escaping their source at $E > 10^{19}$ eV. In their two-population work, the proton spectral index is fixed to $\gamma_p = 1$ ($dN/dE \propto E^{-\gamma_p}$). In Ref. [303], the authors have proposed an interaction-model independent method to probe the allowed proton fraction for $E_p \gtrsim 30$ EeV, constrained by the cosmogenic neutrino flux upper limits at 1 EeV. Thus, they do not take the composition of primary cosmic rays into account, inferred from air shower data. They have considered a generalized redshift evolution function of the proton injecting sources, parametrized by the evolution index m.

4.3 Analysis Techniques

4.3.1 Simulation setup for UHECR propagation

UHECRs propagate over cosmological distances undergoing a variety of photohadronic interactions. These interactions lead to the production of secondary particles, viz., cosmogenic neutrinos and photons. The dominant photopion production of UHECR protons on the cosmic microwave background (CMB) via $\Delta-$resonance occurs at $\approx 6.8 \times 10^{19}$ eV, producing neutral and charged pions (π^0, π^+) with 2/3 and 1/3 probability, respectively. The neutral pions decay to produce γ-rays ($\pi^0 \rightarrow \gamma\gamma$), while the charged pions decay to produce neutrinos ($\pi^+ \rightarrow \mu^+ + \nu_\mu \rightarrow e^+ + \nu_e + \overline{\nu}_\mu + \nu_\mu$). Neutrinos can also be produced through other $p\gamma$ processes and neutron beta decay ($n \rightarrow p + e^- + \overline{\nu}_e$). Bethe-Heitler interaction of UHECR protons of energy $\approx 4.8 \times 10^{17}$ eV with CMB photons can produce e^+e^- pairs. The e^+ and e^- produced through various channels can iteratively produce high-energy photons by inverse-Compton scattering of cosmic background photons or synchrotron radiation in the extragalactic magnetic field (EGMF). The produced photons can undergo Breit-Wheeler pair production. All these interactions also hold for heavier nuclei ($^A_Z X$, $Z > 1$), in addition to photodisintegration. The interactions may also occur with the extragalactic background light (EBL), having energy higher than the CMB, with cosmic-rays of lower energy. Besides, all particles lose energy due to the adiabatic expansion of the universe. While cosmic rays are deflected by the Galactic and extragalactic magnetic fields, the neutrinos travel unaffected by matter or radiation fields, and undeflected by magnetic fields.

The observed spectrum depends heavily on the choice of injection spectrum. We consider all elements are injected by the sources following the spectrum given by,

$$\frac{dN}{dE} = A_0 \sum_i K_i \left(\frac{E}{E_0}\right)^{-\alpha} f_{\rm cut}(E, ZR_{\rm cut}) \tag{4.1}$$

This represents an exponential cutoff power-law function, where K_i and α are the abun-

dance fraction of elements and spectral index at injection. A_0 and E_0 are arbitrary normalization flux and reference energy, respectively. A similar spectrum has been considered in the combined fit analysis by the PAO [151]. The broken exponential cutoff function is written as,

$$f_{\rm cut} = \begin{cases} 1 & (E \leqslant ZR_{\rm cut}) \\ \exp\left(1 - \dfrac{E}{ZR_{\rm cut}}\right) & (E > ZR_{\rm cut}) \end{cases} \tag{4.2}$$

We use the CRPROPA 3 simulation framework to find the particle yields obtained at Earth after propagating over extragalactic space from the source to the observer [144]. We find the best-fit values of the UHECR parameters α, rigidity cutoff ($R_{\rm cut}$) and K_i for both one-population and two-population models. The normalization depends on the source model and the source population. The spectrum of EBL photons and its evolution with redshift is not as well known as for CMB. We use a latest and updated EBL model by Gilmore *et al.* [170] and TALYS 1.8 photodisintegration cross-section [74].

4.3.2 Shower-depth distribution

We use the parametrizations given by PAO based on the Heitler model of EAS to calculate the mean depth of cosmic-ray air shower maximum $\langle X_{\rm max}\rangle$ and its dispersion from the first two moments of $\ln A$ [305, 306].

$$\langle X_{\rm max}\rangle = \langle X_{\rm max}\rangle_p + f_E\langle \ln A\rangle \tag{4.3}$$

$$\sigma^2(X_{\rm max}) = \langle \sigma^2_{\rm sh}\rangle + f_E^2\sigma^2_{\ln A} \tag{4.4}$$

where $\langle X_{\rm max}\rangle_p$ is the mean maximum depth of proton showers and f_E is a parameter which depends on the energy of the UHECR event,

$$f_E = \xi - \frac{D}{\ln 10} + \delta \log_{10}\left(\frac{E}{E_0}\right) \tag{4.5}$$

where ξ, D, and δ depend on the specific hadronic interaction model. $\sigma^2_{\ln A}$ is the variance of $\ln A$ distribution and $\langle \sigma^2_{\rm sh}\rangle$ is the average variance of $X_{\rm max}$ weighted according to the $\ln A$ distribution,

$$\langle \sigma^2_{\rm sh}\rangle = \sigma^2_p[1 + a\langle \ln A\rangle + b\langle (\ln A)^2\rangle] \tag{4.6}$$

where σ^2_p is the $X_{\rm max}$ variance for proton showers depending on energy and three model-dependent parameters. In this work, we use the updated parameter values[1] obtained from the CONEX simulations [111], for one of the post-LHC hadronic interaction models, SYBILL2.3C.

4.4 One-population Model

We perform a combined fit of our UHECR source models to the spectrum and composition data measured by PAO [150, 152]. We do the analysis for both one-population

[1] S. Petrera and F. Salamida (2018), Pierre Auger Observatory

Table 4.1: UHECR best-fit parameter set for the one-population model

Parameter	**Description**			**Values**	
α	Source spectral index			-0.7	
$\log_{10}(R_{\rm cut}/V)$	Cutoff rigidity			18.2 EV	
$z_{\rm max}$	Cutoff redshift			1.0 (fixed)	
m	Source evolution index			0.0 (fixed)	
$K_i(\%)$	H	He	N	Si	Fe
	0.0	95.6	4.1	0.3	0.0073
$\chi^2_{\rm tot}$/d.o.f	$\chi^2_{\rm spec}$	$\chi^2_{\rm comp}$			
56.19/25	9.94	46.25			

and two-population model of the UHECR sources. The fit region corresponds to energies above the ankle, i.e., $E \gtrsim 5\cdot10^{18}$ eV in the spectrum, as well as, composition. We calculate the goodness-of-fit using the standard χ^2 formalism,

$$\chi^2_j = \sum_{i=1}^{N}\left[\frac{y_i^{\rm obs}(E) - y_i^{\rm mod}(E;a_M)}{\sigma_i}\right]^2 \tag{4.7}$$

where the subscript j corresponds to any of the three observables, viz., spectrum, $X_{\rm max}$, or $\sigma(X_{\rm max})$. To find the best-fit cases, we minimize the sum of all the χ^2_j values. Here $y_i^{\rm obs}(E)$ is the measured value of an observable in the $i-$th energy bin corresponding to a mean energy E and $y_i^{\rm mod}(E;a_M)$ is the value obtained numerically. a_M are the best-fit values of M parameters varied in the simulations. σ_i are the errors provided by PAO. We denote the spectral fit as $\chi^2_{\rm spec}$ and the composition fit as $\chi^2_{\rm comp}$. The latter represents the goodness-of-fit considering $X_{\rm max}$ and $\sigma(X_{\rm max})$ simultaneously.

We start by considering a single population of extragalactic sources up to a redshift $z = 1$, injecting a mixed composition of representative elements ^{1}H, ^{4}He, ^{14}N, ^{28}Si, and ^{56}Fe following an injection spectrum given by Eq. 4.1. The elements are injected with energy between $0.1 - 1000$ EeV. The combined fit analysis done by PAO argues that only particles originating from $z \lesssim 0.5$ are able to reach Earth with $E > 5\cdot10^{18}$ eV [151, 268, 269]. Indeed, in our case, the contribution at the spectral cutoff comes from ^{56}Fe. Hence, the sources which are located further in the distance than $z_{\rm max} = 1$ are unable to contribute to the spectrum above the ankle ($\approx 10^{18.7}$ eV) [see, eg., Appendix C of 153]. This is because, as the distance of such heavy nuclei injecting sources increases, the rate of photodisintegration also gradually increases, thus decreasing their survival rate at the highest energies. Moreover, it was found that increasing $z_{\rm max}$ has no effect on the best-fit parameters found with $z_{\rm max} = 1$ [191]. The source distribution is assumed to be uniform over comoving distance to reduce the number of parameters and hence the complexity of

the problem and time required for simulations.

We scan the parameter space by varying the rigidity cutoff $\log_{10}(R_{\rm cut}/V)$ between [18.0, 18.5] with a grid spacing of 0.1 and the injection spectral index α between [-1.5, 1.0] with a grid spacing of 0.1. For each set of values $\{\alpha, \log_{10}(R_{\rm cut}/V)\}$, we find the best-fit abundance fraction of the injected elements. The number of physical parameters varied is 7 and we consider the normalization to be an additional free parameter. Hence the number of degrees of freedom (d.o.f) is $N_{\rm d} = 33-7-1 = 25$ in this model, since the fitting is done to a total of 33 data points. All the parameter values for the best-fit case of the single-population model are listed in Table 4.1.

We see that the best-fit ^{1}H fraction turns out to be zero, and a non-zero ^{56}Fe component is unavoidable in this case. Indeed from the best-fit spectrum, shown in the upper left panel of Fig. 4.2, the contribution from $Z = 1$ component above $5 \cdot 10^{18}$ eV is infinitesimal. Since the heavier nuclei must come from nearby sources, for them to survive at the highest energies. The maximum rigidity, in this case, suggests that the cutoff in the spectrum originates from maximum acceleration energy at the sources. The fit, however, corresponds to a negative injection spectral index, which is difficult to explain by either the existing particle acceleration models or by sufficient hardening due to photohadronic interactions in the environment surrounding the source. The slope of the simulated $X_{\rm max}$ plot (cf. Fig. 4.2), in comparison to data, suggests that the addition of a light element above 10^{19} eV can improve the fit. Motivated by these aforementioned characteristics of the combined fit, it is impulsive to add the contribution from another source population and check the effects on the spectrum and composition.

4.5 Two-population Model

We consider a discrete extragalactic source population injecting ^{1}H following the spectrum of Eq. 4.1. We refer to this as the Population-I (abbv. Pop-I). This pure-proton component has a distinct rigidity cutoff $R_{\rm cut,1}$, and injection spectral index $\alpha_1 \gtrsim 2$, such that the spectrum extends up to the highest-energy bin of the observed UHECR spectrum. The normalization $A_1 = A_p$ is fixed by the condition $J_p(E_h) = f_{\rm H} J(E_h)$, where $J(E) = dN/dE$ of the observed spectrum and E_h is the mean energy of the highest-energy bin. $f_{\rm H}$ is an additional parameter that takes care of the proton fraction in the highest-energy bin of the UHECR spectrum. Another population (Population-II, abbv. Pop-II) injects light-to-heavy nuclei, viz., ^{4}He, ^{14}N, ^{28}Si, and ^{56}Fe, as we have already seen that for a mixed composition at injection, the contribution of ^{1}H abundance tends to be zero above the ankle energy. Pop-II also follows the spectrum in Eq. 4.1 with rigidity cutoff $R_{\rm cut,2}$ and injection spectral index α_2, and the abundance fraction at injection given by K_i ($\sum_i K_i = 100\%$). The normalization A_2 in this case is a free parameter which is adjusted to fit the spectrum and composition. As in the single-population model, here too, we set the maximum redshift of the sources to $z_{\rm max} = 1$. Athough the anisotropy of UHECR arrival

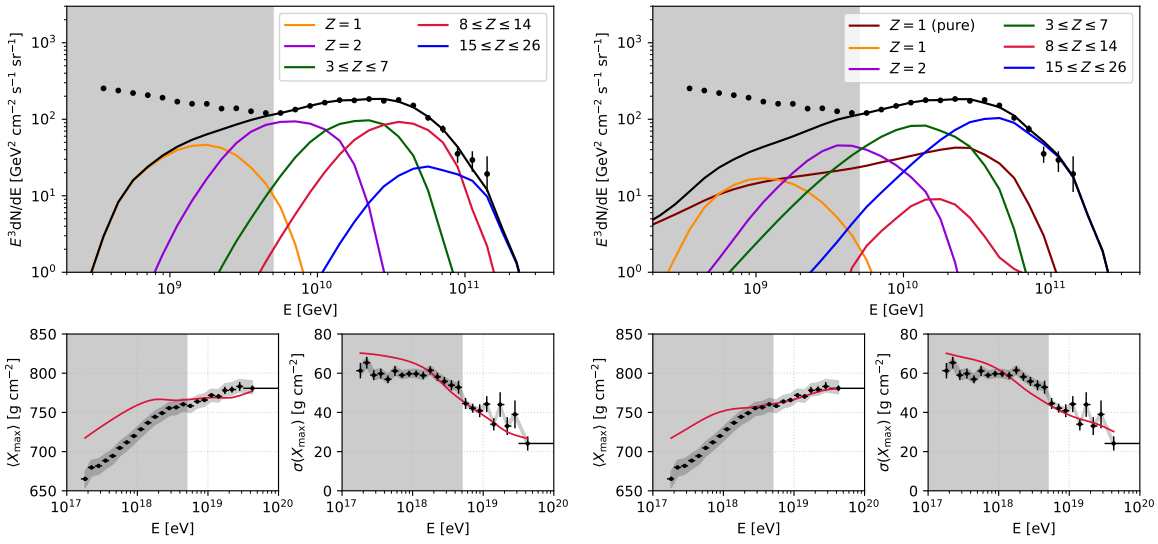

(a) One-population model

(b) Two-population model ($\alpha_1 = 2.2$)

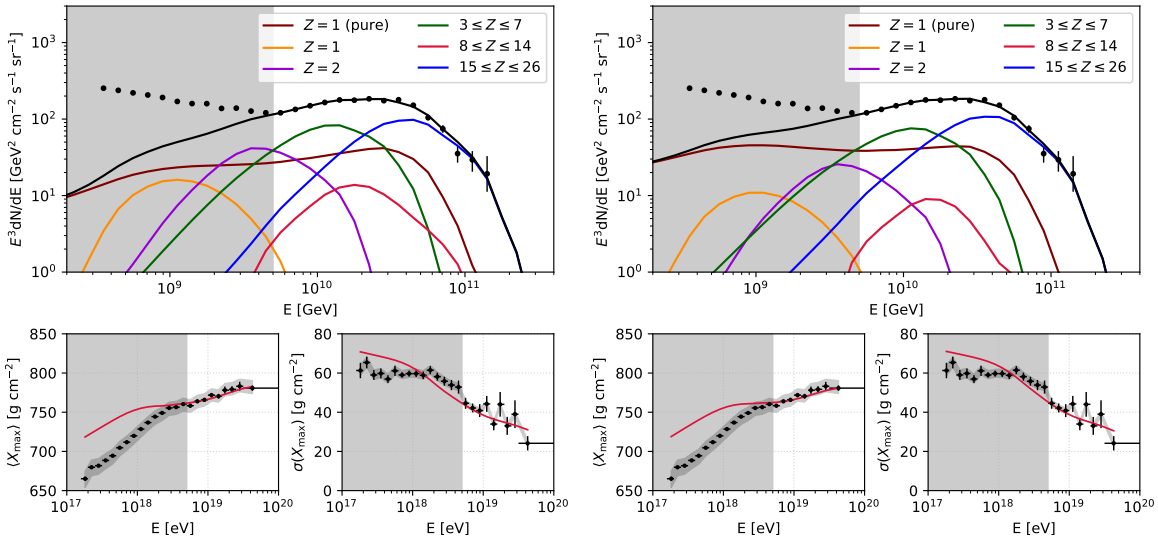

(c) Two-population model ($\alpha_1 = 2.4$)

(d) Two-population model ($\alpha_1 = 2.6$)

Figure 4.2: UHECR spectrum and composition for the best-fit parameters of single-population and two-population models. For the latter case, the resulting spectra for different injection spectral index of the pure-proton component are shown.

directions suggest that the observed spectrum depends on the position distribution of their sources, a definitive source evolution model is difficult to find. The rigidity cutoff and the injection spectral index will vary widely with the variation of evolution function and its exponent. Hence, we consider that both of the source populations are devoid of redshift evolution, i.e., $m = 0$ in the $(1 + z)^m$ type of source evolution models, to enhance computational efficiency. Our motive is to find out the improvement in the simulated $\langle X_{\rm max} \rangle$ to fit the PAO data. It is mentionworthy, that $\langle X_{\rm max} \rangle$ being linear in $\langle \ln A \rangle$, it can measure both pure composition and mixed compositions. However, there is no one-to-one correspondence between the $\sigma(X_{\rm max})$ value and a given mean log mass. Thus,

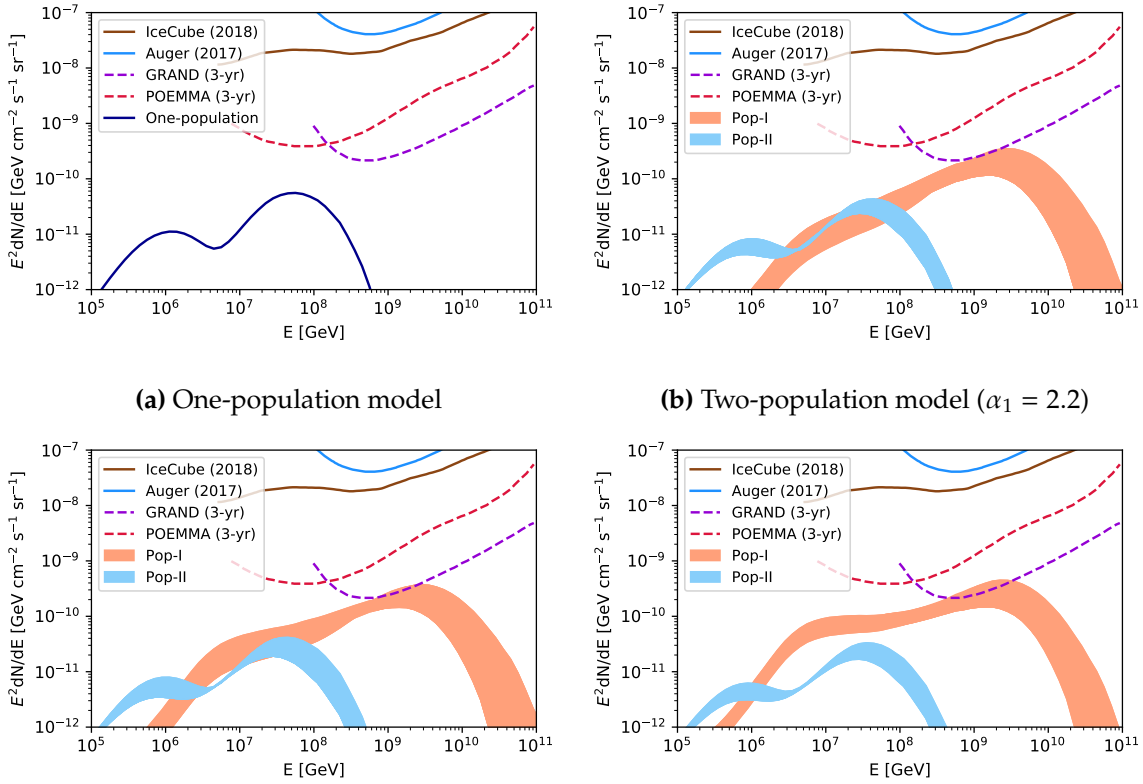

(a) One-population model

(b) Two-population model ($\alpha_1 = 2.2$)

(c) Two-population model ($\alpha_1 = 2.4$)

(d) Two-population model ($\alpha_1 = 2.6$)

Figure 4.3: The all-flavor cosmogenic neutrino fluxes for one-population and two-population models along with the sensitivity of currently operating and future neutrino detectors. The neutrino flux originating from distinct source populations up to $f_{\rm H} = 20.0\%$ are shown for proton injection index $\alpha_1 = 2.2$, 2.4, and 2.6 in the top-right, bottom-left and bottom-right panels.

for a mixed composition the fluctuations in $X_{\rm max}$ can come from the intrinsic shower-to-shower fluctuations, and also from $\ln A$ dispersion due to mass distribution. The mass distribution may arise as a result of propagation effects too [306].

4.5.1 Spectrum and composition fit

The cumulative contribution of Pop-I and Pop-II is used to fit the UHECR spectrum and composition for fixed values of $f_{\rm H}$. We vary $f_{\rm H}$ from $1.0 - 20.0\%$, at intervals of 0.5% between $1.0 - 2.5\%$ and at intervals of 2.5% between $2.5 - 20.0\%$ to save computation time. α_1 is varied through the values 2.2, 2.4, and 2.6, inspired by previous analyses with light elements fitting the UHECR spectrum [163, 194]. We vary $\log_{10}(R_{\rm cut,1}/V)$ between the interval [19.5, 20.2] at grid spacings of 0.1, and $\log_{10}(R_{\rm cut,2}/V)$ between [18.22, 18.36] at grid spacing of 0.02. For each combination of $\{\alpha_1, f_{\rm H}\}$, we find the best-fit values of $\log_{10}(R_{\rm cut,1}/V)$, $\log_{10}(R_{\rm cut,2}/V)$, α_2, and composition K_i at injection of Pop-II; that minimizes the $\chi^2_{\rm tot}$ of the combined fit. Due to increased number of parameters, we set the precision of composition K_i to 0.25%. These parameter sets are listed in Table 4.2. For $\alpha_1 = 2.2$ and 2.4, the $\chi^2_{\rm tot}$ value monotonically increases with $f_{\rm H}$ beyond the best-fit value,

Table 4.2: Best-fits to UHECR spectrum and composition for two-population model. Here the values of $R_{\rm cut,1}$ and $R_{\rm cut,2}$ are in logarithmic units. Cases II, XV, and XXV are presented in Fig. 4.2.

Population - I			**Population - II**						**Goodness-of-fit**			
α_1	$f_{\rm H}(\%)$	$R_{\rm cut,1}$	α_2	$R_{\rm cut,2}$	K_{He}	K_N	K_{Si}	K_{Fe}	$\chi^2_{\rm spec}$	$\chi^2_{\rm comp}$	$\chi^2_{\rm tot}$	ID #
2.2	1.0%	19.5	0.6	18.30	74.75	22.50	2.00	0.75	16.97	23.03	40.00	I
	1.5%	19.5	0.9	18.30	53.00	44.25	0.00	2.75	14.68	15.52	**30.20**	II
	2.0%	19.5	1.2	18.30	41.50	52.50	0.00	6.00	17.03	15.38	32.41	III
	2.5%	19.6	0.6	18.30	73.25	24.25	1.75	0.75	13.86	21.68	35.54	IV
	5.0%	19.7	0.5	18.28	76.50	21.25	1.75	0.50	12.11	25.56	37.67	V
	7.5%	19.8	0.3	18.28	82.25	16.25	1.25	0.25	13.47	28.00	41.47	VI
	10.0%	19.8	0.6	18.28	71.25	26.50	1.50	0.75	14.07	28.74	42.81	VII
	12.5%	19.9	0.3	18.26	82.50	16.00	1.25	0.25	14.28	29.57	43.85	VIII
	15.0%	20.0	0.3	18.28	81.75	16.75	1.25	0.25	16.62	29.31	45.93	IX
	17.5%	20.0	0.3	18.26	82.25	16.25	1.25	0.25	15.85	30.51	46.36	X
	20.0%	20.1	0.3	18.28	81.50	17.00	1.25	0.25	17.65	30.10	47.75	XI
2.4	1.0%	19.5	0.8	18.28	56.75	39.75	1.25	2.25	14.86	20.46	35.32	XII
	1.5%	19.5	1.3	18.30	18.75	70.25	0.00	11.00	21.15	15.48	36.63	XIII
	2.0%	19.6	0.6	18.28	68.75	28.75	1.50	1.00	13.55	21.80	35.35	XIV
	2.5%	19.6	0.9	18.30	45.25	51.00	0.75	3.00	12.60	18.13	**30.73**	XV
	5.0%	19.7	0.8	18.28	54.50	42.25	1.25	2.00	12.13	22.16	34.39	XVI
	7.5%	19.8	0.6	18.28	71.00	26.00	2.25	0.75	12.36	27.10	39.46	XVII
	10.0%	19.9	0.5	18.28	75.75	21.75	2.00	0.50	13.78	28.42	42.20	XVIII
	12.5%	19.9	0.6	18.26	71.50	25.50	2.25	0.75	12.99	30.22	43.21	XIX
	15.0%	20.0	0.5	18.28	74.75	22.75	2.00	0.50	14.93	29.32	44.25	XX
	17.5%	20.1	0.3	18.26	82.00	16.25	1.50	0.25	14.60	30.43	45.03	XXI
	20.0%	20.2	0.3	18.28	80.50	17.75	1.50	0.25	16.40	29.69	46.09	XXII
2.6	1.0%	19.5	1.3	18.30	0.00	84.50	0.00	15.50	21.43	22.86	44.29	XXIII
	1.5%	19.6	0.8	18.30	46.25	49.50	1.75	2.50	14.57	23.97	38.54	XXIV
	2.0%	19.6	1.1	18.30	0.00	91.50	0.00	8.50	12.03	19.63	**31.66**	XXV
	2.5%	19.6	1.3	18.30	0.00	83.50	3.00	13.50	18.18	22.07	40.25	XXVI
	5.0%	19.7	1.3	18.30	0.00	83.75	4.25	12.00	14.36	25.43	39.79	XXVII
	7.5%	19.8	1.1	18.30	0.00	90.75	2.00	7.25	12.27	24.77	37.04	XXVIII
	10.0%	19.9	0.8	18.28	51.00	44.00	3.00	2.00	13.18	26.74	39.92	XXIX
	12.5%	19.9	1.0	18.28	20.00	71.75	3.50	4.75	13.35	29.01	42.36	XXX
	15.0%	20.0	0.8	18.28	49.50	45.50	3.00	2.00	14.69	27.75	42.44	XXXI
	17.5%	20.1	0.6	18.28	61.75	35.00	2.25	1.00	16.88	27.57	44.45	XXXII
	20.0%	20.1	0.7	18.26	62.75	33.00	3.00	1.25	14.25	30.00	44.25	XXXIII

while for α_1=2.6, an alternating behaviour is obtained. The best-fits are found at $f_{\rm H}$ = 1.5%, 2.5%, and 2.0%, respectively for α_1 = 2.2, 2.4, and 2.6. For all the cases, a significant improvement in the combined fit is evident compared to the one-population model. It is worth pointing out that the minimum of $\chi^2_{\rm comp}$ and $\chi^2_{\rm spec}$ do not occur simultaneously and the variation in the best-fit value of $\log_{10}(R_{\rm cut,2}/V)$ is insignificant. In the top right,

bottom left, and bottom right panel of Fig. 4.2, we show the best-fit cases II, XIV, XXV corresponding to α_1 = 2.2, 2.4, and 2.6, respectively. The minimum χ^2 value for all the three cases are comparable and very close to each other, indicating the best-fits are equally good for all the α_1 values considered. The pure-proton component favors higher values of cutoff rigidity than Pop-II and steeper injection spectral index.

4.5.2 Cosmogenic components

It is instructive to compare the all-flavor neutrino fluxes resulting from the two-population model with the current 90% C.L. differential flux upper limits imposed by 9-years of IceCube data [162]. The hard spectral index and lower maximum rigidity in case of one-population model leads to a neutrino spectrum much lower than the current and upcoming future neutrino detectors. This is shown in the top left panel of Fig. 4.3 along with the current sensitivity by PAO [173, 174] and that predicted for 3-years of observation by GRAND [161, 176] and POEMMA [160, 178]. We also present the allowed range of neutrino flux from Pop-I and Pop-II in the two-population model for $f_{\rm H}$ = 1.0 – 20.0%. One can notice that the cosmogenic neutrino flux from Pop-I is within the reach of the proposed GRAND sensitivity. The all-flavor integral limit for GRAND implies an expected detection of $\sim$ 100 neutrino events within 3-years of observation for a flux of $\sim 10^{-8}$ GeV cm^{-2} s^{-1} sr^{-1}. This implies that with a further increase in exposure time, GRAND should be able to constrain our two-population model parameters if $f_H \gtrsim 10\%$.

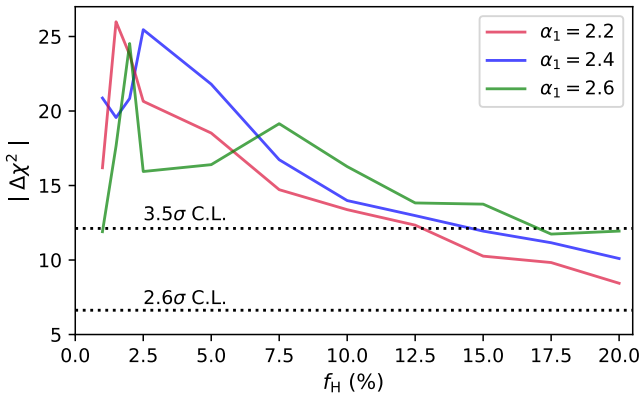

Figure 4.4: $|\Delta\chi^2|$ values between the one-population and two-population model for one d.o.f are shown as a function of the pure-proton fraction $f_{\rm H}$. Three lines correspond to three values of population-I injection spectral index.

As we find the best-fit H fraction is zero in Table-I, $K_{\rm H}$ is a redundant parameter in this case. Scanning the parameter space excluding the latter will result in the same values of the remaining 6 parameters and thus, the resulting model coincides with that of Pop-II in Table-II. Thus, for a $\Delta\chi^2$ calculation between the one-population and two-population model, we consider the number of parameters in the former to be 6 and not 7. The difference in the number of parameters varied between one-population and two-

population model is one, i.e., $R_{\rm cut,1}$. A smooth transition from the two-population model to one-population model can be done by setting $R_{\rm cut,1} = 0$. This necessarily implies that $f_{\rm H} = 0$ and there remains no α_1. Based on the values obtained from,

$$\Delta\chi^2 = \chi^2 \mid_{R_{\rm cut,1}} - \chi^2 \mid_{R_{\rm cut,1}=0} \tag{4.8}$$

we estimate the maximum allowed proton fraction at 3.5σ confidence level (C.L.) in the highest-energy bin. For $\alpha_1 = 2.2$, this corresponds to $\approx 12.5\%$; $\alpha_1 = 2.4$ corresponds to $\approx 15.0\%$; and for $\alpha_1 = 2.6$, it turns out to be $\approx 17.5\%$. However the maximum $\mid \Delta\chi^2 \mid$, which also indicates the most significant improvement in contrast to one-population model, is found for $\alpha_1 = 2.2$, as shown in Fig. 4.4. The 2.6σ and 3.5σ C.L. are also indicated.

4.6 Implications & Discussions

⊙ The composition fit in the one-population model, especially the departure of simulated $\langle X_{\rm max}\rangle$ and $\sigma(X_{\rm max})$ values from the data, leaves a substantial window for improvement. We exploit this possibility in our work by adding a distinct source population injecting ^{1}H that extends up to the highest observed energies. Earlier works have considered a pure-protonic component with an assumed steep injection spectral index [301] or a relatively hard one in addition to a Milky Way-like nuclear composition [302]. Here, we find that a significant improvement in the combined fit to spectrum and composition data is obtained when adding an extragalactic source population emitting UHECRs as protons. For our choice of steep proton injection indices (α_1), the goodness-of-fit is found to be comparable to each other. We also consider the injection index (α_2), maximum rigidity ($R_{\rm cut,2}$), and composition fractions (K_i) of the second population injecting light-to-heavy nuclei to be variables and find the corresponding best-fit values. The corresponding improvement in the combined fit is found to be $\gtrsim 3\sigma$ in some cases.

⊙ Since the variation of each parameter is computationally costly, we consider a flat source evolution to elucidate the importance of a light component directly. In case of one-population model injecting heavy nuclei, a $(1+z)^m$ type of source evolution model prefers $m < 0$ and the injection spectrum is harder than that allowed by the Fermi-acceleration mechanism [38, 191, 193]. In the case of the two-population model, this will allow for various combinations of evolution indices making the analysis complicated. However, with increasing values of $z_{\rm max}$, the variation of m can significantly affect the neutrino spectrum. We have kept the contributing sources within $z \lesssim 1$ in view of the fact that particles originating at higher redshifts will contribute below the ankle, which we do not fit here. Thus within the minimal requirements of this model, our neutrino spectrum can be considered as a conservative lower bound in the two-population scenario.

⊙ The resultant neutrino spectrum in two-population model at $E \gtrsim 0.1$ EeV is dominated by that from pure-protons. Even a small fraction of protons at the highest energy is capable of producing a significant flux of neutrinos. This is expected because of the

maximum energy considered for proton-injecting sources. Even for low $f_{\rm H}$, the values of $E_{\rm max}$ are very close to GZK cutoff energy, where the resonant photopion production occurs, leading to pion-decay neutrinos. The double-humped feature of the neutrino spectrum is a signature of interactions on the CMB and EBL by cosmic rays of different energies. The higher energy peak produced from protons possesses the highest flux, and the detection of these neutrinos at $\sim 3 \cdot 10^{18}$ eV will be a robust test of the presence of a light component at the highest energies, thus also constraining the proton fraction. For $E < 0.1$ EeV, the neutrinos from Pop-II becomes important with peaks at ~ 1 PeV and ~ 40 PeV. Hence, the cumulative neutrino spectrum (Pop-I + Pop-II) exhibits three bumps for $\alpha_1 = 2.2$. But gradually with increasing values of α_1, the lower energy peak of Pop-I becomes significant, diminishing the "three-peak" feature until neutrinos from protons dominate down to ~ 1 PeV for $\alpha_1 = 2.6$

⊙ We present the upper limit on the maximum allowed proton fraction in two-population model at $\approx 1.4 \times 10^{20}$ eV. This is based on the improvement in the combined fit compared to the one-population model, up to 3.5σ statistical significance. For a higher C.L., the proton fraction is even lower at the highest-energy bin. However, a non-zero proton fraction is inevitable. It is studied earlier that the flux of secondary photons increases with an increasing value of α_1 [78]. If a single population injecting protons is used to fit the UHECR spectrum, the resulting cosmogenic photon spectrum saturates the diffuse gamma-ray background at ~ 1 TeV for $\alpha_1 = 2.6$, $m = 0$ [163]. In our two-population model, the proton fraction at the highest energies is much lower than the total observed flux. This ensures the resulting photon spectrum from Pop-I is well within the upper bound imposed by Fermi-LAT [103]. For Pop-II injecting heavier nuclei, the main energy loss process is photodisintegration, contributing only weakly to the cosmogenic photon flux. Hence the two-population model, which we invoke in our study, is in accordance with the current multimessenger data.

⊙ The choice of the hadronic interaction model for our analysis is based on the interpretation of air shower data by the PAO [105, 306]. It is found that QGSJET-II.04 is unsuitable compared to the other two models and leads to inconsistent interpretation of observed data [150]. Also, for our choice of photodisintegration cross-section, i.e. TALYS 1.8, the hadronic model SYBILL2.3C yields superior fits [191]. In general, the SYBILL2.3C model allows for the addition of a higher fraction of heavy nuclei, compared to others, at the highest energies. Indeed in Table 4.2, it is seen that the lowest-χ^2 cases correspond to high $K_{\rm Fe}$, which increases monotonically with α_1. The requirement of Fe abundance in one-population model is much lower than in the case of two-population model. For the latter, the cutoff in the cosmic ray spectrum cannot be solely explained by the maximum acceleration energy of iron nuclei at the sources, but also, must be attributed to photopion production of UHECR protons on the CMB to some extent.

⊙ In going from one-population to the two-population model, the injection spectral

index of the population injecting heavier elements changes from negative to positive, making it easier to accept in the context of various astrophysical source classes. Young neutron stars, eg., can accelerate UHECR nuclei with a flat spectrum, $\alpha_2 \sim 1$ [10]. Particle acceleration in magnetic reconnection sites can also result in such hard spectral indices [see for eg., 307]. AGNs and/or GRBs are probable candidates for pop-I, accelerating protons to ultrahigh energies [285]. The Pop-II injecting light-to-heavy nuclei suggests the sources to be compact objects or massive stars with prolonged evolution history, leading to rich, heavy nuclei abundance in them. The problem in the case of a highly luminous object is, although heavier nuclei may be accelerated in the jet, they interact with ambient matter and radiation density in the environment near the sources [308]. To increase the survivability of UHECR nuclei, less luminous objects such as low-luminosity GRBs (LL GRBs) are preferred [309].

4.7 Conclusions

Based on the spectrum and composition data measured by PAO, a combined fit analysis with a single-population of extragalactic sources suggest that the composition fit at the highest energy deserves improvement. The slope of the simulated $\langle X_{\rm max} \rangle$ curve implies that fitting the highest-energy data points with contribution from ^{56}Fe will diminish the abundance of lighter components ^{28}Si, ^{14}N, and ^{4}He. This will in turn decrease the flux near the ankle region, thus resulting in a bad fit. Addition of another light component of extragalactic origin, preferably pure proton, extending up to the highest-energy bin can resolve this problem. From a critical point of view, this solution is not unique, but definitely a rectifying one. The combined fit improves significantly and we present the maximum allowed proton fraction at the highest-energy bin of spectrum data corresponding to $> 3\sigma$ statistical significance. The UHECR source model studied here is also representative of the various astrophysical candidate classes injecting light-to-heavy elements in diverse abundances. The resulting cosmogenic neutrino spectrum can be detected by future experiments with sufficient exposure and the proton fraction in the highest-energy UHECR data can be tested.

We do not assume any fixed abundance fraction for the light-to-heavy nuclei injecting sources and calculate the best-fit values within the resolution adopted. Also, we consider a flat redshift evolution to reduce the complexity of the problem. Our main aim was to explore if current PAO data allow for a pure-proton flux extending up to the highest-energy bin. We characterize this pure-proton flux arising from typical Fermi acceleration mechanism in luminous astrophysical sources. Our goal is not to explore the parameter regions of such a scenario exhaustively, but to explore a few limited and interesting cases to find the tentatively allowed parameters. Our model can be used to explain cosmogenic neutrino flux, if detected by the current and/or future neutrino detectors, in the context of the current UHECR composition measurements by PAO.

5

Summary & Outlook

The year 2020 marks the end of a decade that witnessed some of the most astonishing observations of the cosmos. These indeed radically transforms our way of understanding the universe at its extreme limits of energy and gravitational acceleration. Predicted in the 1910s by A. Einstein, the long-sought gravitational waves were first detected in 2015 as an aftershock from the distant collision of two black holes [310]. Since then, the ever-intensifying majesty of the LIGO gravitational wave detector [311] has provided further evidence in 2017 of a neutron star merger event [23, 24], also observed by the VIRGO detector [312]. An array of ground-based radio telescopes called Event Horizon Telescope has, for the first time, recreated the image of a supermassive black hole and its shadow in 2019. The SMBH was known to reside at the center of a distant galaxy, Messier 87, in the Virgo cluster. Such energetic events/sources are prominent candidates of ultrahigh-energy cosmic-ray acceleration. On 22 September 2017, IceCube detected a high-energy neutrino-induced muon track [313]. An automated alert was distributed, and several multi-wavelength campaigns by ground-based, as well as space-based telescopes, were done. Simultaneous observations by IceCube and *Fermi*-LAT revealed a neutrino of $E_\nu \sim 0.3$ PeV in spatial coincidence with a γ-ray emitting blazar TXS 0506+056, during an active phase [314]. In 2018, PAO found a correlation between starburst galaxies and the observed intermediate-scale anisotropy of UHECRs, with a statistical significance of 4σ [283]. γ-ray bursts (GRBs) can emit in one second, the amount of energy the Sun will produce in its entire lifetime [315, 316]. For the first time, photons from GRBs with energy extending beyond 100 GeV were reported by Major Atmospheric Gamma Imaging Cherenkov Telescopes (MAGIC) at La Palma, Spain, and the High Energy Stereoscopic System (H.E.S.S.) telescopes in Namibia [317]. TeV photons were detected for 20 minutes from GRB190114C by MAGIC [318, 319], with rapidly diminishing flux, after the burst triggered the SWIFT-BAT and *Fermi*-GBM detectors in space [320]. These remarkable observations uncover several perspectives of the high-energy universe, guiding us to set foot in the uncharted territory of multi-messenger astronomy.

5.1 Impact & Novelty of Research

In this thesis, we try to emphasize the current unknowns of UHECR research. Much has been unveiled in the past decade, from anisotropy observation to the precise measurements of the UHECR spectrum. But, we are yet to reveal the physical process inside astrophysical accelerators that produce UHECRs. As much as 80% of the EGB intensity can be attributed to blazar emission. But neutrinos from them make up only 30%

of the observed astrophysical neutrino flux. While γ-rays can originate from both leptonic and hadronic channels of interaction, neutrinos are produced solely by hadronic processes. Thus neutrinos are the most appropriate messengers of cosmic-ray acceleration/propagation. They are expected to directly point back to their sources because of their weakly interacting nature. We exploit these specific elements of multi-messenger astronomy and the information already obtained, to deduce vital results related to astrophysical aspects of UHECRs.

⊙ In Chapter 2, we show that a light nuclei composition is capable of explaining the UHECR spectrum, while simultaneously satisfying the cosmogenic neutrino flux upper limits from non-observation in 9 years of IceCube operation. A distinction between the abundance fraction of ^{1}H and ^{4}He can be done by identifying the flavor of individual neutrino events. For protons, photopion production is the dominant energy-loss process, producing neutrinos with flavor ratios $\nu_e : \nu_\mu : \nu_\tau = 1 : 2 : 0$. The observed flavor ratio at Earth should be close to $1 : 1 : 1$, by virtue of neutrino oscillations while propagating over extragalactic distances. However, the $\beta-$decay of neutrons can copiously produce electron anti-neutrinos ($\overline{\nu}_e$). The presence of neutrons generated during pion production or, from the nuclei of heavier elements, can shift the constant flavor ratio. The exact energy at which such a departure occurs depends on the composition at injection. For the H+He model, we see the departure occurs at energies less than 10^{17} eV, the precise value of which is determined by the relative He dominance.

The GZK neutrinos, those resulting from the interaction of UHECRs above 6×10^{19} eV with CMB photons, are efficiently produced only by lighter elements, preferably protons. Heavier nuclei lose most of their energy by photodisintegration. In our mixed composition scenario, we find the departure in the constant flux ratio of neutrino flavors occur at around the same energy, i.e., $E < 10^{17}$ eV, but the deviations are much more pronounced. Hence, flavor identification can act as a good discriminator of various composition models at the source. The neutrino flux in the light nuclei case is comparable to the IceCube flux upper limits, and future observation by GRAND can constrain such models. But the presence of heavier elements, up to ^{28}Si pulls down the the neutrino flux below 10^{-12} GeV cm^{-2} s^{-1} sr^{-1}, prior to 1 EeV. The prospects of detection, by currently operating or future neutrino detectors, are bleak. Many studies in recent times have disfavored the UHECR "dip" model. Pure protons explaining the entire UHECR spectrum contradicts the composition measurements by Auger.

It is interesting to note, in the proton dip model, the cutoff in the UHECR spectrum follows from the energy loss through the $\Delta-$resonance channel of photopion production. Although there could be multi-pion production channels too with much lower cross-sections [17, 69], those do not alter the underlying cause of the cutoff. GZK phenomenon has long stood as the explanation to the abrupt end of the observed cosmic ray events. But a fresh debate is ignited by PAO measurements indicating a progressively heavier

composition with increasing energy. Because, if heavier nuclei contribute to the cutoff, they cannot interact with CMB via the $\Delta-$resonance channel. The GZK cutoff is pushed to higher energies, going beyond the observed spectrum for ^{56} Fe nucleus. A solution lies in considering the cutoff is due to maximum acceleration energy at the sources. Why there must exist such maximum energy is yet to be known. The acceleration mechanism inside UHECR sources may be able to provide an answer in the future.

⊙ In Chapter 3, we analyze the feasibility of UHECR production inside extreme energy BL Lacertae (BL Lac) objects. The synchrotron peak in HBLs occurs between UV-to-X-ray frequencies. While the blazar SED is well explained using a synchrotron emission and inverse-Compton (IC) scattering of synchrotron/external photons by electrons, the existence of unattenuated TeV spectrum in HBLs threatens the IC paradigm. Klein-Nishina effect suppresses the efficacy of IC emission by relativistic electrons at high energies ($\Gamma\epsilon_\gamma >> m_e c^2$). The Thomson scattering approximation is no longer valid, and the cross-section becomes dependent on the incident photon energy in the electron rest frame. Hence, IC emission alone is incapable of explaining the very high-energy (VHE) γ-ray signal obtained in several HBLs. If produced, such energetic photons will induce $\gamma\gamma$ pair-production collisions with BLR photons inside the jet, or with EBL photons during extragalactic propagation.

VHE γ-rays can be observed due to UHECR interactions along the line-of-sight of the observer. However, attenuation in the EBL will be significant for photons produced by UHECRs at energies beyond the GZK threshold. Hence, these UHECRs should interact relatively close to Earth with EBL photons, such that a substantial fraction of the produced γ-rays are confined within their propagation direction towards the Earth. While such a scenario is indeed an expected one, distinguishing the photons from hadronic channels is difficult. Differences in arrival times should be resolved for the observed γ-ray signals. Extragalactic propagation of UHECRs also involves the interaction with cosmic magnetic fields. The latter decides the fraction of UHECRs surviving along the line-of-sight. However, the structure of EGMF is not well established, having significant uncertainties on the magnetization at the outskirts of clusters and the filaments in the inter-cluster medium. We consider a random turbulent magnetic field represented by a Kolmogorov power spectrum and the JF12 model of the Galactic magnetic field.

The scenario requires the sources to be placed at distances less than where the majority of UHECRs are deflected from the line-of-sight. The contribution from any source distance will depend on the choice of magnetic field model. The observational constraints on EGMF restrict the allowed range of source distances, from where the electromagnetic cascade initiated by UHECR interactions can have a significant contribution. The UHECR events arriving at Earth will have energy, whatsoever, lower than the GZK threshold. Hence directional correlations cannot be maintained. The different magneto-genesis scenarios of EGMF, in constrained simulations of the local universe, do not affect the anisotropy of

UHECRs. Hence, the anisotropy must originate from the source distribution. Blazars are one assuring class of such astrophysical sources.

⊙ In Chapter 4, we try to improve the composition fit of the observed UHECR spectrum by incorporating additional extragalactic components. Earlier studies have considered an additional light component to explain the UHECR spectrum below the ankle. The predominantly light composition below the ankle can also be explained by the increased photodisintegration/ photohadronic interaction of UHECRs in the region surrounding the source. In both cases, the transition from Galactic to extragalactic cosmic rays are predicted to be near $\sim$ 1 EeV. In our analysis, we add a pure proton component in addition to another population injecting light-to-heavy nuclei. The pure proton component extends up to the highest observed energies. We simultaneously fit the observed $X_{\rm max}$, $\sigma(X_{\rm max})$, and the energy spectrum. The combined fit improves at a significance of $> 3\sigma$ compared to the one-population model.

The UHECR composition becomes progressively heavier beyond $10^{18.2}$ eV. However, the rate of increase in the UHECR mass is not constant but decreases at the highest energies. Hence, the addition of a proton spectrum of extragalactic origin is justified. We have considered the SYBILL2.3C hadronic interaction model for the study, which is a prudent choice, considered in many studies. However, the hadronic interaction models are an extrapolation of cross-sections observed at earth-based accelerators. We do not carry out a rigorous scan of the parameter space to pin down the best-fit value of the Pop-I injection spectral index. The statistical and systematic uncertainties in Auger composition measurements will hinder the accuracy of such an evaluation. The proton injecting sources could be AGN or GRBs. The sources injecting light-to-heavy nuclei must be compact objects or massive stars such as low-luminosity GRBs.

If protons are present at the cutoff of the UHECR spectrum, they will contribute to the GZK neutrinos. A small fraction of protons, at the level of 10%, is sufficient to be detected by future neutrino detectors like GRAND with adequate exposure time. The projected sensitivity is comparable to the neutrino flux from protons. The heavy nuclei injecting sources yield a significantly lesser number of neutrinos, with negligible flux at $\sim$ 1 EeV. Cosmogenic photon flux from UHECR injection with a steep spectral index ($\alpha_1 = 2.6$) saturates the diffuse γ-ray background. The proton abundance is at the level of $< 20\%$ in our study and is thus within flux upper limits imposed by *Fermi*-LAT. It is worth mentioning, the cutoff in the UHECR spectrum arises from two phenomena with relative degrees of dominance, viz., the GZK cutoff due to photopion production of ^{1}H on CMB photons, and also due to maximum acceleration energy at the source for heavier nuclei.

5.2 Multi-messenger Astronomy

The thesis repeatedly emphasizes the importance of multi-messenger observations of astrophysical events, along with multi-wavelength studies. Neutrinos are capable of

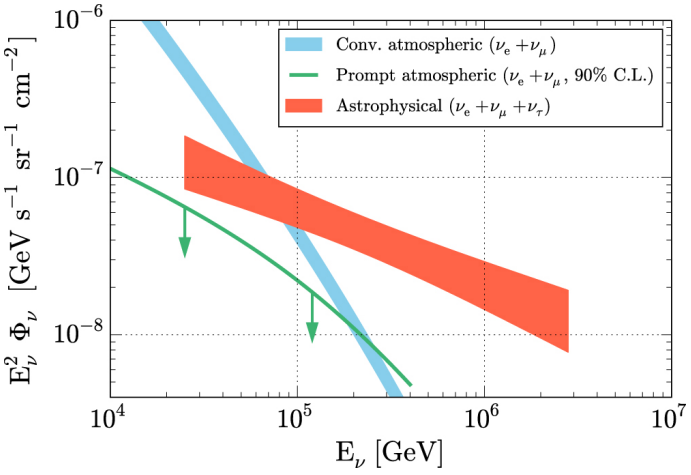

Figure 5.1: The spectrum of astrophysical neutrino flux shows a hardening above the steep atmospheric background. The green line indicates the 90% C.L. upper limit to the expected prompt emission component resulting from the decay of charmed mesons. The image is taken from Ref. [97].

escaping dense and energetic source environments, without interacting. The weakly interacting nature of neutrinos makes them ideal cosmic messengers. Much research has already been devoted to the investigation of expected astrophysical neutrino flux from a variety of source classes. Correlation studies of known γ-ray sources with the neutrino arrival directions are also carried out. Such correlations indicate the relative importance of leptonic to hadronic processes at different luminosities [321, 322]. The only neutrino event which has been correlated at $\sim 3\sigma$ statistical significance with a γ-ray emitting blazar, opens unprecedented avenues to understand cosmic-ray acceleration in blazars. However, recent studies have shown that the high-energy peak can be consistently explained by a leptonic scenario [323]. The neutrino may have come from a radiatively subdominant hadronic component. Hence, ultrahigh-energy cosmic-ray acceleration in TXS 0506+056 is debatable [324, 325]. Another challenge is the direct correlation study of UHECRs with neutrino or γ-rays, because UHECR arrival can be delayed up to $10^4 - 10^5$ years than any simultaneously produced neutrino or γ-ray signals.

About one in a million "track-like" event recorded at IceCube originates from neutrino interaction with ice. A large number of events detected at IceCube comes from muons produced in CR air showers in the Earth's atmosphere. The Earth is used as a filter to distinguish between neutrino-induced and CR-induced muons. The muons which arrive at the IceCube volume (at zenith angles $\gtrsim 85°$) after traversing the Earth/ice must be neutrino-induced because Earth/ice absorbs those originating in hadronic cascades. These are called "upward-going" events, the spectrum of which shows a hardening above the steep atmospheric background, consistent with the astrophysical flux. This is shown in Fig. 5.1. The orange shaded region indicates the 68% C.L. allowed region for astrophysical neutrino flux given by a single power-law model, $\Phi_\nu = \phi(E_\nu/100\ \text{TeV})^{-\gamma}$,

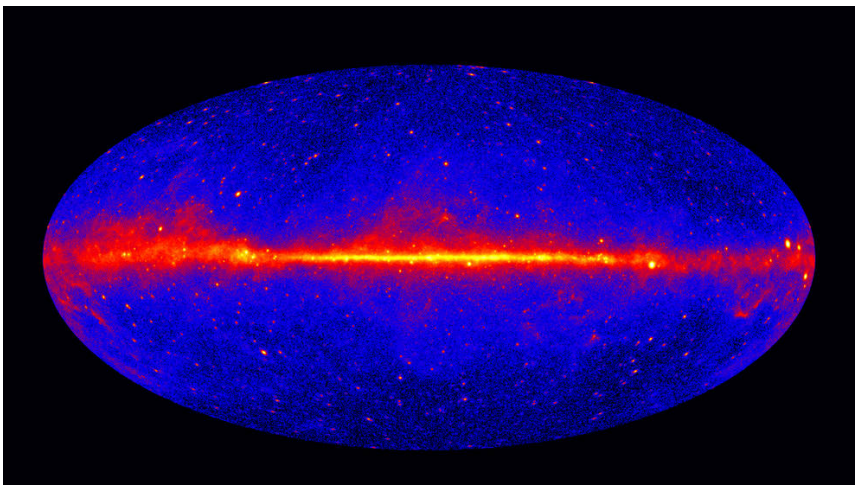

Figure 5.2: The entire gamma-ray sky at energies $E > 1$ Gev from 5 years of *Fermi*-LAT data. The brighter colors indicate brighter gamma-ray sources *(Image Courtesy: NASA/DOE/Fermi-LAT Collaboration).*

assuming neutrinos arrive isotropically at Earth from all directions with a flavor ratio $\nu_e : \nu_\mu : \nu_\tau = 1 : 1 : 1$. Reconstruction of the original neutrino direction can be found with a median angular uncertainty of $< 1^\circ$. The angular resolution of shower-like events is rather poor at about $\sim 15^\circ$. High-energy starting events (HESE) are those for which the neutrino interaction vertex lies within the IceCube detector volume. Such events, recorded in the interval between May 2010 and April 2014, extends to an energy threshold down to $E_\nu \sim 30$ TeV. Three shower-type events were found to have energy $E_\nu > 1$ PeV.

The Pierre Auger Observatory can also detect cosmogenic neutrinos of energy exceeding 100 PeV by employing the surface detectors to observe inclined air showers (zenith angle $> 60^\circ$) that develop deep in the atmosphere [326]. Neutrinos at ultrahigh energies cannot penetrate through Earth. Hence, events with a zenith angle between near horizontal and vertical downgoing are probed. The electromagnetic component of the inclined cosmic-ray showers is attenuated exponentially, and only the muon component reaches ground level. These muons have energies in the range 20–200 GeV and travel several km without decaying, thus having a sharp timing of the shower front [327]. But, neutrinos have an interaction length higher than the matter depth of the atmosphere, at any zenith angle. For inclined neutrinos, the interaction can occur deep inside the atmosphere, and the showers are rich in electrons and photons at the ground level, with broader time spread [328]. Thus cosmic-ray induced showers and neutrino-induced ones are easily distinguished.

The γ-ray emission map obtained from the scan of *Fermi* telescope over the entire sky since 2008 revealed a myriad of non-thermal sources. The map in Fig. 5.2 shows a bright emission component along the Galactic plane and the detection of several other AGNs and GRBs. An overwhelming number of the observed AGNs are blazars. The isotropic diffuse γ-ray background (IGRB) is difficult to distinguish from the Galactic foreground

emission, and precise modeling of the latter is crucial. The foreground introduces a systematic error of $\sim 15-30\%$ on the IGRB intensity [103]. The ground-based telescopes like MAGIC [200], HAWC [202, 203], HESS [199], VERITAS [201], etc., can detect γ-rays from point sources beyond the *Fermi*-LAT threshold. Studies invoking the lepto-hadronic model, and thus prospects of CR acceleration, can be facilitated by the detection of more TeV γ-ray sources. A multi-wavelength campaign employing these various telescopes to hunt for new transient phenomena is capable of shedding light on particle acceleration processes. Some studies have shown that unresolved high-synchrotron peaked BL Lac objects can explain the entire IGRB spectrum beyond 100 GeV. Further observation, new analysis techniques, and future experiments will be able to deduce the composition of IGRB, thus providing better constraints to cosmogenic photons from UHECR interactions. A better sampling of photon data to further constrain the EBL models is also essential.

5.3 Moving Forward

The origin of UHECRs is a long-standing problem in astroparticle physics. Since their discovery, several experiments have been designed to detect their flux and composition. The number of observed events at $E > 5 \times 10^{18}$ eV, i.e., above the ankle, is remarkably lower than that below the ankle. PAO records approximately ~6000 quality hybrid events per year above 10^{18} eV, and roughly 300 per year above 10^{19} eV [89]. For composition measurements, these events must induce air shower up to a depth in the atmosphere contained within the field of view of one of the fluorescence telescopes. The modeling of high-energy astrophysical sources, viz., blazars, starburst galaxies, tidal disruption events, γ-ray bursts, etc., has been done to elucidate on their capability of accelerating UHECRs. Current anisotropy study, using 5514 events above 20 EeV, only points to a weak correlation with extragalactic AGNs and the second catalog of hard *Fermi*-LAT sources. The sky model of cosmic-ray density used in the study parametrizes the fraction of events and the angular scale of clustering around these sources. A sample of starburst galaxies detected by *Fermi*-LAT, however, shows the highest departure from isotropy on an intermediate angular scale, with 4σ statistical significance [283, 329]. The advent of gravitational wave astronomy, allows us to probe some of the most extreme collisions between compact objects. The detection of the merger of two neutron stars triggered the observation of electromagnetic counterparts across all wavebands. The non-detection of neutrinos by PAO in ±500 s time window centered at the merger time of GW 170817 [23, 24], constrains the fluence of UHE neutrinos from such events [330].

UHECRs above the ankle ($E \approx 10^{18.7}$ eV) must originate from nearby sources located at $z \lesssim 0.5$. Otherwise, it is difficult for heavy nuclei to survive photodisintegration and reach Earth. If light elements are present at the highest energies, the primary cosmic rays originate within the GZK sphere, which is $\sim$ 100 Mpc for protons. The latter provides a better correlation of an observed air shower event with point sources, by backtracking

the direction of arrival. Heavy nuclei suffer larger deflections in the magnetic field, and thus, the source position is obscured. However, the evolution of UHECR sources with redshift is not precisely known. A power law evolution of the form $(1+z)^m$ yields satisfactory explanation for the observed spectrum and composition, along with a "hard" injection spectrum and heavy nuclei dominated spectral cutoff. It is difficult to derive the composition in a model-independent manner. Different mass groups appearing at different energies and progressively heavier composition with increasing energy can be caused by the "Peters cycle" [331], whereby rigidity-dependent acceleration at the sources result in a smooth continuity of the observed spectrum. The hadronic interaction models require improvements for obtaining better consistency between $\langle X_{\rm max}\rangle$ and $\sigma(X_{\rm max})$. The magnetic field and their fluctuations in voids and galaxy clusters are difficult to model. γ-ray induced electromagnetic cascade is often used to determine lower limits to the EGMF [332]. Better resolution and sensitivity of γ-ray detectors to point sources can isolate the production channels.

Upgrades to existing experiments and observatories are continually being done to build more improved and sensitive detectors [333]. Any ground-based telescope has an inherent limitation of viewing angle restricted to a part of the sky. The Pierre Auger Observatory and the Telescope Array experiments, being situated at opposite hemispheres, can jointly provide better statistics. The differences in energy scale uncertainty and error estimation pose difficulty in simultaneous analysis of such a combined dataset. Plans are underway to increase the effective TA observatory area by a factor of 4 (TA×4) [334] and thus to bridge the gap between the exposures in two hemispheres. Currently, the fluorescence telescopes at PAO have a duty cycle of $\sim 15\%$, hindering observations of the depth of shower maximum for a significant number of events [335]. Hence, the composition measurement extends only up to 4×10^{19} eV, i.e., the energy beyond which a steep decline in the UHECR flux is observed. The mass composition of the highest-energy UHECR events will point to the possible reason for the cutoff in the cosmic-ray spectrum. It will also differentiate between the energy loss effects during propagation and the maximum energy of injected particles by the sources. Auger aims at achieving sensitivity to the contribution of protons at the level of $\sim 10\%$ in the flux suppression region. This will open up a new course of action to consistently model UHECR sources. The AugerPrime upgrade and the Auger radio upgrade are expected to achieve new heights in UHECR measurements [336]. Analysis of the extensive air showers using hybrid detection techniques holds the potential to reveal new hadronic physics, viz., Lorentz invariance violation, higher dimensions, or exotic particles.

The importance of multi-messenger astronomy can hardly be overestimated. Neutrino and γ-ray observatories are also being improved to achieve state-of-the-art sensitivities. Blazar flares or γ-ray bursts may provide the scope for identification of neutrinos and γ-rays simultaneously from the same event. The IceCube High Energy Array and a

much denser Precision IceCube Next Generation Upgrade (PINGU) subarray, are part of the proposed IceCube-Gen2, a ten-cubic-kilometer detector [156, 337]. The event rate of astrophysical neutrinos is very low relative to the number of tracks recorded. The current angular resolution is $\sim 0.5^\circ$ for muon neutrinos and $\sim 10^\circ$ for electron and tau neutrinos. The Gen2 upgrade will increase the event rates by a factor of $4-10$, depending on the neutrino production channels. And the angular resolution will increase by a factor of approximately three. The Oscillation Research with Cosmics in the Abyss (ORCA) detector of the KM3NeT experiment will provide better statistics in the energy range of $1-20$ GeV [157, 179, 338]. These next-generation telescopes will be able to probe particle physics problems, such as the neutrino mass hierarchy, mixing angles of flavor oscillations, etc. The Giant Radio Array for Neutrino Detection (GRAND) plans to reach an all-flavor integral neutrino flux limit of $\sim 1.5 \times 10^{-10}$ GeV cm^{-2}s^{-1}sr^{-1} above 5×10^{17} eV and a sub-degree angular resolution [176, 339]. The cosmogenic neutrino flux of most UHECR source models will be within the reach of GRAND detector, after a few years of observation. It will also detect UHE cosmic rays and γ-rays exceeding 10^8 GeV. The Cherenkov Telescope Array (CTA) will begin operation on probing γ-rays at energies higher than *Fermi*-LAT, in a few years [340, 341]. It is expected to detect numerous new sources, increasing the number of known γ-ray emitting objects by ten-fold. CTA is likely to detect a large number SNRs in γ-rays and shall probe particle acceleration at PeV energies within the Milky Way.

Analytical and numerical studies of particle acceleration process at extreme energies are also of utmost importance. Predictions of cosmological magnetic fields from simulations, constrained by anisotropy information due to particle propagation, can narrow down the possible UHECR sources. The dynamics and evolution of the most violent events, such as the birth of compact objects, binary merger events involving neutron stars, black holes, etc., require consistent theoretical modeling from the observed electromagnetic and multi-messenger counterparts. The conditions leading to the emission of cosmic rays, neutrinos, and γ-rays can be predicted from analytical and semi-analytical studies of feasible astrophysical environments. Simultaneous observation of UHECRs, high-energy neutrinos, γ-rays, and gravitational waves, from cosmic events, will lead to the first recognition of an astrophysical Zevatron in the future.

———

References

[1] V. S. Beresinsky and G. T. Zatsepin, Phys. Lett. B **28**, 423 (1969).

[2] R. Engel, D. Seckel, and T. Stanev, Phys. Rev. D **64**, 093010 (2001).

[3] R. A. Batista, D. Boncioli, A. di Matteo, A. van Vliet, and D. Walz, J. Cosmol. Astropart. Phys. **10**, 063 (2015).

[4] R. Aloisio, D. Boncioli, A. Grillo, S. Petrera, and F. Salamida, J. Cosmol. Astropart. Phys. **2012**, 007 (2012).

[5] M. Böttcher and C. D. Dermer, Astrophys. J. **711**, 445 (2010).

[6] M. Böttcher, A. Reimer, K. Sweeney, and A. Prakash, Astrophys. J. **768**, 54 (2013).

[7] C. D. Dermer, J. D. Finke, H. Krug, and M. Böttcher, Astrophys. J. **692**, 32 (2009).

[8] A. M. Hillas, Annu. Rev. Astron. Astrophys. **22**, 425 (1984).

[9] E. Fermi, Phys. Rev. **75**, 1169 (1949).

[10] P. Blasi, R. I. Epstein, and A. V. Olinto, Astrophys. J. Lett. **533**, L123 (2000).

[11] H. Kang, D. Ryu, and T. W. Jones, Astrophys. J. **456**, 422 (1996).

[12] V. S. Berezinsky, P. Blasi, and V. S. Ptuskin, Astrophys. J. **487**, 529 (1997).

[13] G. R. Farrar and T. Piran, arXiv e-prints , arXiv:1411.0704 (2014), arXiv:1411.0704 [astro-ph.HE] .

[14] R. Alves Batista and J. Silk, Phys. Rev. D **96**, 103003 (2017).

[15] D. Biehl, D. Boncioli, C. Lunardini, and W. Winter, Sci. Rep. **8**, 10828 (2018).

[16] C. Guépin, K. Kotera, E. Barausse, K. Fang, and K. Murase, Astron. Astrophys. **616**, A179 (2018).

[17] K. Murase and S. Nagataki, Phys. Rev. Lett. **97**, 051101 (2006).

[18] C. D. Dermer and S. Razzaque, Astrophys. J. **724**, 1366 (2010).

[19] N. Gupta and B. Zhang, Mon. Not. R. Astron. Soc. **380**, 78 (2007).

[20] P. Baerwald, M. Bustamante, and W. Winter, Astrophys. J. **768**, 186 (2013).

[21] N. Globus, D. Allard, R. Mochkovitch, and E. Parizot, Mon. Not. R. Astron. Soc. **451**, 751 (2015).

[22] X.-Y. Wang, S. Razzaque, P. Mészáros, and Z.-G. Dai, Phys. Rev. D **76**, 083009 (2007).

[23] B. P. Abbott *et al.* (LIGO Scientific Collaboration and Virgo Collaboration), Phys. Rev. Lett. **119**, 161101 (2017).

[24] B. P. Abbott *et al.*, Astrophys. J. Lett. **848**, L13 (2017).

[25] B. Eichmann, J. P. Rachen, L. Merten, A. van Vliet, and J. Becker Tjus, J. Cosmol. Astropart. Phys. **2018**, 036 (2018).

[26] S. S. Kimura, K. Murase, and B. T. Zhang, Phys. Rev. D **97**, 023026 (2018).

[27] K. Murase, C. D. Dermer, H. Takami, and G. Migliori, Astrophys. J. **749**, 63 (2012).

[28] S. Razzaque, C. D. Dermer, and J. D. Finke, Astrophys. J. **745**, 196 (2012).

[29] S. Das, N. Gupta, and S. Razzaque, Astrophys. J. **889**, 149 (2020).

[30] R. Davis, Phys. Rev. Lett. **12**, 303 (1964).

[31] R. Davis, Prog. Part. Nucl. Phys. **32**, 13 (1994).

[32] R. M. Bionta *et al.*, Phys. Rev. Lett. **58**, 1494 (1987).

[33] K. Hirata *et al.*, Phys. Rev. Lett. **58**, 1490 (1987).

[34] V. F. Hess, Phys. Z. **13**, 1084 (1912).

[35] P. Auger, R. Maze, and T. Grivet-Mayer, Compt. Rend. Hebd. Seances Acad. Sci. **206**, 1721 (1938).

[36] K. Kotera and A. V. Olinto, Annu. Rev. Astron. Astrophys. **49**, 119 (2011).

[37] L. A. Anchordoqui, Phys. Rep. **801**, 1 (2019).

[38] R. Alves Batista, J. Biteau, M. Bustamante, K. Dolag, R. Engel, K. Fang, K.-H. Kampert, D. Kostunin, M. Mostafa, K. Murase, F. Oikonomou, A. V. Olinto, M. I. Panasyuk, G. Sigl, A. M. Taylor, and M. Unger, Front. Astron. Space Sci. **6**, 23 (2019).

[39] J. Linsley and L. Scarsi, Phys. Rev. Lett. **9**, 123 (1962).

[40] G. Sigl, Science **291**, 73 (2001).

[41] R. J. Protheroe, in *Topics in Cosmic-Ray Astrophysics*, Vol. 230, edited by M. A. Duvernois (1999) p. 247.

[42] M. Aartsen *et al.*, Adv. Space Res. **62**, 2902 (2018).

[43] R. Blandford and D. Eichler, Phys. Rep. **154**, 1 (1987).

[44] A. R. Bell, Mon. Not. R. Astron. Soc. **182**, 147 (1978).

[45] R. D. Blandford and J. P. Ostriker, Astrophys. J. Lett. **221**, L29 (1978).

[46] M. Lemoine, G. Pelletier, and B. Revenu, Astrophys. J. Lett. **645**, L129 (2006).

[47] L. Sironi, A. Spitkovsky, and J. Arons, Astrophys. J. **771**, 54 (2013).

[48] Z. Li and E. Waxman, Astrophys. J. **651**, 328 (2006).

[49] Z. Li and X.-H. Zhao, J. Cosmol. Astropart. Phys. **2011**, 008 (2011).

[50] D. Caprioli, Astrophys. J. Lett. **811**, L38 (2015).

[51] P. O. Lagage and C. J. Cesarsky, Astron. Astrophys. **125**, 249 (1983).

[52] J. F. McKenzie and H. J. Voelk, Astron. Astrophys. **116**, 191 (1982).

[53] S. G. Lucek and A. R. Bell, Mon. Not. R. Astron. Soc. **314**, 65 (2000).

[54] A. R. Bell and S. G. Lucek, Mon. Not. R. Astron. Soc. **321**, 433 (2001).

[55] M. A. Malkov and L. O. Drury, Rep. Prog. Phys. **64**, 429 (2001).

[56] E. Amato and P. Blasi, Mon. Not. R. Astron. Soc. **364**, L76 (2005).

[57] L. O. Drury, Rep. Prog. Phys. **46**, 973 (1983).

[58] D. R. Lorimer, Living Rev. Relativ. **11**, 8 (2008).

[59] R. Aloisio, Prog. Theor. Exp. Phys. **2017** (2017), 10.1093/ptep/ptx115, 12A102.

[60] A. Venkatesan, M. Coleman Miller, and A. V. Olinto, Astrophys. J. **484**, 323 (1997).

[61] J. Arons, Astrophys. J. **589**, 871 (2003).

[62] M. Bertaina *et al.* (KASCADE-Grande Collaboration), PoS ICRC, **ICRC2015**, 359 (2016).

[63] K. Andeen and M. Plum (IceCube Collaboration), PoS ICRC, **ICRC2019**, 172 (2019).

[64] R. Alfaro *et al.* (HAWC Collaboration), Phys. Rev. D **96**, 122001 (2017).

[65] D. Ivanov (Telescope Array Collaboration), PoS ICRC, **ICRC2019**, 298 (2019).

[66] V. Verzi (Pierre Auger Collaboration), PoS ICRC, **ICRC2019**, 450 (2019).

[67] R. Aloisio, V. Berezinsky, and A. Gazizov, Astropart. Phys. **39**, 129 (2012).

[68] F. G. Schröder, arXiv e-prints , arXiv:1910.03721 (2019), arXiv:1910.03721 [astro-ph.HE] .

[69] A. Mücke, R. Engel, J. P. Rachen, R. J. Protheroe, and T. Stanev, Comput. Phys. Commun. **124**, 290 (2000), astro-ph/9903478 .

[70] J. L. Puget, F. W. Stecker, and J. H. Bredekamp, Astrophys. J. **205**, 638 (1976).

[71] Allard, D., Parizot, E., Olinto, A. V., Khan, E., and Goriely, S., Astron. Astrophys. **443**, L29 (2005).

[72] R. Aloisio, V. Berezinsky, and S. Grigorieva, Astropart. Phys. **41**, 73 (2013).

[73] R. Aloisio, V. Berezinsky, and S. Grigorieva, Astropart. Phys. **41**, 94 (2013).

[74] A. J. Koning, S. Hilaire, and M. C. Duijvestijn, AIP Conf. Proc. **769**, 1154 (2005).

[75] K. Olive and P. D. Group (Particle Data Group), Chinese Physics C **38**, 090001 (2014).

[76] H. Bethe and W. Heitler, Proc. R. Soc. **146**, 83 (1934).

[77] W. Heitler, *Quantum theory of radiation* (Oxford University Press, London, 1954).

[78] V. Berezinsky, A. Gazizov, M. Kachelrieß, and S. Ostapchenko, Phys. Lett. B **695**, 13 (2011).

[79] S. S. Bulanov, C. B. Schroeder, E. Esarey, and W. P. Leemans, Phys. Rev. A **87**, 062110 (2013).

[80] V. Berezinsky and O. Kalashev, Phys. Rev. D **94**, 023007 (2016).

[81] V. Berezinsky, A. Gazizov, and S. Grigorieva, Phys. Rev. D **74**, 043005 (2006).

[82] R. Aloisio, V. Berezinsky, P. Blasi, A. Gazizov, S. Grigorieva, and B. Hnatyk, Astropart. Phys. **27**, 76 (2007).

[83] R. Aloisio, D. Boncioli, A. di Matteo, A. F. Grillo, S. Petrera, and F. Salamida, J. Cosmol. Astropart. Phys. **10**, 006 (2015).

[84] J. C. Gosse and F. M. Phillips, Quat. Sci. Rev. **20**, 1475 (2001).

[85] D. Góra, Universe **4**, 128 (2018).

[86] A. Letessier-Selvon and T. Stanev, Rev. Mod. Phys. **83**, 907 (2011).

[87] J. Linsley and A. A. Watson, Phys. Rev. Lett. **46**, 459 (1981).

[88] Pierre Auger Collaboration, J. Abraham, *et al.*, Science **318**, 938 (2007).

[89] Pierre Auger Collaboration, Nucl. Instrum. Methods Phys. Res., Sect. A **798**, 172 (2015).

[90] X. Bertou *et al.* (Pierre Auger collaboration), Nucl. Instrum. Methods Phys. Res., Sect. A **568**, 839 (2006).

[91] M. Unger, EPJ Web Conf. **53**, 04009 (2013).

[92] P. Nečesal *et al.* (Pierre Auger collaboration), J. Phys. Conf. Ser. **293**, 012036 (2011).

[93] T. Abu-Zayyad *et al.* (Telescope Array collaboration), Nucl. Instrum. Methods Phys. Res., Sect. A **689**, 87 (2012).

[94] R. U. Abbasi *et al.*, Astrophys. J. **804**, 133 (2015).

[95] A. Achterberg *et al.* (IceCube), Astropart. Phys. **26**, 155 (2006).

[96] M. G. Aartsen *et al.* (IceCube Collaboration), arXiv e-prints , arXiv:1510.05223 (2015), arXiv:1510.05223 [astro-ph.HE] .

[97] M. G. Aartsen *et al.* (IceCube Collaboration), Astrophys. J. **809**, 98 (2015).

[98] M. G. Aartsen *et al.* (IceCube Collaboration), Astrophys. J. **835**, 45 (2017).

[99] K. Kotera, D. Allard, and A. Olinto, J. Cosmol. Astropart. Phys. **2010**, 013 (2010).

[100] M. Ahlers, L. Anchordoqui, M. Gonzalez-Garcia, F. Halzen, and S. Sarkar, Astropart. Phys. **34**, 106 (2010).

[101] K. Murase, Y. Inoue, and C. D. Dermer, Phys. Rev. D **90**, 023007 (2014).

[102] M. Fornasa and M. A. Sánchez-Conde, Phys. Rep. **598**, 1 (2015), the nature of the Diffuse Gamma-Ray Background.

[103] M. Ackermann *et al.* (Fermi-LAT Collaboration), Astrophys. J. **799**, 86 (2015).

[104] P. G. Tinyakov and I. I. Tkachev, Astropart. Phys. **24**, 32 (2005).

[105] A. Aab *et al.* (Pierre Auger collaboration), arXiv e-prints , arXiv:1708.06592 (2017), arXiv:1708.06592 [astro-ph.HE] .

[106] D. Harari, S. Mollerach, and E. Roulet, J. Cosmol. Astropart. Phys. **2006**, 012 (2006).

[107] T. K. Gaisser and A. M. Hillas, in *International Cosmic Ray Conference*, International Cosmic Ray Conference, Vol. 8 (1977) p. 353.

[108] The Telescope Array Collaboration and The Pierre Auger Collaboration, arXiv e-prints , arXiv:1801.01018 (2018), arXiv:1801.01018 [astro-ph.HE] .

[109] T. K. Gaisser, T. Stanev, and S. Tilav, Front. Phys. **8**, 748 (2013).

[110] D. Heck, J. Knapp, J. N. Capdevielle, G. Schatz, and T. Thouw, *CORSIKA: a Monte Carlo code to simulate extensive air showers.* (1998).

[111] T. Pierog, M. K. Alekseeva, T. Bergmann, V. Chernatkin, R. Engel, D. Heck, N. N. Kalmykov, J. Moyon, S. Ostapchenko, T. Thouw, and K. Werner, Nucl. Phys. B Proc. Suppl. **151**, 159 (2006).

[112] F. M. Liu, J. Aichelin, M. Bleicher, and K. Werner, Phys. Rev. C **69**, 054002 (2004).

[113] K. Werner, F.-M. Liu, and T. Pierog, Phys. Rev. C **74**, 044902 (2006).

[114] K. Werner and T. Pierog, AIP Conf. Proc. **928**, 111 (2007).

[115] T. Pierog, I. Karpenko, J. M. Katzy, E. Yatsenko, and K. Werner, Phys. Rev. C **92**, 034906 (2015).

[116] J. Engel, T. K. Gaisser, P. Lipari, and T. Stanev, Phys. Rev. D **46**, 5013 (1992).

[117] R. S. Fletcher, T. K. Gaisser, P. Lipari, and T. Stanev, Phys. Rev. D **50**, 5710 (1994).

[118] E.-J. Ahn, R. Engel, T. K. Gaisser, P. Lipari, and T. Stanev, Phys. Rev. D **80**, 094003 (2009).

[119] F. Riehn, R. Engel, A. Fedynitch, T. K. Gaisser, and T. Stanev, arXiv e-prints , arXiv:1510.00568 (2015), arXiv:1510.00568 [hep-ph] .

[120] R. Engel, F. Riehn, A. Fedynitch, T. K. Gaisser, and T. Stanev, EPJ Web Conf. **145**, 08001 (2017).

[121] A. Fedynitch, F. Riehn, R. Engel, T. K. Gaisser, and T. Stanev, Phys. Rev. D **100**, 103018 (2019).

[122] N. Kalmykov and S. Ostapchenko, Sov. J. Nucl. Phys. **50**, 315 (1989).

[123] N. N. Kalmykov, S. S. Ostapchenko, and A. I. Pavlov, Nuclear Physics B Proceedings Supplements **52**, 17 (1997).

[124] S. Ostapchenko, Phys. Rev. D **74**, 014026 (2006).

[125] S. Ostapchenko, Phys. Lett. B **636**, 40 (2006).

[126] S. Ostapchenko, Phys. Rev. D **83**, 014018 (2011).

[127] Ostapchenko, S., EPJ Web of Conferences **52**, 02001 (2013).

[128] R. Engel, D. Heck, and T. Pierog, Annual Review of Nuclear and Particle Science **61**,

467 (2011).
[129] T. Pierog, in *EPJ Web Conf.*, EPJ Web Conf., Vol. 99 (2015) p. 09002.
[130] A. Aab *et al.* (Pierre Auger collaboration), Astrophys. J. **868**, 4 (2018).
[131] J. Abraham *et al.* (Pierre Auger collaboration), Astropart. Phys. **29**, 188 (2008).
[132] J. D. Bray and A. M. M. Scaife, Astrophys. J. **861**, 3 (2018).
[133] C. D. Dermer, S. Razzaque, J. D. Finke, and A. Atoyan, New J. Phys. **11**, 065016 (2009).
[134] K. Dolag and F. Stasyszyn, Mon. Not. R. Astron. Soc. **398**, 1678 (2009).
[135] F. Miniati and D. F. Martin, Astrophys. J. Suppl. **195**, 5 (2011).
[136] S. Hackstein, F. Vazza, M. Brüggen, G. Sigl, and A. Dundovic, Mon. Not. R. Astron. Soc. **462**, 3660 (2016).
[137] M. S. Pshirkov, P. G. Tinyakov, P. P. Kronberg, and K. J. Newton-McGee, Astrophys. J. **738**, 192 (2011).
[138] R. Jansson and G. R. Farrar, Astrophys. J. **757**, 14 (2012).
[139] R. Jansson and G. R. Farrar, Astrophys. J. Lett. **761**, L11 (2012).
[140] R. U. Abbasi *et al.* (Telescope Array collaboration), Astrophys. J. **790**, L21 (2014).
[141] A. Aab *et al.* (Pierre Auger collaboration), Astrophys. J. **804**, 15 (2015).
[142] A. Aab *et al.* (Pierre Auger collaboration), Science **357**, 1266 (2017).
[143] W. D. Apel *et al.* (KASCADE-Grande Collaboration), Phys. Rev. Lett. **107**, 171104 (2011).
[144] R. Alves Batista, A. Dundovic, M. Erdmann, K.-H. Kampert, D. Kuempel, G. Müller, G. Sigl, A. van Vliet, D. Walz, and T. Winchen, J. Cosmol. Astropart. Phys. **2016**, 038 (2016).
[145] S. Lee, Phys. Rev. D **58**, 043004 (1998).
[146] M. Settimo and M. De Domenico, Astropart. Phys. **62**, 92 (2015).
[147] C. Heiter, D. Kuempel, D. Walz, and M. Erdmann, Astropart. Phys. **102**, 39 (2018).
[148] V. Zabalza, Proc. of International Cosmic Ray Conference 2015 , 922 (2015), 1509.03319 .
[149] J. Hahn, PoS ICRC, **ICRC2015**, 917 (2015).
[150] J. Bellido (Pierre Auger Collaboration), PoS ICRC, **ICRC2017**, 506 (2017).
[151] A. Aab *et al.* (Pierre Auger Collaboration), J. Cosmol. Astropart. Phys. **2017**, 038 (2017).
[152] F. Fenu (Pierre Auger Collaboration), PoS ICRC, **ICRC2017**, 486 (2017).
[153] R. Alves Batista, R. M. de Almeida, B. Lago, and K. Kotera, J. Cosmol. Astropart. Phys. **2019**, 002 (2019).
[154] K. Fang and K. Kotera, Astrophys. J. **832**, L17 (2016).
[155] M. Ageron *et al.* (ANTARES), Nucl. Instrum. Meth. **A656**, 11 (2011).
[156] M. G. Aartsen *et al.* (IceCube-Gen2 Collaboration), arXiv e-prints , arXiv:1412.5106 (2014), arXiv:1412.5106 [astro-ph.HE] .
[157] S. Adrian-Martinez *et al.* (KM3Net Collaboration), J. Phys. **G43**, 084001 (2016).
[158] P. Allison *et al.* (ARA Collaboration), Astropart. Phys. **35**, 457 (2012).
[159] S. W. Barwick *et al.* (ARIANNA Collaboration), Astropart. Phys. **70**, 12 (2015).
[160] A. V. Olinto *et al.*, PoS ICRC, **ICRC2017**, 542 (2017).
[161] O. Martineau-Huynh *et al.* (GRAND Collaboration), EPJ Web Conf., **135**, 02001 (2017).
[162] M. G. Aartsen *et al.* (IceCube Collaboration), Phys. Rev. D **98**, 062003 (2018).
[163] S. Das, S. Razzaque, and N. Gupta, Phys. Rev. D **99**, 083015 (2019).
[164] Aghanim, N. *et al.* (Planck Collaboration), Astron. Astrophys. **594**, A11 (2016).
[165] T. M. Kneiske, T. Bretz, K. Mannheim, and D. H. Hartmann, Astron. Astrophys. **413**, 807 (2004).
[166] F. W. Stecker, M. A. Malkan, and S. T. Scully, Astrophys. J. **648**, 774 (2006).
[167] A. Franceschini, G. Rodighiero, and M. Vaccari, Astron. Astrophys. **487**, 837 (2008).
[168] J. D. Finke, S. Razzaque, and C. D. Dermer, Astrophys. J. **712**, 238 (2010).
[169] A. Domínguez, J. R. Primack, D. J. Rosario, F. Prada, R. C. Gilmore, S. M. Faber, D. C. Koo, R. S. Somerville, M. A. Pérez-Torres, P. Pérez-González, J. S. Huang, M. Davis, P. Guhathakurta, P. Barmby, C. J. Conselice, M. Lozano, J. A. Newman, and M. C. Cooper, Mon. Not. R. Astron. Soc. **410**, 2556 (2011).

[170] R. C. Gilmore, R. S. Somerville, J. R. Primack, and A. Domínguez, Mon. Not. R. Astron. Soc **422**, 3189 (2012).
[171] F. W. Stecker, S. T. Scully, and M. A. Malkan, Astrophys. J. **827**, 6 (2016).
[172] N. M. Gerasimova and I. L. Rozental, Sov. Phys. JETP **41**, 488 (1961).
[173] A. Aab *et al.* (Pierre Auger Collaboration), Phys. Rev. D **91**, 092008 (2015).
[174] E. Zas (Pierre Auger Collaboration), PoS ICRC, **ICRC2017**, 972 (2017).
[175] M. G. Aartsen *et al.* (IceCube Collaboration), Phys. Rev. Lett. **117**, 241101 (2016).
[176] K. Fang *et al.*, PoS ICRC, **ICRC2017**, 996 (2017).
[177] K. Møller, P. B. Denton, and I. Tamborra, J. Cosmol. Astropart. Phys. **2019**, 047 (2019).
[178] J. Adams *et al.*, ArXiv e-prints (2017), arXiv:1703.04513 [astro-ph.HE] .
[179] S. Aiello *et al.* (KM3NeT Collaboration), Astropart. Phys. **111**, 100 (2019).
[180] M. Ageron *et al.* (KM3NeT Collaboration), Eur. Phys. J. C **80**, 99 (2020).
[181] K. Murase and J. F. Beacom, Phys. Rev. D **82**, 043008 (2010).
[182] F. W. Stecker, Phys. Rev. **180**, 1264 (1969).
[183] F. W. Stecker and M. H. Salamon, Astrophys. J. **512**, 521 (1999).
[184] L. A. Anchordoqui, J. F. Beacom, H. Goldberg, S. Palomares-Ruiz, and T. J. Weiler, Phys. Rev. D **75**, 063001 (2007).
[185] F. Capozzi, E. Di Valentino, E. Lisi, A. Marrone, A. Melchiorri, and A. Palazzo, Phys. Rev. **D95**, 096014 (2017).
[186] J. G. Learned and S. Pakvasa, Astropart. Phys. **3**, 267 (1995).
[187] J. F. Beacom, N. F. Bell, D. Hooper, S. Pakvasa, and T. J. Weiler, Phys. Rev. **D68**, 093005 (2003), [Erratum: Phys. Rev.D72,019901(2005)].
[188] T. DeYoung, S. Razzaque, and D. F. Cowen, Astropart. Phys. **27**, 238 (2007).
[189] G. B. Gelmini, O. Kalashev, and D. V. Semikoz, J. Cosmol. Astropart. Phys. **2012**, 044 (2012).
[190] A. D. Supanitsky, Phys. Rev. D **94**, 063002 (2016).
[191] J. Heinze, A. Fedynitch, D. Boncioli, and W. Winter, Astrophys. J. **873**, 88 (2019).
[192] Biehl, Daniel, Boncioli, Denise, Fedynitch, Anatoli, Morejon, Leonel, and Winter, Walter, EPJ Web Conf. **208**, 04002 (2019).
[193] A. M. Taylor, M. Ahlers, and D. Hooper, Phys. Rev. D **92**, 063011 (2015).
[194] R. Aloisio and V. Berezinsky, J. Exp. Theor. Phys. **128**, 52 (2019).
[195] A. Aab *et al.* (Pierre Auger Collaboration), Phys. Rev. D **90**, 122006 (2014).
[196] I. S. Karpikov, G. I. Rubtsov, and Y. V. Zhezher, Phys. Rev. D **98**, 103002 (2018).
[197] J. Heinze, D. Boncioli, M. Bustamante, and W. Winter, Astrophys. J. **825**, 122 (2016).
[198] M. Unger, G. R. Farrar, and L. A. Anchordoqui, Phys. Rev. D **92**, 123001 (2015).
[199] F. Aharonian *et al.*, Nature **440**, 1018 (2006).
[200] V. A. Acciari *et al.*, Mon. Not. R. Astron. Soc. **486**, 4233 (2019).
[201] A. Archer *et al.* (VERITAS Collaboration), Phys. Rev. D **98**, 062004 (2018).
[202] A. U. Abeysekara *et al.*, Astrophys. J. **843**, 116 (2017).
[203] A. U. Abeysekara *et al.*, Astrophys. J. **843**, 40 (2017).
[204] C. M. Urry and P. Padovani, Publ. Astron. Soc. Pac **107**, 803 (1995).
[205] G. Fossati, L. Maraschi, A. Celotti, A. Comastri, and G. Ghisellini, Mon. Not. R. Astron. Soc. **299**, 433 (1998).
[206] M. Böttcher and M. G. Baring, Astrophys. J. **887**, 133 (2019).
[207] F. A. Aharonian, Mon. Not. R. Astron. Soc. **332**, 215 (2002).
[208] A. A. Zdziarski and M. Böttcher, Mon. Not. R. Astron. Soc. **450**, L21 (2015).
[209] W. Essey and A. Kusenko, Astropart. Phys. **33**, 81 (2010).
[210] W. Essey, O. E. Kalashev, A. Kusenko, and J. F. Beacom, Phys. Rev. Lett. **104**, 141102 (2010).
[211] W. Essey, O. Kalashev, A. Kusenko, and J. F. Beacom, Astrophys. J. **731**, 51 (2011).
[212] O. E. Kalashev, A. Kusenko, and W. Essey, Phys. Rev. Lett. **111**, 041103 (2013).
[213] A. D. Supanitsky and V. de Souza, J. Cosmol. Astropart. Phys. **2013**, 023 (2013).
[214] H. Takami, K. Murase, and C. D. Dermer, Astrophys. J. Lett. **771**, L32 (2013).
[215] F. Tavecchio, Mon. Not. R. Astron. Soc. **438**, 3255 (2014).

[216] S. Abdollahi *et al.* (Fermi-LAT collaboration), Astrophys. J. Suppl. **247**, 33 (2020).
[217] M. Ajello *et al.* (Fermi-LAT collaboration), Astrophys. J. **892**, 105 (2020).
[218] S. Sahu, B. Zhang, and N. Fraija, Phys. Rev. D **85**, 043012 (2012).
[219] M. Petropoulou and A. Mastichiadis, Mon. Not. R. Astron. Soc **447**, 36 (2015).
[220] S. Sahu, C. E. López Fortín, and S. Nagataki, Astrophys. J. Lett. **884**, L17 (2019).
[221] R. Xue, R.-Y. Liu, X.-Y. Wang, H. Yan, and M. Böttcher, Astrophys. J. **871**, 81 (2019).
[222] M. Böttcher and P. Els, Astrophys. J. **821**, 102 (2016).
[223] K. Murase, F. Oikonomou, and M. Petropoulou, Astrophys. J. **865**, 124 (2018).
[224] J. Hahn, PoS ICRC, **ICRC2015**, 917 (2015).
[225] A. Celotti and G. Ghisellini, Mon. Not. R. Astron. Soc. **385**, 283 (2008).
[226] V. S. Berezinskii and S. I. Grigor'eva, Astron. Astrophys. **199**, 1 (1988).
[227] M. J. Chodorowski, A. A. Zdziarski, and M. Sikora, Astrophys. J. **400**, 181 (1992).
[228] G. Ghisellini, P. Padovani, A. Celotti, and L. Maraschi, Astrophys. J. **407**, 65 (1993).
[229] J. C. Joshi and N. Gupta, Phys. Rev. D **87**, 023002 (2013).
[230] A. Neronov and I. Vovk, Science **328**, 73 (2010).
[231] W. Essey, S. Ando, and A. Kusenko, Astropart. Phys. **35**, 135 (2011).
[232] A. B. Pushkarev, Y. Y. Kovalev, M. L. Lister, and T. Savolainen, Astron. Astrophys. **507**, L33 (2009).
[233] J. D. Finke, Astrophys. J. **870**, 28 (2019).
[234] S. Razzaque, C. D. Dermer, and J. D. Finke, Astrophys. J. **697**, 483 (2009).
[235] R. Falomo, N. Carangelo, and A. Treves, Mon. Not. R. Astron. Soc. **343**, 505 (2003).
[236] P. Padovani and P. Giommi, Astrophys. J. **444**, 567 (1995).
[237] M. L. Ahnen *et al.*, Mon. Not. R. Astron. Soc. **459**, 2286 (2016).
[238] J. Albert *et al.*, Astrophys. J. **667**, L21 (2007).
[239] F. Acero *et al.* (Fermi-LAT Collaboration), Astrophys. J. Suppl. **218**, 23 (2015).
[240] A. A. Abdo *et al.*, Astrophys. J. **716**, 30 (2010).
[241] S. Sahu, A. R. de León, and L. S. Miranda, Eur. Phys. J. C **77**, 741 (2017).
[242] J.-H. Woo, C. M. Urry, R. P. van der Marel, P. Lira, and J. Maza, Astrophys. J. **631**, 762 (2005).
[243] L. Costamante, G. Bonnoli, F. Tavecchio, G. Ghisellini, G. Tagliaferri, and D. Khangulyan, Mon. Not. R. Astron. Soc. **477**, 4257 (2018).
[244] S. Kaufmann, S. J. Wagner, O. Tibolla, and M. Hauser, Astron. Astrophys. **534**, A130 (2011).
[245] F. Aharonian *et al.*, Astron. Astrophys. **475**, L9 (2007).
[246] P. Giommi, S. G. Ansari, and A. Micol, Astron. & Astrophys. Suppl. Ser. **109**, 267 (1995).
[247] F. Tavecchio, G. Ghisellini, L. Foschini, G. Bonnoli, G. Ghirlanda, and P. Coppi, Mon. Not. R. Astron. Soc. Lett. **406**, L70 (2010).
[248] S. Razzaque, P. Meszaros, and B. Zhang, Astrophys. J. **613**, 1072 (2004).
[249] M. Ackermann *et al.*, Astrophys. J. **765**, 54 (2013).
[250] A. Abramowski *et al.* (H. E. S. S. Collaboration), Astron. Astrophys. **562**, A145 (2014).
[251] M. Cerruti, arXiv e-prints , arXiv:1307.8091 (2013), arXiv:1307.8091 [astro-ph.HE] .
[252] E. Aliu *et al.*, Astrophys. J. **782**, 13 (2014).
[253] D. Maccagni, M. Tarenghi, B. A. Cooke, T. Maccacaro, J. P. Pye, M. J. Ricketts, and G. Chincarini, Astron. Astrophys. **62**, 127 (1978).
[254] I. M. McHardy, A. Lawrence, J. P. Pye, and K. A. Pounds, Mon. Not. R. Astron. Soc. **197**, 893 (1981).
[255] D. A. H. Buckley, I. R. Tuohy, and R. A. Remillard, Proceedings of the Astronomical Society of Australia **6**, 147 (1985).
[256] R. A. Remillard, I. R. Tuohy, R. J. V. Brissenden, D. A. H. Buckley, D. A. Schwartz, E. D. Feigelson, and S. Tapia, Astrophys. J. **345**, 140 (1989).
[257] M. Cerruti, A. Zech, C. Boisson, and S. Inoue, Mon. Not. R. Astron. Soc. **448**, 910 (2015).
[258] F. Aharonian *et al.*, Astron. Astrophys. **470**, 475 (2007).
[259] J. P. Halpern, V. S. Chen, G. M. Made-

jski, and G. A. Chanan, Astron. J. **101**, 818 (1991).
[260] H. Gursky, H. Bradt, R. Doxsey, D. Schwartz, J. Schwarz, R. Dower, G. Fabbiano, R. E. Griffiths, M. Johnston, R. Leach, A. Ramsey, and G. Spada, Astrophys. J. **223**, 973 (1978).
[261] A. Abramowski *et al.* (H.E.S.S. Collaboration), Astron. Astrophys. **538**, A103 (2012).
[262] E. Aliu *et al.*, Astrophys. J. **755**, 118 (2012).
[263] M. Petropoulou, S. Dimitrakoudis, P. Padovani, A. Mastichiadis, and E. Resconi, Mon. Not. R. Astron. Soc. **448**, 2412 (2015).
[264] S. R. Kelner and F. A. Aharonian, Phys. Rev. D **78**, 034013 (2008).
[265] C. D. Dermer and G. Menon, *High energy radiation from black holes: gamma rays, cosmic rays, and neutrinos*, Princeton series in astrophysics (Princeton Univ. Press, Princeton, NJ, 2009).
[266] N. Fraija, E. Aguilar-Ruiz, A. Galván-Gámez, A. Marinelli, and J. A. de Diego, Mon. Not. R. Astron. Soc **481**, 4461 (2018).
[267] P. Sommers, Astropart. Phys. **14**, 271 (2001).
[268] K. Greisen, Phys. Rev. Lett. **16**, 748 (1966).
[269] G. T. Zatsepin and V. A. Kuzmin, JETP Lett. **4**, 78 (1966), [Pisma Zh. Eksp. Teor. Fiz.4,114(1966)].
[270] R. Prince, N. Gupta, and K. Nalewajko, Astrophys. J. **883**, 137 (2019).
[271] R. Xue, R.-Y. Liu, M. Petropoulou, F. Oikonomou, Z.-R. Wang, K. Wang, and X.-Y. Wang, Astrophys. J. **886**, 23 (2019).
[272] M. Petropoulou and A. Mastichiadis, Mon. Not. R. Astron. Soc. **426**, 462 (2012).
[273] K. Mannheim and P. L. Biermann, Astron. Astrophys. **253**, L21 (1992).
[274] A. Mücke, R. J. Protheroe, R. Engel, J. P. Rachen, and T. Stanev, Astropart. Phys. **18**, 593 (2003).
[275] M. Zacharias and S. J. Wagner, Astron. Astrophys. **588**, A110 (2016).
[276] P. P. Basumallick and N. Gupta, Astrophys. J. **844**, 58 (2017).
[277] J. P. Rachen and P. L. Biermann, Astron. Astrophys. **272**, 161 (1993).
[278] J. P. Rachen, T. Stanev, and P. L. Biermann, Astron. Astrophys. **273**, 377 (1993).
[279] X. Wang and A. Loeb, Phys. Rev. D **95**, 063007 (2017).
[280] E. Resconi, S. Coenders, P. Padovani, P. Giommi, and L. Caccianiga, Mon. Not. R. Astron. Soc. **468**, 597 (2017).
[281] L. A. Anchordoqui, G. E. Romero, and J. A. Combi, Phys. Rev. D **60**, 103001 (1999).
[282] R. Attallah and D. Bouchachi, Mon. Not. R. Astron. Soc. **478**, 800 (2018).
[283] A. Aab *et al.* (Pierre Auger Collaboration), Astrophys. J. Lett. **853**, L29 (2018).
[284] L. A. Anchordoqui, Phys. Rev. D **97**, 063010 (2018).
[285] E. Waxman, Phys. Rev. Lett. **75**, 386 (1995).
[286] M. Vietri, Astrophys. J. **453**, 883 (1995).
[287] D. Biehl, D. Boncioli, A. Fedynitch, and W. Winter, Astron. Astrophys. **611**, A101 (2018).
[288] B. T. Zhang, K. Murase, S. S. Kimura, S. Horiuchi, and P. Mészáros, Phys. Rev. D **97**, 083010 (2018).
[289] M. Lemoine, K. Kotera, and J. Pétri, J. Cosmol. Astropart. Phys. **2015**, 016 (2015).
[290] K. Kotera, E. Amato, and P. Blasi, J. Cosmol. Astropart. Phys. **2015**, 026 (2015).
[291] J. W. Elbert and P. Sommers, Astrophys. J. **441**, 151 (1995).
[292] G. R. Farrar and P. L. Biermann, Phys. Rev. Lett. **81**, 3579 (1998).
[293] A. Virmani, S. Bhattacharya, P. Jain, S. Razzaque, J. P. Ralston, and D. W. Mckay, Astropart. Phys. **17**, 489 (2002).
[294] D. S. Gorbunov, P. G. Tinyakov, I. I. Tkachev, and S. V. Troitsky, J. Exp. Theor. Phys. Lett. **80**, 145 (2004).
[295] R. Abbasi *et al.*, Astropart. Phys. **80**, 131 (2016).
[296] A. Aab *et al.* (Pierre Auger Collaboration), Phys. Rev. D **96**, 122003 (2017).
[297] R. U. Abbasi *et al.* (Telescope Array Collaboration), Astrophys. J. **862**, 91 (2018).
[298] R. U. Abbasi *et al.* (Telescope Array Collaboration), Astrophys. J. **858**, 76 (2018).
[299] M. Kachelrieß, O. Kalashev, S. Ostapchenko, and D. V. Semikoz, Phys. Rev. D **96**, 083006 (2017).
[300] A. D. Supanitsky, A. Cobos, and A. Etchegoyen, Phys. Rev. D **98**, 103016 (2018).
[301] R. Aloisio, V. Berezinsky, and P. Blasi, J.

Cosmol. Astropart. Phys. **2014**, 020 (2014).
[302] M. S. Muzio, M. Unger, and G. R. Farrar, Phys. Rev. D **100**, 103008 (2019).
[303] A. van Vliet, R. A. Batista, and J. R. Hörandel, Phys. Rev. D **100**, 021302 (2019).
[304] W. D. Apel *et al.* (KASCADE-Grande Collaboration), Phys. Rev. D **87**, 081101 (2013).
[305] J. Matthews, Astropart. Phys. **22**, 387 (2005).
[306] Pierre Auger Collaboration, J. Cosmol. Astropart. Phys. **2013**, 026 (2013).
[307] G. Kowal, E. M. de Gouveia Dal Pino, and A. Lazarian, Astrophys. J. **735**, 102 (2011).
[308] X.-Y. Wang, S. Razzaque, and P. Mészáros, Astrophys. J. **677**, 432 (2008).
[309] K. Murase, K. Ioka, S. Nagataki, and T. Nakamura, Phys. Rev. D **78**, 023005 (2008).
[310] B. P. Abbott *et al.* (LIGO Scientific Collaboration and Virgo Collaboration), Phys. Rev. Lett. **116**, 061102 (2016).
[311] J. Aasi *et al.* (LIGO Collaboration), Classical Quant. Grav. **32**, 115012 (2015).
[312] F. Acernese *et al.*, Classical Quant. Grav. **32**, 024001 (2015).
[313] M. G. Aartsen *et al.* (IceCube Collaboration), Science **361**, 147 (2018).
[314] IceCube Collaboration *et al.*, Science **361**, eaat1378 (2018).
[315] P. Kumar and B. Zhang, Phys. Rep. **561**, 1 (2015).
[316] X.-Y. Wang, R.-Y. Liu, H.-M. Zhang, S.-Q. Xi, and B. Zhang, Astrophys. J. **884**, 117 (2019).
[317] H. Abdalla *et al.*, Nature **575**, 464 (2019).
[318] V. A. o. Acciari (MAGIC Collaboration), Nature **575**, 459 (2019).
[319] V. A. Acciari *et al.* (MAGIC Collaboration), Nature **575**, 455 (2019).
[320] M. Ajello *et al.*, Astrophys. J. **890**, 9 (2020).
[321] P. Mészáros, D. B. Fox, C. Hanna, and K. Murase, Nature Rev. Phys. **1**, 585 (2019).
[322] K. Murase and I. Bartos, Ann. Rev. Nucl. Part. Sci. **69**, 477 (2019).
[323] A. Keivani, K. Murase, M. Petropoulou, D. B. Fox, S. B. Cenko, S. Chaty, A. Coleiro, J. J. DeLaunay, S. Dimitrakoudis, P. A. Evans, J. A. Kennea, F. E. Marshall, A. Mastichiadis, J. P. Osborne, M. Santander, A. Tohuvavohu, and C. F. Turley, Astrophys. J. **864**, 84 (2018).
[324] R.-Y. Liu, K. Wang, R. Xue, A. M. Taylor, X.-Y. Wang, Z. Li, and H. Yan, Phys. Rev. D **99**, 063008 (2019).
[325] A. Reimer, M. Böttcher, and S. Buson, Astrophys. J. **881**, 46 (2019).
[326] K. Capelle, J. Cronin, G. Parente, and E. Zas, Astropart. Phys. **8**, 321 (1998).
[327] A. Aab *et al.* (Pierre Auger collaboration), J. Cosmol. Astropart. Phys. **2014**, 019 (2014).
[328] A. Aab *et al.* (Pierre Auger collaboration), J. Cosmol. Astropart. Phys. **2019**, 022 (2019).
[329] F.-K. Peng, H.-M. Zhang, X.-Y. Wang, J.-F. Wang, and Q.-J. Zhi, Astrophys. J. **884**, 91 (2019).
[330] A. Albert *et al.* (ANTARES, IceCube, Pierre Auger and LIGO/Virgo Collaborations), Astrophys. J. Lett. **850**, L35 (2017).
[331] B. Peters, Il Nuovo Cimento **22**, 800 (1961).
[332] Z.-R. Wang, S.-Q. Xi, R.-Y. Liu, R. Xue, and X.-Y. Wang, Phys. Rev. D **101**, 083004 (2020).
[333] A. Aab *et al.* (Pierre Auger Collaboration), Phys. Rev. D **100**, 082003 (2019).
[334] H. Sagawa, PoS **ICRC2015**, 657 (2016).
[335] A. Aab *et al.* (Pierre Auger Collaboration), Front. Astron. Space Sci. **6**, 24 (2019).
[336] A. Aab *et al.* (Pierre Auger Collaboration), arXiv e-prints (2016), arXiv:1604.03637 [astro-ph.IM] .
[337] M. G. Aartsen *et al.*, arXiv e-prints (2019), arXiv:1911.02561 [astro-ph.HE] .
[338] S. Adrián-Martínez *et al.* (KM3NeT Collaboration), J. High Energy Phys. **2017**, 8 (2017).
[339] Q. Gou *et al.*, PoS ICRC, **ICRC2017**, 388 (2017).
[340] T. Hassan *et al.*, Astropart. Phys. **93**, 76 (2017).
[341] M. Actis *et al.* (CTA Consortium), Exper. Astron. **32**, 193 (2011).